Conditional Source-term Estimation for Diesel Combustion

Riyaz Ismail

Exeter College

University of Oxford

A thesis submitted for the degree of

Doctor of Philosophy

Hilary 2019

Acknowledgements

I would like to thank my supervisor, Dr Martin Davy for his support and guidance throughout this DPhil. I would also like to thank Professor Richard Stone for his support and the opportunity to be part of the Oxford Combustion & Engines Group. My sincerest thanks go to Dr Felix Leach for his help, support and willing collaborations on projects.

I would like to gratefully acknowledge Jaguar Land Rover for the financial support they provided. I would like to thank in particular, David Richardson, Sridhar Ayypureddi and others in the CFD team for their many helpful comments and discussions during this DPhil. I would also like to acknowledge the EPSRC and the Oxford Advanced Research Computing centre for the financial and computational support they provided during this DPhil. Additionally, I would like to express my thanks to Kelly Senecal, Suresh Nambully and the many others of the Convergent Science team for all their help and support during these past four years.

I would like to express my gratitude to Professor Kendal Bushe for his interest and many fruitful discussion on turbulent combustion modelling. His continual guidance and support were invaluable to the success of this project.

Many thanks go to my colleagues, Joseph Camm, Safwan Hanis and Louis Nicholson for their time, help and support during this DPhil.

I would especially like to express my sincerest thanks to XiaoHang Fang, Nick Papaioannou, Marc Perez Soriano, Blane Scott, Christina Palmou, Muyi Qiu, Paula Pedret and Mica. For without them, this DPhil would not be accomplished. I enjoyed the many shared discussions, coffees, hot-pots, brunches and everything in-between. You have all truly made my Oxford experience one of the most memorable away from home.

Most importantly, I would like to thank my parents, sisters, uncles and aunts who have supported and encouraged me throughout all my years of study.

Abstract

The compression ignition engine will continue to be a significant factor in the transportation sector due to its unmatched efficiency and robustness. As emissions legislation becomes more stringent, pressure on the automotive industry will continue to increase as both government and consumers demand cleaner technologies. The detailed understanding of in-cylinder physics is paramount to improving efficiency and reducing engine-out emissions. Consequently, numerical analysis is playing a much more pivotal role in the engine design phase with the requirement to predict complex combustion events and pollutant formation driving the need for ever better models. In this investigation, current numerical tools are used to elucidate the effects of spray targetting and piston bowl geometry on combustion evolution and pollutant formation. Closed cycle computational fluid dynamics simulations are performed on a sector mesh at various load points using the 3 Zones Extended Coherent Flame Model coupled with adaptive mesh refinement. The computational fluid dynamics model is validated experimentally at the baseline conditions at each test point after-which, parametric sweeps of bowl geometry, exhaust gas recirculation rate and nozzle tip protrusion are conducted. Results indicate that appropriately pairing fuel injection strategy and piston geometry is essential in reducing engine-out emissions.

In addition, a novel chemical source term closure based on Conditional Moment Closure (CMC) is developed to simulate diesel combustion. Conditional Source-term Estimation (CSE) uses the conditional averages in evaluating the mean chemical source term. However, unlike Conditional Moment Closure where transport equations are solved for the conditional averages. CSE approximates the conditional averages through inversion of an integral. Previous studies have shown CSE is capable of accurately simulating non-premixed flames of light hydrocarbon fuels. In this study, CSE is extended to simulate spray flame combustion by coupling the CSE combustion model with Flamelet Generated Manifolds chemistry reduction methodology. The CSE-FGM model is applied to the Engine Combustion Network n-Dodecane Spray.A – in a Large Eddy Simulation turbulence modelling framework. The model is successfully able to predict ignition delay and flame lift-off length with good agreement to experimental measurements. Additionally, the CSE-FGM model is validated further within a RANS framework to predict ignition delay and flame lift-off length over a wide range of ambient temperature and oxygen concentration conditions. The CSE-FGM model is successfully able to predict experimental trends and sensitivity with respect to ambient conditions.

Contents

List of Figures

Nomenclature

Abbreviations

AMR	Adaptive mesh refinment
ASI	After start of injection
CFD	Computational fluid dynamics
CFM	Coherent flame model
CMC	Conditional moment closure
CSE	Conditional source-term estimation
DNS	Direct numerical simulation
EBU	Eddy break-up model
ECFM-3Z	Extended coherent flame model - 3 zones
ECFM-CLEH	Extended coherent flame model - combustion limited by equlibirium enthalpy
ECN	Engine combustion network
EDC	Eddy dissipation concept
EGR	Exhaust gas recirculation
EVO	Exhaust valve opening
FEM	Finite element method
FGM	Flamelet generated manifold
FPI	Flame prolongation of ILDM
ICDF	Igniting counter-flow diffusion flame
ILDM	Intrinsic low dimensional manifold
IVC	Intake valve closing
KH-RT	Kelvin Helmholtz - Rayleigh Taylor
LES	Large eddy simulations
nIMEP	Net inidicated mean effective pressure
NSC	Nagle and Strickland-Constable
NTP	Nozzle tip protrusion
ODE	Ordinary differential equation
PDF	Probability Density Function

PEA	Partial equilibrium assumption
QSSA	Quasi steady state assumption
RANS	Reynolds averaged navier-stokes
RIF	Representative interactive flamelet
ROI	Rate of injection
SLFM	Steady laminar flamelet model
TCI	Turbulence-chemistry interaction
TGLDM	Trajectory generated low dimensional manifold
TKE	Turbulent kinetic energy
TKI	Tabulated kinetic ignition
TVSD	Truncated Singular Value Decomposition

Symbols

χ	Scalar dissipation rate
δ_{ij}	Kronecker operator
$\dot{\omega}_k$	Reaction rate of species k
ϵ	Dissipation rate of turbulent kinetic energy
κ	Wavenumber
$\mathcal{C}$	Progress variable
Pr	Prandtl number
Sc	Schmidt number
μ	Dynamic viscosity
μ_t	Turbulent viscosity
ν_{kr}, s	Stoichiometric coefficient
ϕ_{nozzle}	Nozzle diameter
ρ	Density
ρ_{amb}	Ambient density
Σ	Flame surface density
τ_{ij}	Viscous stress tensor
a	Strain rate
D	Diffusion coefficient
$E_{a,r}$	Activation energy
h_s	Sensible enthalpy
K	Stretch rate
k	Turbulent kinetic energy
M	Pope criterion
N	Scalar dissipation rate in the CMC equation
N_r	Number of reactions
N_s	Number of species
p	Static pressure

P_{amb}	Ambient pressure
P_{inj}	Injection pressure
q_i	Enthalpy diffusive flux
R_u	Universal gas constant
t	Time
T_{fu}	Fuel temperature
T_{ox}	Oxidiser temperature
u_i	Velocity in i-th direction where $i = 1, 2, 3$
$V_{k,i}$	i-th component of diffusion velocity of species k
W_k	Molar weight of species k
x_i	Cartesian coordinate space where $i = 1, 2, 3$
Y_k^{eq}	Equilibrium mass fraction of species k
Y_k	Mass fraction of species k
Z	Mixture fraction

Chapter 1

Introduction

1.1 Motivation

Combustion of gaseous and liquid fuels has been the primary energy source for transportation and industrial application with future trends indicating it will remain so [1]. This demand, driven mainly by economic recovery and emerging market growth will undoubtedly apply significant pressure on the environment, forcing governments to implement ever stricter emissions legislation in-order to minimise the impact. Globally, the transportation sector accounts for approximately 23% of total CO_2 emissions with road transport accounting for 20% [2]. Pollutants such as NO_x, soot and unburned hydrocarbons produced from incomplete/uncontrolled combustion pose serious health risks. As purchasing choices of consumers trend towards environmental friendliness, fuel efficiency and durability [3], automotive manufacturers are faced with the difficult task of simultaneously meeting both governmental and consumer requirements.

The spatial and temporal distribution of fuel within the cylinder directly influences ignition, combustion and pollutant formation. This has prompted numerous investigations into the detailed in-cylinder processes of diesel combustion. These range from fuel spray interaction/behaviour to chemical kinetics of the charge and other related physical phenomena. Diesel combustion is a complex process due to its inherent heterogeneity where, liquid fuel breakup, atomization, vaporization, fuel-air mixing, burned-unburned gas mixing and combustion occur simultaneously. Hence, there are a multitude of physical and chemical processes that contribute to the combustion phasing and pollutant formation. Optimisation methods for engine design and operation fall into two categories: the first, from which most of our current understanding of diesel combustion has originated, is experimental investigations with physical engines and the second, which has only recently become more pertinent, is multi-dimensional numerical analysis. Since neither can capture all relevant details, it is common to link the two methodologies with the numerical analysis allowing a deeper understanding of the physical processes occurring and the experimental observations allowing validation of the numerical models/analysis.

Numerical modelling has become increasingly popular in recent years as there have been dramatic increases in computational power that have enabled the use of advanced computational fluid dynamics models to describe many of the complex phenomenon occurring during diesel combustion. As such, there has been a significant reduction in the requirements for experimental testing as conceptual engines and advanced combustion modes can be explored long before prototypes are made. However, present understanding of the combustion process and associated pollutant formation mechanisms are limited and further investigation is needed in-order to better represent these processes numerically.

1.2 Objectives

The proposed research will follow two paths:

1. The first part of the project will focus on using current numerical tools to elucidate key operating parameters that govern performance and emissions formation of a combustion system for which experimental data will be available. This phase of study will also highlight shortcomings of current models.

2. Within the myriad of physical processes taking place in diesel combustion, of particular interest to this study are those of the turbulence interactions with chemistry (TCI). Current combustion models have a number of shortcomings such as simplified chemical kinetics, rudimentary TCI descriptions and high computational expense. Therefore, the objective of this part of the project will be to extend a novel chemical source term closure in a commercial Computational Fluid Dynamics (CFD) code. This will facilitate the use of detailed chemistry through tabulation, in-order to better represent the multi-scale, multi-physics problem of diesel combustion.

1.3 Thesis outline

Beginning with this introductory chapter, an overview of turbulent combustion will be presented in Chapter 2 where the governing equations and models for turbulence and chemical source term closure will be discussed. Finally, a brief description of spray modelling will be highlighted.

Chapter 3 will focus on computational modelling of a single cylinder research engine using currently available numerical tools. The effects of piston bowl geometry and spray targetting on combustion evolution and emissions formation over a wide range of operating points will be investigated.

Chapter 4 introduces the novel turbulent combustion model (Conditional Source-term Estimation) and its extension to spray combustion. Additionally, the chemistry tabulation methodology of Flamelet Generated Manifolds will be presented.

Chapter 5 describes application of the newly implemented combustion model to the Engine Combustion Network Sandia Spray A. Numerical simulations over a wide range of operating points will be used to validate the combustion model under a Large Eddy Simulation framework. Comparisons of experimental and numerical results will be presented for key combustion characteristics of ignition delay and flame lift-off length.

Finally, a summary of the main findings and recommendations for future work will be presented in Chapter 6.

1.4 Publications

It is acknowledged that the contents of Chapters 3-4 have been published in the following:

- Felix Leach, Riyaz Ismail, Martin Davy, Adam Weall, and Brian Cooper. "Comparing the Effect of Fuel/Air Interactions in a Modern High-Speed Light-Duty Diesel Engine". In: *SAE Technical Paper 2017-24-0075*. SAE International, Sept. 2017

- Riyaz Ismail, Felix Leach, Martin H Davy, David Richardson, and Brian Cooper. "Computational investigation of the effects of piston geometry on the combustion evolution in a light duty HSDI engine". In: *ASME 2017 Internal Combustion Engine Division Fall Technical Conference ICEF2017-3588*. American Society of Mechanical Engineers. 2017

- Felix Leach, Riyaz Ismail, and Martin Davy. "Engine-out emissions from a modern high speed diesel engine – The importance of Nozzle Tip Protrusion". In: *Applied Energy* 226 (2018), pp. 340–352

- Felix Leach, Riyaz Ismail, Martin Davy, Adam Weall, and Brian Cooper. "The effect of a stepped lip piston design on performance and emissions from a high-speed diesel engine". In: *Applied Energy* 215 (2018), pp. 679–689

- XiaoHang Fang, Riyaz Ismail, and Martin H Davy. "Numerical Investigation of Combustion Recession on ECN Diesel Spray A". in: *ASME 2017 Internal Combustion Engine Division Fall Technical Conference ICEF2018-9597*. American Society of Mechanical Engineers. 2018

- XiaoHang Fang, Riyaz Ismail, and Martin H Davy. "A Study on Kinetic Mechanisms of Diesel Fuel Surrogate n-Dodecane for the Simulation of Combustion Recession". In: *SAE Technical Paper 2019-01-0202*. SAE International, Jan. 2019

In addition, the following journal paper is in preparation and is aimed to be submitted to Combustion Theory and Modelling:

- XiaoHang Fang, Riyaz Ismail, Kendal Bushe, Martin Davy. "Simulation of ECN Diesel Spray A using Conditional Source-term Estimation"

CHAPTER 2

Background

2.1 Introduction

Modelling of turbulent reactive flows presents a number of challenges especially in the context of internal combustion engines, where flow is compressible, multi-phase, multi-scale, unsteady and three dimensional. Due to strong coupling between the fluid dynamics and chemistry within the domain of interest, any modelling assumption made in order to close one set of equations will have an effect on others which could result in a misrepresentation of physical reality. Even though this strong coupling exists, the historical process is that each aspect of turbulent combustion is investigated and modelled in isolation, so as to limit complexity - with the evaluation of the model and its interactions with and effects on the rest of the system occurring at a later point in time. A formal definition of this process as expressed by Veynante and Vervisch [10] is shown in Figure 2.1.

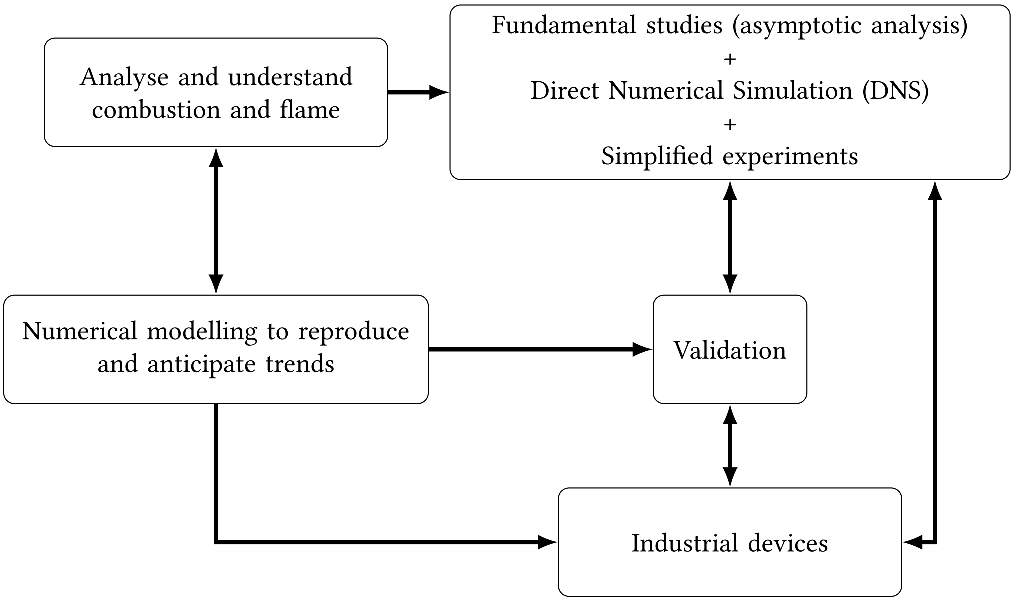

Figure 2.1: Combustion modelling steps. Adapted from [10]

2.2 Instantaneous conservation equations

Derived from fundamental principles of balancing a variable over an infinitesimally small volume. The instantaneous form of partial differential equations for a single phase Newtonian fluid with non-constant density in Cartesian notation are given as follows [11].

Mass: also known as the continuity equation, total mass balance in a system is given as:

$$\frac{\partial \rho}{\partial t} + \frac{\partial \rho u_i}{\partial x_i} = 0 \tag{2.1}$$

Momentum: conservation of linear momentum is given as:

$$\frac{\partial \rho u_j}{\partial t} + \frac{\partial \rho u_i u_j}{\partial x_i} = -\frac{\partial p}{\partial x_j} + \frac{\partial \tau_{ij}}{\partial x_i} + \mathcal{F}_i \tag{2.2}$$

where p is static pressure, τ_{ij} is the viscous stress tensor and $\mathcal{F}_i$ is a body force.

Enthalpy: energy balance can be written in the form of enthalpy, here sensible enthalpy, h_s is used:

$$\frac{\partial \rho h_s}{\partial t} + \frac{\partial \rho u_i h_s}{\partial x_i} = \frac{\partial p}{\partial t} + \frac{\partial u_i p}{\partial x_i} - \frac{\partial q_i}{\partial x_i} + \frac{\partial u_i \tau_{ij}}{\partial x_j} + \dot{\omega}_T \tag{2.3}$$

where q_i is the enthalpy diffusive flux and $\dot{\omega}_T$ is the heat release due to combustion.

Species: for flows with multiple species, additional balance equations must be solved for each species.

$$\frac{\partial \rho Y_k}{\partial t} + \frac{\partial \rho u_i Y_k}{\partial x_i} = -\frac{\partial \rho V_{k,i} Y_k}{\partial x_i} + \dot{\omega}_k \tag{2.4}$$

where Y_k is the mass fraction of species k, $V_{k,i}$ is the i-th component of the diffusion velocity of species k and $\dot{\omega}$ is the reaction rate of species k.

Closure of these equations are done by providing expressions for the viscous stress tensor, diffusive fluxes and reaction rate terms. The viscous stress tensor is given by:

$$\tau_{ij} = \mu \frac{2}{3} \frac{\partial u_k}{\partial x_k} \delta_{ij} + \mu \left(\frac{\partial u_i}{\partial x_j} + \frac{\partial u_j}{\partial x_i} \right) \tag{2.5}$$

where μ is the dynamic viscosity and δ_{ij} is the Kronecker operator.

Fick's law is employed to close the species diffusive flux and Fourier's law is used to provide and expression for the enthalpy diffusive flux. More complex expressions for the diffusion fluxes which include species diffusion due to temperature gradients (Soret effect) and molecular transport due to pressure gradients are commonly neglected. Additionally, body forces and energy transfer due to concentration gradients (Dufour effect) are also ignored in these expressions.

Thermochemical evolution in reacting flows is determined by chemical kinetics of the system which consists of N_s species with N_r reactions. The reaction rate of a reaction r, is given as:

$$\dot{\omega}_r = k_{fr} \prod_{k=1}^{N} \left(\frac{\rho Y_k}{W_k} \right)^{\nu'_{kr}} - k_{br} \prod_{k=1}^{N} \left(\frac{\rho Y_k}{W_k} \right)^{\nu''_{kr}} \tag{2.6}$$

where W_k is the molar weight of species k and ν'_{kr} and ν''_{kr} denote the forward and reverse stoichiometric coefficients for species k in reaction r. The forward k_{fr} and reverse k_{br}

rate coefficients are computed by the Arrhenius expression:

$$k_r = A_r T^{\beta_r} \exp\left(\frac{E_{a,r}}{R_u T}\right) \tag{2.7}$$

where A_r and β_r are the pre-exponential rate constants, $E_{a,r}$ is the activation energy and R_u is the universal gas constant. The reaction rate of species k can then be computed through summation over all elementary reactions as:

$$\dot{\omega}_k = W_k \sum_{r=1}^{N_r} \dot{\omega}_r \left(\nu''_{kr} - \nu'_{kr}\right) \tag{2.8}$$

2.3 Reynolds and Favre decomposition

A full numerical solution of the instantaneous form of the conservation equations is limited to very simple problems where the range of scales both in time and space are small. For engineering flows with complex geometry and a large range of length and time scales, it is not possible to obtain a full numerical solution due to the impractical computational requirements. Accordingly, the instantaneous set of equations are typically decomposed into a form where only the mean flow field is considered. The fluctuations and turbulent structures are then integrated into mean quantities, thus eliminating their explicit description in the conservation equations. Following this approach, each quantity, ϕ is split into a mean, $\overline{\phi}$ and fluctuating part, ϕ':

$$\phi = \overline{\phi} + \phi' \tag{2.9}$$

$$\overline{\phi'} = 0 \tag{2.10}$$

Applying Equation 2.9 to the conservation equations results in the Reynolds Averaged Navier Stokes equations (RANS) which represent conservation of the mean quantity $\overline{\phi}$. However, this procedure is only suitable for incompressible flows as with variable density flows, Reynolds decomposition will introduce a velocity-density correlation, $\overline{\rho' u'_i}$ whose closure adds another level of complexity. To avoid this problem, a density weighted averaging procedure is implemented such that:

$$\phi = \tilde{\phi} + \phi'' \tag{2.11}$$

$$\tilde{\phi} = \frac{\overline{\rho\phi}}{\overline{\rho}} \tag{2.12}$$

$$\widetilde{\phi''} = \frac{\overline{\rho(\phi - \tilde{\phi})}}{\overline{\rho}} = 0 \tag{2.13}$$

Applying this decomposition to the instantaneous conservation equations results in the following set of Favre averaged equations:

Mass:

$$\frac{\partial \overline{\rho}}{\partial t} + \frac{\partial \overline{\rho}\tilde{u}_i}{\partial x_i} = 0 \tag{2.14}$$

Momentum:

$$\frac{\partial \overline{\rho}\tilde{u}_i}{\partial t} + \frac{\partial \overline{\rho}\tilde{u}_i\tilde{u}_j}{\partial x_i} = -\frac{\partial \overline{p}}{\partial x_j} + \frac{\partial}{\partial x_i}\left(\overline{\tau}_{ij} - \overline{\rho}\widetilde{u_i''u_j''}\right) + \overline{F}_i \tag{2.15}$$

Enthalpy:

$$\frac{\partial \overline{\rho}\tilde{h}_s}{\partial t} + \frac{\partial \overline{\rho}\tilde{u}_i\tilde{h}_s}{\partial x_i} = \frac{\partial \overline{p}}{\partial t} + \frac{\partial \tilde{u}_i\overline{p}}{\partial x_i} - \frac{\partial}{\partial x_i}\left(\overline{q}_i + \overline{\rho}\widetilde{u_i''h_s''}\right) + \overline{\frac{\partial u_i\tau_{ij}}{\partial x_j}} + \overline{\dot{\omega}}_T \tag{2.16}$$

Species:

$$\frac{\partial \overline{\rho}\widetilde{Y}_k}{\partial t} + \frac{\partial \overline{\rho}\tilde{u}_i\widetilde{Y}_k}{\partial x_i} = -\frac{\partial}{\partial x_i}\left(\overline{V_{k,i}Y_k} + \overline{\rho}\widetilde{u_i''Y_k''}\right) + \overline{\dot{\omega}}_k \tag{2.17}$$

As a result of the averaging procedure, a number of additional terms have been introduced into the conservation equations. This is what is termed as the closure problem of moment methods. And unless expressions for the additional terms are presented, some of which are described below, there are more unknowns than equations:

- Reynolds stresses, $\widetilde{u_i''u_j''}$: a turbulence model provides an approximation for this term. An overview of the main models will be presented in Section 2.4.
- Laminar diffusive fluxes in the enthalpy $\overline{q}_i$ and species $\overline{V_{k,i}Y_k}$ equations are

generally neglected if the Reynolds number is high. However, if retained, they are modelled in terms of average quantities as:

$$\overline{q}_i = -\frac{\mu}{\mathrm{Pr}}\frac{\partial \tilde{h}}{\partial x_i} \tag{2.18}$$

$$\overline{V_{k,i}Y_k} = -\overline{\rho}\overline{D}_k\frac{\partial \widetilde{Y}_k}{\partial x_i} \tag{2.19}$$

where Pr is the Prandtl number and $\overline{D}_k$ is a mean species molecular diffusion coefficient.

- Velocity-scalar co-variances in the enthalpy $\widetilde{u_i''h_s''}$ and species equations $\widetilde{u_i''Y_k''}$, to which an approximation is made via the gradient diffusion hypothesis as:

$$\overline{\rho}\widetilde{u_i''h_s''} = -\frac{\mu_t}{\mathrm{Pr}_t}\frac{\partial \tilde{h}_s}{\partial x_i} \tag{2.20}$$

$$\overline{\rho}\widetilde{u_i''Y_k''} = -\frac{\mu_t}{\mathrm{Sc}_{kt}}\frac{\partial \widetilde{Y}_k}{\partial x_i} \tag{2.21}$$

  where μ_t is the turbulent viscosity which is derived from the turbulence model, Sc_{kt} is the turbulent Schmidt number for species k and Pr_t is the turbulent Prandtl number.

- Closure of the mean reaction rate $\overline{\dot{\omega}}$, in the species equation is the main objective of turbulent combustion modelling. An overview of the main modelling approaches will be described in Section 2.5.

2.4 Turbulence modelling

Though turbulence has no formal definition, it exhibits a number of characteristic features allowing us a satisfactory understanding of its nature. Turbulent flow is always disorganised, chaotic, three-dimensional, unsteady and rotational with a wide range of length and time scales. Although turbulent flow appears to be random, it is deterministic as the flow is still governed by the Navier-Stokes equations - which themselves are deterministic. A common way of representing this order is through the turbulent energy spectrum, Figure 2.2, which expresses the energy content, E, as a function of the wavenumber, κ, for the different scales present within the flow [12].

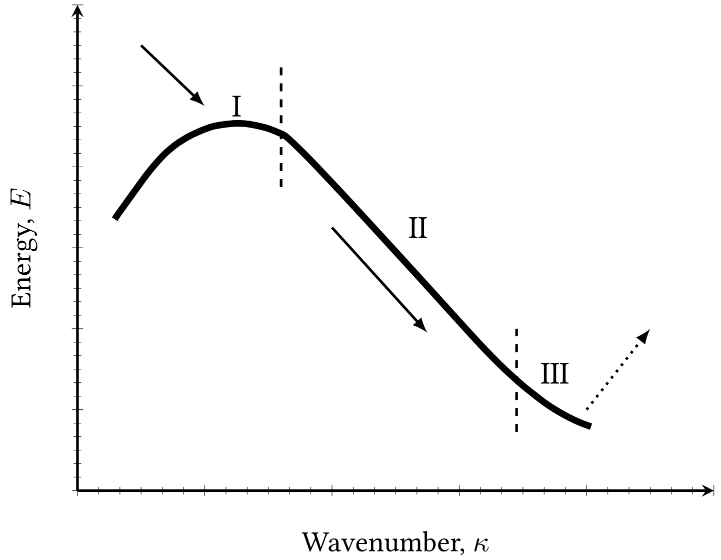

Figure 2.2: Turbulent kinetic energy spectrum. Adapted from [12]

- I: This range contains the integral (dominant) length scale eddies that interact with the mean flow extracting energy from it.
- II: The inertial sub-range facilitates the cascade process as it transports energy from the large eddies to the smaller eddies in the dissipation range. The eddies in this region are independent of both I and III and the flow of energy through this range is expressed by Kolmogorov's $^{-5}/_{3}$ law:

$$E(\kappa) = Constant \cdot \epsilon^{\frac{2}{3}} \cdot \kappa^{-\frac{5}{3}} \tag{2.22}$$

- III: Viscous sub-range. Eddies here are small and isotropic with the scales defined by the Kolmogorov scales, it is here where dissipation occurs.

A Direct Numerical Simulation (DNS) solution of the instantaneous balance equations (Equation 2.1-2.4) will resolve the entire spectrum. However, as mentioned previously, this is not possible for any real flow, hence, the choice of turbulence model will directly influence which scales will be resolved and which will be modelled. In RANS approximations, the entire energy spectrum is modelled. The various closure methodologies in RANS can be broken down into models that adopt the Boussinesq assumption and those that do not. Boussinesq proposed that the Reynolds stresses are a function of the mean velocity gradients and a turbulent viscosity μ_t:

$$\overline{\rho}\widetilde{u_i''u_j''} = -\mu_t \left(\frac{\partial \tilde{u}_i}{\partial x_j} + \frac{\partial \tilde{u}_j}{\partial x_i} - \frac{2}{3}\delta_{ij}\frac{\partial \tilde{u}_k}{\partial x_k} \right) + \frac{2}{3}\overline{\rho}k \tag{2.23}$$

where $k = \frac{1}{2}\sum_{k=1}^{3} \widetilde{u_k''u_k''}$. Adopting this assumption then leaves only one unknown term, the turbulent viscosity. Knowing that $\mu_t = \overline{\rho}\nu_t$ and ν_t having dimensions of $\mathrm{m^2s^{-1}}$ (identical to ν), it is apparent that $\nu_t \propto velocity \cdot length$. Therefore, any quantity that can describe the velocity or length scale adequately can be used to compute μ_t. Some of the more commonly modelling approaches are described below.

Algebraic models

These are the simplest models as they either assume a constant value of μ_t throughout the domain, or use an algebraic relation to compute μ_t.

One-equation models

In one-equation models, the velocity scale is determined by solving a transport equation for the turbulent kinetic energy. The length scale is then obtained from an algebraic relation after-which the turbulent viscosity can be calculated.

Two-equation models

These are the most widely used models as they offer a good balance between accuracy and performance. The most used two-equation models for combustion simulations are the $k - \epsilon$ [13] and RNG $k - \epsilon$ [14] models where a transport equation is solved for both the turbulent kinetic energy, k and its dissipation, ϵ. The modelled k and ϵ equations read:

$$\frac{\partial \bar{\rho}\tilde{k}}{\partial t} + \frac{\partial \bar{\rho}\tilde{u}_i\tilde{k}}{\partial x_i} = \frac{\partial}{\partial x_i}\left(\left(\mu + \frac{\mu_t}{\sigma_k}\right)\frac{\partial \tilde{k}}{\partial x_i}\right) - \bar{\rho}\widetilde{u_i''u_j''}\frac{\partial \tilde{u}_i}{\partial x_j} - \bar{\rho}\tilde{\epsilon} \tag{2.24}$$

$$\frac{\partial \bar{\rho}\tilde{\epsilon}}{\partial t} + \frac{\partial \bar{\rho}\tilde{u}_i\tilde{\epsilon}}{\partial x_i} = \frac{\partial}{\partial x_i}\left(\left(\mu + \frac{\mu_t}{\sigma_\epsilon}\right)\frac{\partial \tilde{\epsilon}}{\partial x_i}\right) - C_{\epsilon 1}\frac{\tilde{\epsilon}}{\tilde{k}}\bar{\rho}\widetilde{u_i''u_j''}\frac{\partial \tilde{u}_i}{\partial x_j} - C_{\epsilon 2}\bar{\rho}\frac{\tilde{\epsilon}^2}{\tilde{k}} \tag{2.25}$$

where σ_k, σ_ϵ , C_{ϵ_1} and C_{ϵ_2} are model constants. The turbulent viscosity is then computed as:

$$\mu_t = \bar{\rho}C_\mu\frac{\tilde{k}^2}{\tilde{\epsilon}} \tag{2.26}$$

where C_μ is a model constant.

The RNG $k - \epsilon$ model first proposed by Yakhot *et al.* [15] re-normalised the Navier-Stokes equation to account for the smaller scales of motion. With the standard $k - \epsilon$ model, the turbulent viscosity is computed from a single length scale and hence turbulent diffusion only originates from that one scale. This is contrary to reality where all scales of motion will contribute to diffusion. The RNG $k - \epsilon$ model in compressible form as derived by Han *et al.*[14] modifies the dissipation equation to account for smaller scales through the addition of an additional term, R_{rng}, that represents the effect of the mean flow distortion on the dissipation rate:

$$\frac{\partial \bar{\rho}\tilde{\epsilon}}{\partial t} + \frac{\partial \bar{\rho}\tilde{u}_i\tilde{\epsilon}}{\partial x_i} = \frac{\partial}{\partial x_i}\left(\left(\mu + \frac{\mu_t}{\sigma_\epsilon}\right)\frac{\partial \tilde{\epsilon}}{\partial x_i}\right) - C_{\epsilon 1}\frac{\tilde{\epsilon}}{\tilde{k}}\bar{\rho}\widetilde{u_i''u_j''}\frac{\partial \tilde{u}_i}{\partial x_j} - C_{\epsilon 2}\bar{\rho}\frac{\tilde{\epsilon}^2}{\tilde{k}} - C_{\epsilon 3}\bar{\rho}\tilde{\epsilon}\frac{\partial \tilde{u}_i}{\partial x_j} - R_{rng} \tag{2.27}$$

where $C_{\epsilon 3}$ is a constant and R_{rng} is computed from:

$$R_{rng} = \frac{C_\mu\tilde{\eta}^3\left(1 - \frac{\tilde{\eta}}{\eta^0}\right)}{1 + \beta\tilde{\eta}^3}\frac{\bar{\rho}\tilde{\epsilon}}{\tilde{k}} \tag{2.28}$$

where η^0 is a constant, $\tilde{\eta} = S\frac{\tilde{k}}{\tilde{\epsilon}}$ and $S = \left(2\left(\frac{1}{2}\left(\frac{\partial \tilde{u}_i}{\partial x_j} + \frac{\partial \tilde{u}_j}{\partial x_i}\right)\right)^2\right)^{1/2}$.

Reynolds Stress Models

These models avoid using the Boussinesq assumption by solving additional transport equations for each component of the Reynolds stress tensor and one more quantity to determine a length scale for the turbulence. The modelled equation for the Reynolds Stress tensor reads [16]:

$$\frac{\partial \overline{\rho} \widetilde{u_i'' u_j''}}{\partial t} + \frac{\partial}{\partial x_k} \left(\overline{\rho} \tilde{u}_k \widetilde{u_i'' u_j''} \right) + \frac{\partial}{\partial x_k} T_{kij} = P_{ij} + R_{ij} - \epsilon_{ij} \tag{2.29}$$

where T_{kij} is the Reynolds-stress flux, R_{ij} is the pressure strain and ϵ_{ij} is the dissipation which all need to be closed.

Filtering and Large Eddy Simulation (LES)

LES allows explicit computation of the larger flow scales whilst modelling smaller ones. The main idea behind this is that most of the computational expense of Direct Numerical Simulations is due to resolution of the smaller scales. If this burden is removed, a more correct solution (when compared to unsteady RANS) can potentially be achieved at a reasonable computational expense. For reactive flows, especially with respect to non-premixed combustion, most of the turbulence-chemistry-flame interactions occur at the smaller scales which are still modelled in LES. Whilst this does not seem attractive, LES provides a number of benefits over using the standard RANS techniques [10, 12]:

- Most large scale flow structures are geometry dependent whereas small scale flow structures generally exhibit uniform properties and as most turbulence models make an isotropic assumption of the smaller scales, using LES will give a better solution even at the sub-grid level.
- Turbulent mixing governs flame propagation in reactive flows, the fuel-oxidiser interactions are resolved in both space and time in LES, allowing clear identification of combustion zones with turbulence/flame properties explicitly computed.
- Unsteady RANS provides an ensemble averaged solution, hence cycle-to-cycle variability aspect is averaged out. With LES, individual realisations are possible

and this allows a much greater insight into the dynamics of combustion which are well known to vary from cycle-to-cycle.

In LES, all quantities are filtered in order to decompose them into resolved and residual components. Filters can be defined in either spectral space, where the resolved components are limited by a cut-off frequency, or in physical space, where the filter width dictates the limits of resolution. The filtering operation can be defined as:

$$\overline{\Phi}_i(x,t)s = \int \Phi_i(x',t)G(x-x')dx' \tag{2.30}$$

where $\overline{\Phi}_i$ is the filtered quantity in the ith direction and $G(x)$ is the filter function. Common filters include [10, 12]:

- Cut-off filter in spectral space, κ, is the spatial wavenumber and the filter suppresses all quantities less than the cut-off wavenumber, κ_c.

$$\overline{G}(\kappa) = \begin{cases} 1 & if\, \kappa \leq \kappa_c \\ 0 & otherwise \end{cases} \tag{2.31}$$

- Box filter in physical space where (x_1, x_2, x_3) are the spatial coordinates of x and the filtering operation corresponds to averaging the quantity Φ over a box of size Δ.

$$\overline{G}(x) = G(x_1, x_2, x_3) = \begin{cases} \frac{1}{\Delta^3} & if\ |x_i| \leq \frac{\Delta}{2} \\ 0 & otherwise \end{cases} \tag{2.32}$$

- Gaussian filter in physical space

$$\overline{G}(x) = G(x_1, x_2, x_3) = \left(\frac{6}{\pi\Delta^2}\right)^{1/2} exp\left(-\frac{6x_i^2}{\Delta^2}\right) \tag{2.33}$$

In finite volume methods, box filtering is almost always used with implicit filtering employed. Explicit methods in Equation 2.30 are often avoided due to difficulty in implementing an explicit filter on a non-isotropic grid [17]. Implicit filtering equates to the numerical scheme and grid size acting as the filter width i.e. the control volume being the same as the filter volume:

$$\Delta \equiv (\Delta x_1 \Delta x_2 \Delta x_3)^{1/3} \tag{2.34}$$

where Δx_i is the grid spacing in the ith direction.

Similarly to RANS, the instantaneous conservation equations are Favre filtered (as opposed to Reynolds averaged) to derive conservation equations for Favre filtered quantities.

$$\Phi = \widetilde{\Phi} + \Phi'' \tag{2.35}$$

$$\widetilde{\Phi} = \frac{\overline{\rho\Phi}}{\overline{\rho}} \tag{2.36}$$

$$\widetilde{\phi''} \neq 0 \tag{2.37}$$

Mass:

$$\frac{\partial \overline{\rho}}{\partial t} + \frac{\partial \overline{\rho}\tilde{u}_i}{\partial x_i} = 0 \tag{2.38}$$

Momentum:

$$\frac{\partial \overline{\rho}\tilde{u}_i}{\partial t} + \frac{\partial \overline{\rho}\tilde{u}_i\tilde{u}_j}{\partial x_i} = -\frac{\partial \overline{p}}{\partial x_j} + \frac{\partial}{\partial x_i}\left(\overline{\tau}_{ij} - \overline{\rho}\left(\widetilde{u_i''u_j''} - \tilde{u}_i\tilde{u}_j\right)\right) + \overline{F}_i \tag{2.39}$$

Enthalpy:

$$\frac{\partial \overline{\rho}\tilde{h}_s}{\partial t} + \frac{\partial \overline{\rho}\tilde{u}_i\tilde{h}_s}{\partial x_i} = \frac{\partial \overline{p}}{\partial t} + \frac{\partial \tilde{u}_i\overline{p}}{\partial x_i} - \frac{\partial}{\partial x_i}\left(\overline{q}_i + \overline{\rho}\left(\widetilde{u_i''h_s''} - \tilde{u}_i\tilde{h}_s\right)\right) + \overline{\frac{\partial u_i\tau_{ij}}{\partial x_j}} + \overline{\dot{\omega}}_T \tag{2.40}$$

Species

$$\frac{\partial \overline{\rho}\widetilde{Y}_k}{\partial t} + \frac{\partial \overline{\rho}\tilde{u}_i\widetilde{Y}_k}{\partial x_i} = -\frac{\partial}{\partial x_i}\left(\overline{V_{k,i}Y_k} + \overline{\rho}\left(\widetilde{u_i''Y_k''} - \tilde{u}_i\widetilde{Y}_k\right)\right) + \overline{\dot{\omega}}_k \tag{2.41}$$

The unclosed quantities in these equations are as follows:

- Unresolved Reynolds stresses, $\tau_{ij} = (\widetilde{u_iu_j} - \tilde{u}_i\tilde{u}_j)$, for which a sub-grid turbulence model is required.

- As with RANS, the laminar diffusive fluxes in the enthalpy ($\overline{q}_i$) and species ($\overline{V_{k,i}Y_k}$) equations are generally neglected if the Reynolds number is high. However, if retained, they are also modelled using the gradient assumption:

$$\overline{q}_i = -\frac{\mu}{\mathrm{Pr}}\frac{\partial \tilde{h}}{\partial x_i} \tag{2.42}$$

$$\overline{V_{k,i}Y_k} = -\overline{\rho}\overline{D}_k\frac{\partial \widetilde{Y}_k}{\partial x_i} \tag{2.43}$$

- Similarly, the unresolved turbulent fluxes in the enthalpy $\left(\widetilde{u_i h_s} - \tilde{u}_i\tilde{h}_s\right)$ and species equations $\left(\widetilde{u_i Y_k} - \tilde{u}_i\tilde{Y}_k\right)$ are also approximated via the gradient diffusion hypothesis as:

$$\left(\widetilde{u_i h_s} - \tilde{u}_i\tilde{h}_s\right) = -\frac{\mu_{sgs}}{\mathrm{Pr}_{sgs}}\frac{\partial \tilde{h}_s}{\partial x_i} \tag{2.44}$$

$$\left(\widetilde{u_i Y_k} - \tilde{u}_i\tilde{Y}_k\right) = -\frac{\mu_{sgs}}{\mathrm{Sc}_{k,sgs}}\frac{\partial \widetilde{Y}_k}{\partial x_i} \tag{2.45}$$

  where μ_{sgs} is the sub-grid scale viscosity, Pr_{sgs} is the sub-grid scale Prandtl number and $\mathrm{Sc}_{k,sgs}$ is the sub-grid scale Schmidt number.

- Closure of the filtered reaction rate, $\overline{\dot{\omega}}$, is done through a combustion model.

2.5 Combustion modelling

2.5.1 Chemical source term-explicit expansion

The chemical source term closure presents one of the greatest challenges in turbulent combustion modelling due to its highly non-linear behaviour, and its sensitivity to truncation. This is clearly demonstrated through derivation of the Taylor expansion of the chemical source term as per Veynante and Vervisch [10]. Taking a single-step irreversible reaction between fuel, F and oxidiser, O:

$$\mathrm{F} + s\mathrm{O} \Longrightarrow (1+s)\mathrm{P} \tag{2.46}$$

As before, an Arrhenius expression is used to determine the reaction rate of the fuel:

$$\dot{\omega}_F = -A\rho^2 T^b Y_F Y_O \exp\left(-\frac{T_\mathrm{A}}{T}\right) \tag{2.47}$$

where, A is a constant and T_A, is the activation temperature. Due to the non-linearity of the reaction rate, the most convenient way of determining the mean reaction rate as a function of the mean mass fractions, density and temperature is through a Taylor expansion of the temperature fluctuations using [10]:

$$\exp\left(-\frac{T_\mathrm{A}}{\widetilde{T}}\right) = \exp\left(-\frac{T_\mathrm{A}}{\widetilde{T}}\right)\left(1 + \sum_{n=1}^{+\infty} P_n \frac{T''^n}{\widetilde{T}^n}\right) \tag{2.48}$$

$$T^b = \widetilde{T}^b \left(1 + \sum_{n=1}^{+\infty} Q_n \frac{T''^n}{\widetilde{T}_n}\right) \tag{2.49}$$

where P_n and Q_n are given as:

$$P_n = \sum_{k=1}^{n} (-1)^{n-k} \frac{(n-1)!}{(n-1)!\left\{(k-1)!\right\}^2 k} \left(\frac{T_\mathrm{A}}{\widetilde{T}}\right)^k \tag{2.50}$$

$$Q_n = \frac{b\,(b+1)\,...\,(b+n-1)}{n!} \tag{2.51}$$

The mean reaction rate is then:

$$
\begin{aligned}
\bar{\dot{\omega}}_F &= -A\bar{\rho}^2\widetilde{T}^b\widetilde{Y}_F\widetilde{Y}_O \exp\left(-\frac{T_{\mathrm{A}}}{\widetilde{T}}\right) \\
&\times \left[1 + \frac{\widetilde{Y_F''Y_O''}}{\widetilde{Y}_F\widetilde{Y}_O} + (P_1+Q_1)\left(\frac{\widetilde{Y_F''T''}}{\widetilde{Y}_F\widetilde{T}} + \frac{\widetilde{Y_O''T''}}{\widetilde{Y}_O\widetilde{T}}\right)\right. \\
&+ \left.(P_2+Q_2+P_1Q_1)\left(\frac{\widetilde{Y_F''T''^2}}{\widetilde{Y}_F\widetilde{T}^2} + \frac{\widetilde{Y_O''T''^2}}{\widetilde{Y}_O\widetilde{T}^2}\right) + \ldots\right]
\end{aligned}
\tag{2.52}
$$

A number of difficulties result from this equation, new covariance terms appear which need to be closed - either through algebraic relations or additional transport equations. Truncation of this series would eliminate these terms altogether. However, due to the non-linearity in Equation 2.52 and the temperature fluctuations potentially being very high, the result would be a very poor approximation. A further difficulty arises from the fact that this expression is valid only for a single step irreversible reaction, hence, extending this type of closure to multi-step chemical schemes would in itself be a major challenge. As such, this type of closure is avoided in turbulent combustion modelling and most methods are derived from a physical analysis, where length, velocity and time scales are considered. Methodologies for turbulent non-premixed combustion modelling are generally grouped into two main categories: infinitely fast chemistry and finite rate chemistry, which correspond to the chemical/turbulent time scales for which they are applicable [10, 11, 16]. An overview of the commonly used models in each category is presented below.

2.5.2 Infinitely fast chemistry methods

Eddy Break Up (EBU) Model

The EBU model was proposed by Spalding [18] as a first attempt at closing the chemical source term. As mentioned before, turbulent mixing can be seen as an energy cascade process from the integral length scale down to the molecular scales. The basic premise behind the EBU model and its derivative, the Eddy Dissipation Concept

(EDC) - which applies to non-premixed combustion [19], is that turbulent mixing is rate determining in combustion because of infinitely fast chemistry. The characteristic turbulent mixing time can be calculated from the turbulent quantities as:

$$\tau_t = \frac{\tilde{k}}{\tilde{\epsilon}} \tag{2.53}$$

The mean reaction rate for products with the EBU model is then given by:

$$\overline{\dot{\omega}}_P = \overline{\rho} C_{EBU} \frac{1}{\tau_t} \sqrt{\widetilde{Y_P''^2}} \tag{2.54}$$

where C_{EBU} is a model constant, and Y_P'', is variance of the product mass fraction. The EDC model extends the definition in Equation 2.54 by taking the minimum of three reaction rates:

$$\overline{\rho\dot{\omega}_F} = \alpha\overline{\rho}\frac{1}{\tau_t} min\left(\tilde{Y_F}, \frac{\tilde{Y_O}}{s}, \beta\frac{\tilde{Y_P}}{(1+s)}\right) \tag{2.55}$$

where α and β are tunable model constants and $\tilde{Y_O}$, $\tilde{Y_P}$ represents the reactant and product mass fractions. This methodology appears quite attractive as the mean reaction rate is a function of known quantities. However, as the chemical time scales are omitted and turbulence is assumed to behave isotropically, the EDC model overestimates the mean reaction rate in highly strained flow regions [10]. Additionally, ignition or stabilisation characteristics cannot be predicted due to the fact that fuel and oxidiser burn on contact. Furthermore, the model constants need to be tuned for each case to get any meaningful results [11].

2.5.3 Finite rate chemistry methods

Well-Mixed Model

The Well-Mixed combustion model treats each computational cell as a homogeneous reactor by assuming turbulent mixing is infinitely fast. As such, turbulence-chemistry interactions are not explicitly accounted for with this model and the reaction rate is calculated directly by solving Equation 2.8 using the mean value of species and temperature. Provided an accurate reaction mechanism is used, Well-Mixed models can give acceptable results where fluctuations in temperature and species are small, or where chemical time scales are greater than turbulent time scales [10]. However, in most applications this methodology leads to large errors in the mean reaction rate [20].

Flamelet

The description of turbulent diffusion flames as an ensemble of laminar flamelet's was first pioneered by Williams [21]. Flamelet equations were then derived based on the idea that local balance between diffusion and reaction are similar to those found in prototype laminar flames [22, 23]. If chemical time-scales are much shorter than characteristic turbulence scales and the flame is thin, a flamelet can be viewed as a thin reactive-diffusive one-dimensional laminar flame sheet embedded in a non-reactive turbulent flow field. Flamelet models are constructed from an asymptotic view of diffusive-reactions with the controlling parameters being mixture fraction, Z and its scalar dissipation rate χ [10, 23, 24]. The simplified flamelet equations for species and temperature read:

$$\rho \frac{\partial Y_k}{\partial t} = \frac{1}{2} \rho \chi \frac{\partial^2 Y_k}{\partial Z^2} + \dot{\omega}_k \tag{2.56}$$

$$\rho \frac{\partial T}{\partial t} = - \sum_{k=1}^{N} \Delta h^0_{f,k} \dot{\omega}_k + \frac{1}{2} \rho \chi \frac{\partial^2 T}{\partial Z^2} \tag{2.57}$$

where $\chi = 2D \left(\frac{dZ}{dx_i} \frac{dZ}{dx_i} \right)$ is a measure of the mixture fraction gradients and species fluxes towards the flame and D is the diffusion coefficient.

If χ is specified, the flame structure can be computed through the solution of Equation 2.56 and Equation 2.57 using detailed chemistry. Thermochemical properties are then tabulated into flamelet libraries and the mean species mass fractions and temperatures can then be obtained by assuming a PDF functional form relationship [11, 25].

$$T = T(z, t) \tag{2.58}$$

$$Y_k = Y_k(z, t) \tag{2.59}$$

$$\overline{\rho}\widetilde{Y_k} = \int_0^{+\infty} \int_0^1 \rho Y_k(Z, \chi) p(Z, \chi) dz d\chi \tag{2.60}$$

$$\overline{\rho}\widetilde{T} = \int_0^{+\infty} \int_0^1 \rho T(Z, \chi) p(Z, \chi) dz d\chi \tag{2.61}$$

Generally, the transient terms in Equation 2.56 and Equation 2.57 are considered negligible as it is assumed that the characteristic time scales in the flamelet equations are much smaller than the flamelet lifetime. This is known as the Steady Laminar flamelet Model (SLFM) whose applicability is limited to very high Damköhler number (the ratio of flow to chemical time scale) flows, whereby local extinction of the flame does not occur. The basic flamelet approaches have been extended to include the effects of unsteadiness, flame curvature and radiative heat transfer [25, 26, 27]. One of the more popular models is the Representative Interactive Flamelet (RIF) model whereby the unsteady flamelet equations are solved between each CFD time-step [28, 29]. This ensures that chemical and physical time scales are decoupled as well as overcoming the implicit assumption of a slow scalar dissipation rate in the SLFM model. Additionally, RIF allows the inclusion of the transient pressure term that is present in the complete expression of Equation 2.57 (not shown here), which is necessary for any real combustion application. As the flamelet assumption implies that the thermochemical trajectories in state-space of a multi-dimensional flame will be similar to those found in corresponding one-dimensional flames. It is possible to construct a low-dimensional manifold by mapping the high dimensional thermochemical state space of flamelet solutions using detailed chemistry and reaction kinetics onto a low-dimensional manifold in composition space. This is the basis of the Flamelet Generated Manifold (FGM) method developed by van Oijen [30, 31] that will be discussed further in Section 4.2.

Coherent Flame Models (CFM)

The Coherent Flame Model initially developed for partially-premixed flames, is a phenomenological type model that assumes that a flame sheet divides the flow field into burned and unburned zones. The flame sheet is characterised by a flame surface density, Σ, which is one of the controlling parameters of this model as the reaction zones are assumed to be a function of the distortion of the flame-sheet front [32]. The CFM approach allows decoupling of chemistry - represented by a local burning rate $\dot{\Omega}_i$, from the turbulence - represented by flame surface density. As Σ will wrinkle, stretch and be transported by the flow field, the mean reaction rate is then expressed as the local reaction rate per unit of flame area:

$$\overline{\dot{\omega}} = \dot{\Omega}_i \Sigma \tag{2.62}$$

where $\dot{\Omega}_i$ is the local burning rate and is computed either from one-dimensional laminar flames or expressed as a function of the scalar dissipation rate or species molecular fluxes. The flame surface density is solved through an additional transport equation given as [33]:

$$\frac{\partial \Sigma}{dt} + \frac{\partial \tilde{u}_i \Sigma}{dx_i} = \frac{\partial}{\partial x_i}\left(\left(\frac{\mu_t}{Sc_t} + \frac{\mu}{Sc}\right)\frac{\partial \Sigma / \overline{\rho}}{\partial x_i}\right) + \left(P_1 + P_2 + P_3\right)\Sigma - D + P_k \tag{2.63}$$

where P_1, P_2, P_3 denote the flame surface production by turbulent stretch, mean flow dilation and thermal expansion respectively. D represents the destruction term and P_k is the production term during ignition. Treatment of non-premixed combustion was included by extending the CFM model to include a third zone, leading to what is known as the Extended Coherent Flame Model-3 Zones (ECFM-3Z) [34]. Initially, each computational cell is subdivided into three zones as shown in Figure 2.3:

- Unmixed fuel zone
- Unmixed air+EGR zone
- Mixed zone containing air+fuel+EGR

Auto-ignition, which occurs in the mixed zone is modelled using Tabulated Kinetics [35] whereby ignition delay values are tabulated prior to the CFD calculation. The TKI model solves 0D constant pressure reactors over a series of pressure, temperature, equivalence ratio, EGR and reaction progress levels, thereby accounting for a wide range of initial conditions experienced in a combustion device. After ignition has occurred, the premixed flame is solved using the flame surface density approach and the diffusion flame is solved with a mixing model. The evolution of the zones is computed via this mixing model and is based on local turbulent time scales as:

$$\frac{1}{\tau_m} = \beta_m \frac{\epsilon}{k} \tag{2.64}$$

where β_m is a model constant. More detailed descriptions of the ECFM-3Z model and its derivative the ECFM-CLEH (Combustion Limited by Equilibrium Enthalpy) can be found in [34, 36].

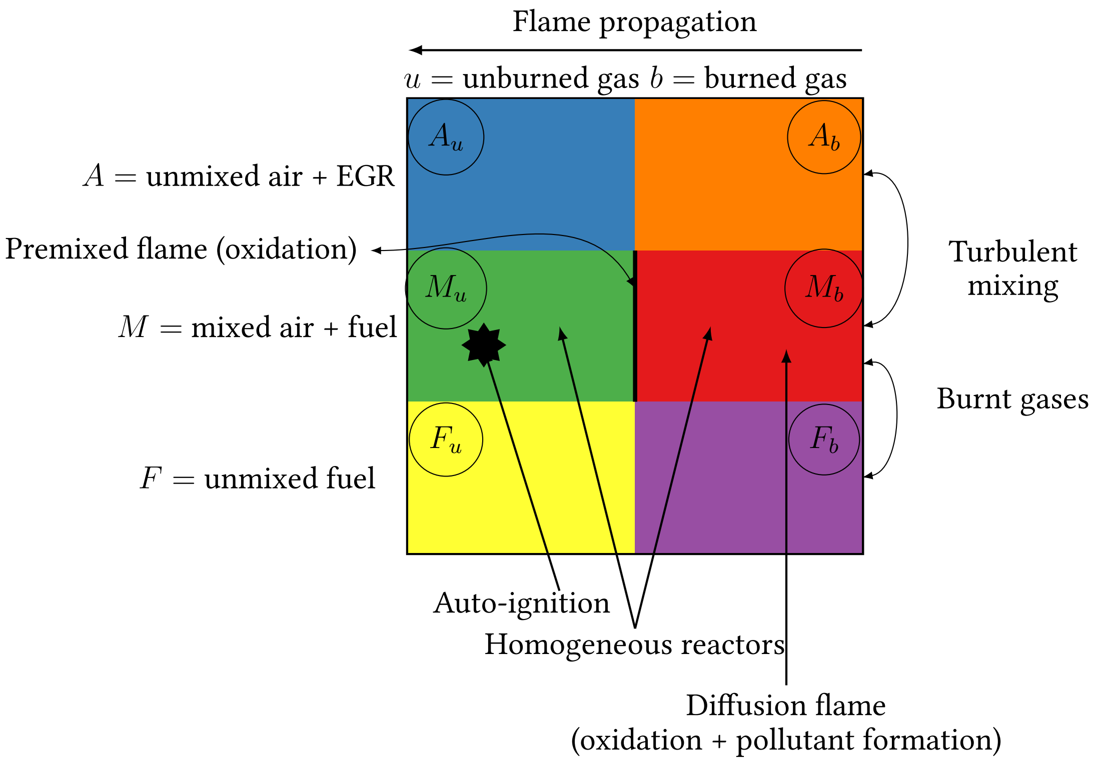

Figure 2.3: ECFM-3Z schematic. Adapted from [34]

Probability Density Function (PDF)

In PDF approaches, the mean reaction rate is recovered from integrating the conditional reaction rates weighted by their local PDF provided that the flow field is known. Either a balance equation for the PDF/joint-PDF is solved for relevant variables or a shape is assumed for the PDF. This PDF contains all the information equivalent to the standard moment methods at a particular point in time. The probability of finding a variable, Ψ at given location, $\vec{x}$ in time, t in the range, $[\Psi^* - \Delta\Psi/2, \Psi^* + \Delta\Psi/2]$ is defined as, $\overline{P} = (\Psi^*; \vec{x}, t)\Delta\Psi$, which obeys the following relations:

$$\int_{\Psi} \overline{P}(\Psi^*; \vec{x}, t) d\Psi^* = 1 \tag{2.65}$$

$$\int_{\Psi} \overline{P}(\Psi^*; \vec{x}, t) d\Psi^* = \overline{\Psi}(\vec{x}, t) \tag{2.66}$$

$$\int_{\Psi} (\Psi^* - \overline{\Psi})^2 \overline{P}(\Psi^*; \vec{x}, t) d\Psi^* = \widetilde{\Psi'^2}(\vec{x}, t) \tag{2.67}$$

where Ψ^* is the sample space variable for Ψ. For more than one variable, a joint probability density function can be applied as $\overline{P}(\Psi_1^*, ...\Psi_N^*; \vec{x}, t)$. Any mean quantity can then be expressed as:

$$\overline{\psi}_{\Psi_1}(\vec{x}, t) = \int_{\Psi_1} ... \int_{\Psi_N} \psi_{\Psi_1}(\Psi_1^*, ...\Psi_N^*) \overline{P}(\Psi_1^*, ...\Psi_N^*; \vec{x}, t) d\Psi_1^* ... d\Psi_N^* \tag{2.68}$$

Presumed PDF

A given shape is assumed for the PDF, which in non-premixed combustion can be derived by solving balance equations of the mean mixture fraction, $\widetilde{Z}$, and its variance, $\widetilde{Z''}$. Usually, the shape is that of a β-PDF as it has been found to appropriately characterise such flows [23, 37, 38, 39]. The mixture fraction which describes local composition is defined according to Bilger [40] as:

$$Z = \frac{2\frac{Y_C - Y_{C,2}}{M_C} + \frac{1}{2}\frac{Y_H - Y_{H,2}}{M_H} - \frac{Y_O - Y_{O,2}}{M_O}}{2\frac{Y_{C,1} - Y_{C,2}}{M_C} + \frac{1}{2}\frac{Y_{H,1} - Y_{H,2}}{M_H} - \frac{Y_{O,1} - Y_{O,2}}{M_O}} \tag{2.69}$$

where Y_k is the element mass fraction, M_k is the molar mass of the elements (Carbon (C), Hydrogen (H), Oxygen (O)) and subscripts 1,2, denoting the initial composition in the fuel and oxidiser streams respectively. This definition leads to $Z = 0$ in the oxidiser stream and $Z = 1$ in the fuel stream. The β-PDF of mixture fraction in Favre-averaged form is given as [39]:

$$\widetilde{P}\left(Z, \boldsymbol{x}, t\right) = \frac{Z^{\alpha-1}\left(1-Z\right)^{\beta-1}\Gamma\left(\alpha+\beta\right)}{\Gamma\left(\alpha\right)+\Gamma\left(\beta\right)} \tag{2.70}$$

where $\alpha = \widetilde{Z}\gamma$, $\beta = \left(1-\widetilde{Z}\right)\gamma$ and $\gamma = \frac{\widetilde{Z}\left(1-\widetilde{Z}\right)}{\widetilde{Z''}} - 1 \geq 0$

Transported PDF

First proposed by Pope [41], the transported PDF method solves the joint velocity-composition PDF instead of assuming a specific form of the PDF. Starting from the Navier-Stokes equations, the joint PDF $\hat{\mathcal{F}}\left(\boldsymbol{V}, \boldsymbol{\psi}, \boldsymbol{x}; t\right)$ of composition $\boldsymbol{\phi}\left(\boldsymbol{x}, t\right)$ and velocity is written as [42]:

$$\begin{aligned}
\frac{\partial \hat{\mathcal{F}}}{\partial t} + & \underbrace{\boldsymbol{V}_j \frac{\partial \hat{\mathcal{F}}}{\partial x_j} - \frac{1}{\rho}\frac{\partial \overline{p}}{\partial x_j}\frac{\partial \hat{\mathcal{F}}}{\partial \boldsymbol{V}_j} + \frac{\partial}{\partial \boldsymbol{\psi}_k}\left[\hat{\mathcal{F}}\dot{\omega}_k\right]}_{Closed} \\
= & \underbrace{\frac{\partial}{\partial \boldsymbol{V}_j}\left(\hat{\mathcal{F}}\left\langle \boldsymbol{v}\nabla^2 \boldsymbol{U}_j | \boldsymbol{V}, \boldsymbol{\psi}\right\rangle\right)}_{Viscous\,dissipation} \\
- & \underbrace{\frac{\partial}{\partial \boldsymbol{V}_j}\left(\hat{\mathcal{F}}\left\langle \frac{1}{\rho}\frac{\partial p'}{\partial x_j} | \boldsymbol{V}, \boldsymbol{\psi}\right\rangle\right)}_{Pressure\,fluctuation} \\
- & \underbrace{\frac{\partial}{\partial \boldsymbol{\psi}_k}\left[\hat{\mathcal{F}}\left\langle \Gamma\nabla^2 \boldsymbol{\psi}_k | \boldsymbol{V}, \boldsymbol{\psi}\right\rangle\right]}_{Molecular\,mixing}
\end{aligned} \tag{2.71}$$

Terms on the left hand side represent the time differential of the PDF, convective transport of the PDF in physical space by a random velocity field (including turbulent transport), convective transport of the PDF in velocity space and finally the chemical source term. The advantage of PDF transport models is that terms on the left hand side of Equation 2.71 are closed, hence the chemical source term is treated directly. The terms on the right hand side of Equation 2.71 remain unclosed and require modelling. The main difficulty with the transported PDF methods lies in the closure of these terms, where molecular mixing presents the greatest challenge [43], followed by the large computational costs. As transported-PDF methods are characterised by high dimensionality, finite-volume or finite-difference methods are not suitable as the computational expense increases exponentially with the number of scalars. Hence, alternative numerical methods are needed such as Monte-Carlo type methods, whereby the flow is described by a large number of particles whose individual properties are solved for using a stochastic Lagrangian approach [44]. A review on transported-PDF methods and their application to turbulent reacting flows can be found in Haworth [45].

Conditional Moment Closure (CMC)

Independently derived by Klimenko [46] and Bilger [47], CMC assumes that fluctuations in scalar quantities are dependent on the fluctuation of one principal quantity. In non-premixed combustion this principal quantity is the mixture fraction, as it has been observed that thermochemical quantities such as reaction rates and temperature are strongly correlated to the mixture fraction [11, 48, 49]. The conditional means of species mass fraction, Y_k and temperature, T, conditioned on the mixture fraction can be written as:

$$Q_k\left(\boldsymbol{x},t,\eta\right) = \left\langle Y_k\left(\boldsymbol{x},t\right)|Z\left(\boldsymbol{x},t\right)=\eta\right\rangle \tag{2.72}$$

$$Q_T\left(\boldsymbol{x},t,\eta\right) = \left\langle T\left(\boldsymbol{x},t\right)|Z\left(\boldsymbol{x},t\right)=\eta\right\rangle \tag{2.73}$$

where η is the sample space variable for the mixture fraction, Z. Following the decomposition method, as per Bilger [47], and substituting the conditional definitions into the species and energy equation, Equation 2.17 and Equation 2.16, the derived CMC transport equations for Q_k and Q_T read:

$$\frac{\partial Q_k}{\partial t} + \underbrace{\langle u_i|\eta\rangle\frac{\partial Q_k}{\partial x_i}}_{convection} - \underbrace{\langle N|\eta\rangle\frac{\partial^2 Q_k}{\partial \eta^2}}_{molecular\,mixing} + \underbrace{\frac{1}{\overline{\rho}\widetilde{P}\left(\eta\right)}\frac{\partial}{\partial x_i}\left[\langle\rho u_i'' Y_k''|\eta\rangle\widetilde{P}\left(\eta\right)\right]}_{diffusion} = \underbrace{\langle\dot{\omega}_k|\eta\rangle}_{chemical\,source} \tag{2.74}$$

$$\begin{aligned}
\frac{\partial Q_T}{\partial t} + \langle u_i|\eta\rangle \frac{\partial Q_T}{\partial x_i} &= \langle N|\eta\rangle \frac{\partial^2 Q_T}{\partial \eta^2} \\
&- \frac{1}{\overline{\rho}\widetilde{P}\left(\eta\right)} \frac{\partial}{\partial x_i} \left[\langle \rho u_i'' T''|\eta\rangle \overline{\rho}\widetilde{P}\left(\eta\right)\right] \\
&+ \langle N|\eta\rangle \frac{\partial Q_T}{\partial \eta} \left[\frac{1}{\langle c_p|\eta\rangle} \left(\frac{\partial \langle c_p|\eta\rangle}{\partial \eta} + \sum_{k=1}^{N} c_{p,k} \frac{\partial Q_T}{\partial \eta}\right)\right] \\
&+ \frac{\langle w_H|\eta\rangle}{\langle \rho|\eta\rangle \langle c_p|\eta\rangle} \\
&+ \frac{1}{\langle c_p|\eta\rangle} \left\langle \frac{1}{\rho}\frac{\partial p}{\partial t}|\eta \right\rangle
\end{aligned} \tag{2.75}$$

Solving these equations will provide the conditional mass fractions of all species and temperature for all locations and time in the flow field. As can be seen, no assumptions have been made regarding the scale/type of flow structures and turbulent/chemical time scales when compared to flamelet models. Furthermore, unlike transported PDF models, the computational expense and numerical challenges are greatly reduced as the CMC equations are conditional on the mixture fraction hence the dimensionality is lowered. However, terms remain unclosed in Equation 2.74 and Equation 2.75, the main ones being the conditional chemical source terms ($\langle \dot{\omega}_k|\eta\rangle$, $\langle \omega_H|\eta\rangle$), the conditional turbulent fluxes ($\langle u_i''\phi''|\eta\rangle$), the conditional scalar dissipation ($\langle N|\eta\rangle$) and the conditional veloctiy ($\langle u_i|\eta\rangle$). A number of methods have been developed to provide relevant expressions depending on flow characteristics [50, 51], closure can either be first order - using means and averages or second order - using variances and covariances of the fluctuations about their averages. Generally first order closure is employed, however, it has been found that for certain reacting flows where extinction or auto-ignition are present, second order closure is preferable with the inclusion of double conditioning (mixture fraction and scalar dissipation), although the computational cost increases quite considerably with these additions [51, 52, 53, 54, 55]. Assuming first order closure, the conditional mean of the chemical source term can be evaluated as a function of conditionally averaged scalars:

$$\langle \dot{\omega}_k|\eta\rangle \approx \dot{\omega}_k(Q_k, Q_T, \rho) \tag{2.76}$$

The unconditional mean chemical source term is then computed knowing the PDF of the mixture fraction as:

$$\overline{\dot{\omega}}_k = \int_0^1 \langle \dot{\omega}_k | \eta \rangle \, \overline{P}(\eta) d\eta \tag{2.77}$$

CMC has been used successfully to simulate turbulent non-premixed combustion in fuel sprays [56, 57, 58, 59, 60, 61] and pilot flames/jets [53, 54, 62, 63] with relatively successful predictions of auto-ignition, flame development and pollutant formation. It is apparent that successfully accounting for extinction, re-ignition and predicting auto-ignition requires higher order closures, but at an increase in computational expense, CMC becomes less attractive for use in practical applications. Hence, there is a need for a closure that benefits from the inherent generalism of CMC with regards to flame structure, but is less computationally demanding if higher order closures are used.

Conditional Source-Term Estimation (CSE)

Conditional Source term Estimation, first proposed by Bushe and Steiner [64], also uses conditional averages to evaluate the chemical source term, Equation 2.76. Unlike CMC, transport equations are not solved to determine the conditional averages, instead, CSE assumes spatial homogeneities exist on defined surfaces in the flow field leading to recovery of the conditional averages through inversion of Equation 2.77. Further details on CSE and its extension to spray combustion will be presented in Chapter 4.

2.6 Spray modelling

Chemical energy is commonly stored in liquid form in many combustion devices whereby mixing with oxidiser is achieved through high pressure injection of this fuel into (usually) hot gases. In the present work, multi-phase interactions are modelled using the Lagrangian-Eulerian framework. In this approach, conservation equations in the Lagrangian frame of reference are solved for each droplet with net rates of mass/energy/momentum exchanged with the gaseous (Eulerian frame) field through source/sink terms in the Favre averaged/filtered conservation equations. In practice, conservations equations are not solved for each droplet due to the excessive computational expense - but are solved for parcels. A parcel is a collection of droplets (many thousands) that have identical physical properties.

Droplet momentum transfer rate is given as:

$$\rho_l V_d \frac{dv_i}{dt} = F_{d,i} \tag{2.78}$$

the where ρ_l is the liquid density, V_d is the droplet volume and $F_{d,i}$ is the sum of drag $F_{drag,i}$ and gravitational $F_{g,i}$ forces acting on the droplet, which is expressed as:

$$F_{d,i} = F_{drag,i} + F_{g,i} = C_D A_f \frac{\rho_g |U_i|}{2} U_i + \rho_l V_d g_i \tag{2.79}$$

where C_D is the coefficient of drag, A_f is the droplet frontal area, ρ_g is the gas density and U_i is the drop-gas phase relative velocity given as:

$$U_i = u_i + u_i' - v_i \tag{2.80}$$

where u_i, u_i' denote the mean gas phase velocity at the droplet position and its fluctuation.

Droplet mass change rate is given by the Frossling correlation as [65]:

$$\frac{dr_o}{dt} = -\frac{\alpha_{spray} \rho_g D}{2 \rho_l r_0} B_d Sh_d \tag{2.81}$$

where α_{spray} is a mass transfer coefficient, D is the mass diffusivity of the liquid vapour in air, $\mathrm{Sh_d}$ is the Sherwood number and B_d is defined as:

$$B_d = \frac{Y_1^\star - Y_1}{1 - Y_1^\star} \tag{2.82}$$

where Y_1 is the vapour mass fraction and $Y_1^\star$ is the vapour mass fraction at the drop surface. The droplet energy equation based on the Uniform Temperature Model [65] assumes energy supplied to the droplet is either used to heat the droplet or supply heat for vaporisation.

$$c_l m_d^\star \frac{dT_d}{dt} = \overline{A}_d Q_d + \frac{dm_d}{dt} H_{vap} \tag{2.83}$$

where c_l is the liquid specific heat, T_d is the droplet temperature, $m_d$is the droplet mass and H_{vap} is the latent heat of vaporisation. The rate of heat conduction Q_d is given by the Ranz-Marshall correlation [66] .

A number of physical processes act on these parcels which include, but are not limited to: droplet breakup, collisions, evaporation, wall-interactions and turbulent dispersion. The sub-models used to account for these physical processes will be stated and referenced in the relevant chapters and the reader is referred to the original publications if more detail is required.

CHAPTER 3

Single cylinder research engine simulations

The content in this chapter is a result of the collaborative efforts of the author and Dr. Felix Leach and Dr. Nick Papaioannou. The author was responsible for all engine computational modelling, its post-processing and analysis. Dr. Felix Leach and Dr. Nick Papaioannou were responsible for the experimental measurements and analysis. The content in this chapter has been published in [4, 5, 6, 7].

3.1 Introduction

Diesel combustion is diffusion dominated, thus controlling and optimising of the combustion process relies on strategies that influence fuel-air mixing in the combustion chamber. Modern diesel engines adopt a variety of methods which include a combination of geometrical, fuel injection and flow adapting parameters [67]. For example, multiple injection events at high pressures are typically used to increase air entrainment by the fuel jet and thus improve mixing which in turn improves combustion efficiency and reduces soot formation [67, 68, 69, 70]. Geometrical considerations such as stepped piston bowls have been used extensively in medium duty diesel engines due to their effectiveness at improving air utilisation, enhancing late cycle mixing and reducing heat transfer losses [71, 72]. Their use in light-duty diesel engines is actively being explored with early findings reporting improvements in fuel efficiency and emissions as a result of this better mixing, especially late in the cycle [73, 74, 75]. From these investigations it is apparent that optimal matching of these parameters is key to designing cleaner and more efficient engines. The following investigation explores the effects of changes to spray targeting and combustion bowl shape and their respective influence on combustion evolution and emissions formation in a high speed light duty diesel engine. Simulations validated at baseline experimental conditions are run on a range of test points corresponding to an array of physical experiments recently carried out on a newly commissioned single cylinder research engine. These validated results are used to explain some of the significant findings in the experimental data.

3.2 Experimental test conditions

Experimental data is obtained from a single cylinder research engine based on the Ricardo Hydra platform [76]. The cylinder head, engine geometry and combustion system are identical to the Jaguar Land Rover AJ200D “Ingenium” engine. Table 3.1 gives an overview of the main engine specifications with a schematic of the test cell shown in Figure 3.1. The engine is fitted with a standard production injection system with an eight-hole injector based on the Bosch CRI2 platform. A comprehensive description of the test engine and measurement instrumentation can be found in [4].

Table 3.1: Engine specification

Valve per cylinder [-]	2 intake, 2 exhaust
Bore x Stroke [mm]	83 x 92.3
Displacement [mm^3]	500
Compression Ratio [-]	15.4:1
Fuel rail pressure [bar]	400-1800
Injector mechanism [-]	Solenoid
Injector nozzle diameter [μm]	124
Injector umbrella angle [deg.]	156

The experimental test points simulated are shown in Table 3.2, these include two part load test points in which the engine was run with varying EGR rate at constant

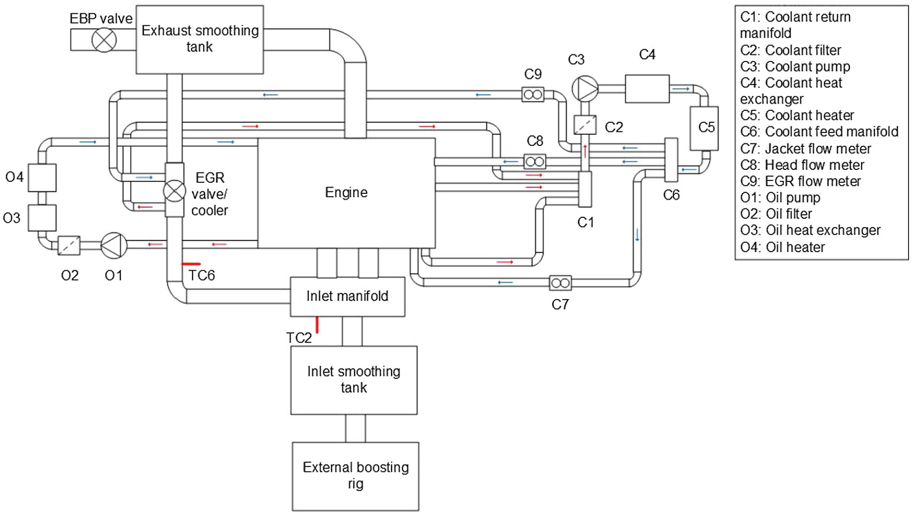

Figure 3.1: Schematic of engine test cell. Adapted from [77]

Table 3.2: Simulated experimental test points

	P1	P2	F1	F2	F3
Engine speed [rpm]	1500	1750	1500	2000	4000
Net IMEP [bar]	6.8	13.5		Max	
EGR level [%]	0,20,40	0,16,25	0	0	0
Fuel rail pressure [bar]	550	900	1100	1450	1800
Inlet manifold pressure [bar]	0.25	1.0	1.55	1.85	1.95
Inlet manifold air temperature [℃]	Varies with EGR		40	45	50
Exhaust back-pressure [bar]	0.45	1.4	1.9	1.75	2.5

exhaust back-pressure and inlet manifold pressure. The engine load was set by adjusting the main injection fuel quantity to reach the desired nIMEP value, this was then held constant throughout the EGR sweep. Additionally, three full load test points at zero percent EGR and varying engine speed were run where injection timing advance was limited by peak in-cylinder pressure and injected fuel quantity was limited by exhaust temperature. Each test point was simulated for two piston bowls at two Nozzle Tip Protrusion (NTP) values. The main details of the piston bowl geometry and fuel injector are shown in Figure 3.2. The piston bowls include one standard re-entrant type piston and one stepped-lip piston bowl as shown in Figure 3.3. NTP was varied by +0.5 mm from the baseline value of 2.25 mm by adding washer of relevant thickness to the injector mount.

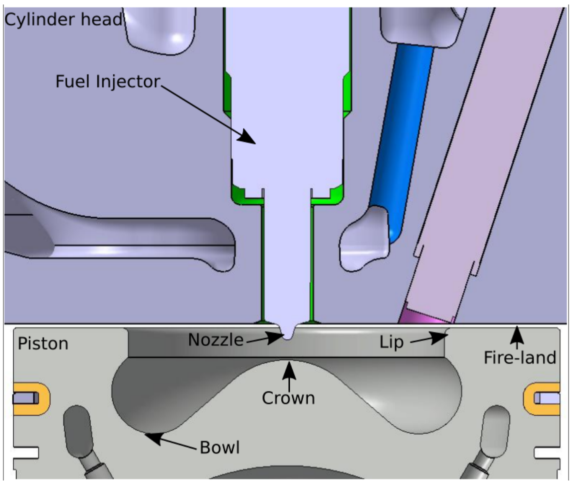

Figure 3.2: Cross-sectional view of 3D CAD model showing injector position and piston bowl geometry.

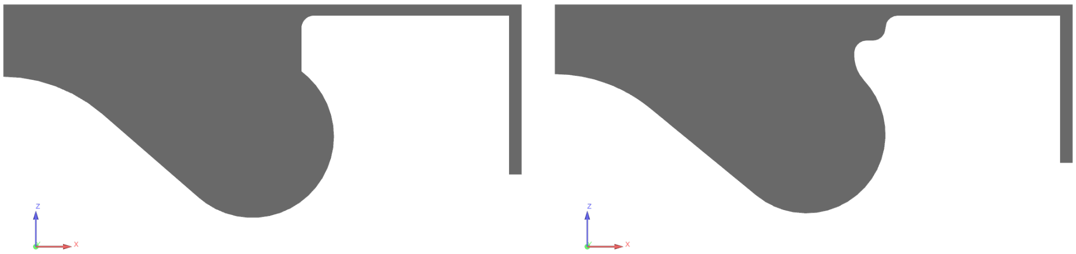

(a) Re-entrant

(b) Stepped-lip

Figure 3.3: Sectional view of piston bowl geometries highlighting piston-lip.

3.3 Computational setup

Simulations were performed using the CONVERGE CFD code version-2.4.15 [78]. The Pressure Implicit with Splitting of Operators (PISO) of Issa [79] was used to solve the transport equations. All transported variables in CONVERGE are colocated at the centre of the cell, hence, the Rhie-Chow [80] algorithm was adopted to prevent checker-boarding. Second-order accurate central differencing schemes were used for spatial discretization in all simulations, with fully implicit first-order accurate time integration to maintain stability. A variable time-step was used based on the Courant-Friedrichs-Lewy (CFL) condition for convection (CFL$_u = u\frac{\Delta t}{\Delta x}$), diffusion (CFL$_\nu = \nu\frac{\Delta t}{\Delta x^2}$) and speed of sound (CFL$_c = c\frac{\Delta t}{\Delta x}$). Here, Δx is the grid size, Δt is the time-step, u is the cell velocity, ν is the dynamic viscosity and c is the speed of sound. Additionally, spray and chemistry based time-step control are also used whereby the time-step is computed as:

$$dt_{spray} = \min\left[\frac{\Delta x}{u_{parcel}}\right] \cdot mult_{spray} \tag{3.1}$$

and:

$$dt_{chem} = dt_{i-1}\left[\frac{\Delta T}{T}\right] \cdot mult_{chem} \tag{3.2}$$

where u_{parcel} is the spray parcel velocity, $mult_{spray}$ is a user specified multiplier that limits the number of cells a parcel can travel in one time-step, dt_{i-1} is the last time-step, T is the cell temperature, ΔT is the change in temperature due to combustion and $mult_{chem}$ is a user specified multiplier that limits the maximum temperature rise within a time-step. Further details on time-step control can be found in [78]. From the initial time-step, the code will attempt to increase the time-step by 25%, if convergence is not achieved with this time-step or if the time-step control criteria above are exceeded then the time-step will be reduced. The input parameters for time-step control are shown in Table 3.3, these settings lead to a time-step which varied between $5 \cdot 10^{-7}$ s to $9 \cdot 10^{-6}$ s.

Table 3.3: Time-step control input parameters.

	Value
Initial time-step [s]	1e-7
Maximum time-step [s]	1e-5
CFL$_u$ [-]	1.0
CFL$_\nu$ [-]	2.0
CFL$_c$ [-]	50.0
$mult_{spray}$ [-]	1.5
$mult_{chem}$ [-]	0.5

Combustion was modelled using the ECFM-3Z model with ignition accounted for using the Tabulated Kinetic Ignition (TKI) model as described in Section 2.5.3. The TKI table was generated using n-Heptane fuel with the Chalmers kinetic mechanism of 42 species and 168 reactions [81]. The Chalmers n-Heptane mechanism was chosen as it has been successfully used for constant volume spray combustion simulations and diesel engine simulations over a wide range of operating points [81, 82]. All TKI computations were done using a detailed chemistry solver [83] for the range of initial conditions given in Table 3.4.

Table 3.4: TKI input parameters.

	Min	Max	Discretisation points
Pressure [bar]	1	200	12
Temperature [K]	500	1500	56
EGR [%]	0	80	4
Equivalence ratio [-]	0.1	3	9
Reaction progress [-]	0	1	99

Turbulence was modelled with the RANS RNG k-ϵ model as described in Section 2.4 with model constants given in Table 3.5. Wall heat transfer was taken into account using the model of Han & Reitz [84]. The well known Lagrangian-Eulerian framework was used to model the liquid phase where all sub-models used are stated in Table 3.6.

Table 3.5: RNG k-ϵ model constants

C_μ	$1/Pr_k$	$1/Pr_t$	$C_{\epsilon 1}$	$C_{\epsilon 2}$	$C_{\epsilon 3}$	β	η_0	c_s	c_{ps}
0.0845	1.39	1.39	1.42	1.68	-1.0	0.012	4.38	0.0	0.03

Table 3.6: Engine simulation discrete phase sub-models

Spray sub-models	
Injection	Blob method [85]
Droplet breakup	KH-RT without breakup length [86, 87]
Droplet drag	Dynamic droplet drag [88, 89]
Droplet collisions	No Time Counter [90]
Vaporisation	Frossling correlation [65]
Droplet heat transfer	Ranz-Marshall [66]
Turbulent dispersion	O'Rourke [65]
Wall film	Kuhnke [91]

Table 3.7: KH-RT breakup model constants

B_0	B_1	C_1	C_t	C_{RT}
0.61	7.0	0.188	1.0	0.1

NO_x formation is primarily attributed to thermal NO_x, hence, the Extended Zeldovich Mechanism [92] was used to calculate NO formation as:

$$\begin{aligned} \mathrm{O} + \mathrm{N_2} &\rightleftharpoons \mathrm{NO} + \mathrm{N} \qquad [\mathrm{R1}] \\ \mathrm{N} + \mathrm{O_2} &\rightleftharpoons \mathrm{NO} + \mathrm{O} \qquad [\mathrm{R2}] \\ \mathrm{N} + \mathrm{OH} &\rightleftharpoons \mathrm{NO} + \mathrm{H} \qquad [\mathrm{R3}] \end{aligned} \tag{3.3}$$

The principle pathways of NO formation are described in reactions [R1]-[R3], these include, high temperature oxidation of N_2, oxidation of nitrogen from the dissociation of oxygen and finally, bonding of unstable atoms of nitrogen with hydroxyl radicals that are formed during combustion. The concentration of O and OH radicals is computed using the assumption of equilibrium state of combustion reactions. This is deemed possible due to the kinetics of thermal NO_x formation rates being slower than main hydrocarbon oxidation rates, as such, most thermal NO_x is formed once combustion is complete. The extended Zeldovich mechanism only describes NO formation, hence, NO_x is predicted by multiplying the amount of NO by the ratio of molecular weights between NO_2 and NO which is 1.533. An extensive description of the model and reaction rate constants can be found in [93]. The empirical model of Hiroyasu *et al.* [94] coupled with the Nagle and Strickland-Constable (NSC) model [95] were used to model soot formation and oxidation respectively. In the Hiroyasu model, soot mass within a computational cell is determined from a single-step competing reaction between soot formation and soot oxidation:

$$\frac{dM_s}{dt} = \dot{M}_{sf} - \dot{M}_{so} \tag{3.4}$$

The formation rate is based on an Arrhenius type expression as:

$$\dot{M}_{sf} = SF \times M_{form} \tag{3.5}$$

$$SF = A_{sf} p^{0.5} \exp\left(-\frac{E_{sf}}{RT}\right) \tag{3.6}$$

where M_{form} is the mass of soot formation species, p is cell pressure, T is temperature, E_{sf} is the activation energy and A_{sf} is the Arrhenius pre-exponential factor.

The NSC model is based on experiments of carbon graphite oxidation over a range of partial pressures. This model considers carbon oxidation through two mechanisms which depend on surface chemistry interactions between more-reactive sites, A, and less-reactive sites, B. The soot oxidation rate is given as:

$$\dot{M}_{so} = \frac{6M_s}{\rho_s D_s} R_{total} MW_c \tag{3.7}$$

where M_s, ρ_s, D_s are the soot particle mass, density and diameter respectively. R_{total} is the net reaction rate of the reactions between reactive sites A and B, and MW_c is the molecular weight of carbon. Further details on the soot model can be found in [93].

Taking into account symmetry of the equispaced eight-hole injector and combustion chamber geometry, only a 45°sector was simulated from intake valve closing (IVC) to before exhaust valve opening (EVO) to reduce runtime. Expectedly, results will differ compared to simulations of a complete combustion chamber geometry, however, trends have been shown to be comparable between the two approaches by [96]. A structured grid is generated at runtime with adaptive mesh refinement enabled to refine regions of interest. Furthermore, fixed grid refinements are placed in the near nozzle region and along combustion chamber boundaries. Adaptive mesh refinement will refine regions where the sub-grid fluctuations of a variable increase above a user specified value. The sub-grid field, ϕ', for a scalar is the difference between the actual field, ϕ, and resolved field, $\overline{\phi}$:

$$\phi' = \phi - \overline{\phi} \tag{3.8}$$

From Bedford *et al.* [97] and Pomraning [98], the sub-grid field for any scalar can be expressed as an infinite series as:

$$\phi' = -\alpha_{[k]} \frac{\partial^2 \overline{\phi}}{\partial x_k \partial x_k} + \frac{1}{2!} \alpha_{[k]} \alpha_{[l]} \frac{\partial^4 \overline{\phi}}{\partial x_k \partial x_k \partial x_l \partial x_l} + ... \tag{3.9}$$

where $\alpha_{[k]} = {}^{dx_k^2}\!/_{24}$ for a rectangular cell and brackets [] indicating no summation. As it is not possible to evaluate an infinite series, only the first term is used to approximate the sub-grid value i.e:

$$\phi' \cong -\alpha_{[k]} \frac{\partial^2 \overline{\phi}}{\partial x_k \partial x_k} \tag{3.10}$$

If the sub-grid value rises above the user specified value, a cell will be refined, conversely, if the sub-grid value is $^1/_5$th of the user specified value, then the cell will be coarsened. In the following engine simulations, AMR is based on velocity and temperature fluctuations with sub-grid criteria set at 1 ms^{-1} and 5 K respectively. The refinement cell sizes are functions of a base cell size and embed scale, which is defined as follows:

$$\text{Cell size} = \text{base cell size} \times 2^{\text{-embed scale}} \tag{3.11}$$

The base cell size for all engine simulations has been set at 1.4 mm. An overview of the computational domain with fixed embedding regions, AMR and visualisation plane definitions is shown in Figure 3.4.

All engine simulations were initialised with experimentally measured in-cylinder pressure data at the relevant test point. Initial species concentrations were computed from chemical equilibrium balance at the experimental air-fuel ratio assuming

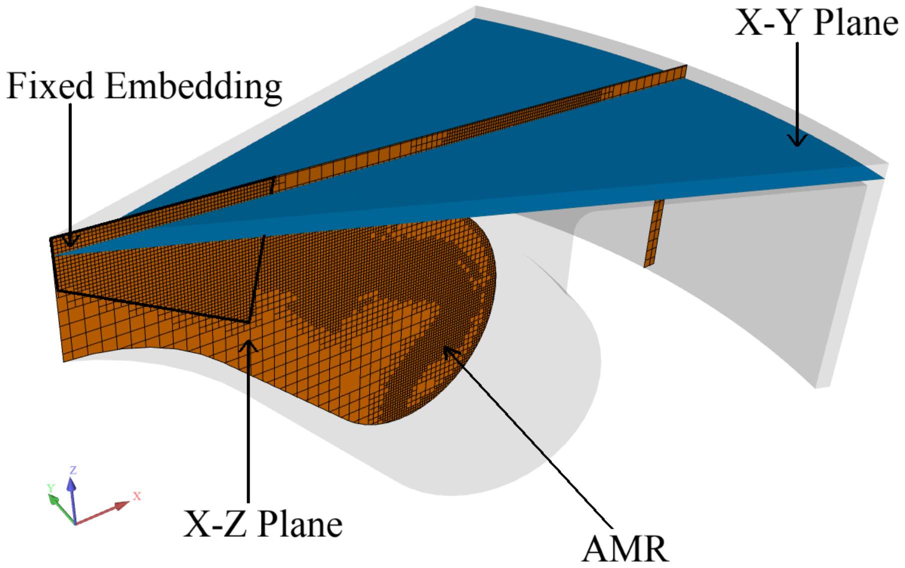

Figure 3.4: Computational domain showing regions of refinement and visualisation planes.

incomplete combustion and eight species as by-products following the methodology of Silvis *et al.* [99]. A complete description of this process can be found in Papaioannou [77]. In-cylinder flow was set using a swirl ratio determined from full-cycle simulations at the test point of interest. Wall temperature boundaries are computed from FEM thermal analysis and kindly provided by the industrial partner. Additionally, the fuel injection system is modelled using the AMEsim code where each physical component of the fuel injector is represented by a lumped parameter model. The output of this hydraulic model are injector flow-rate profiles which have also been provided by the industrial partner. Further details of the AMEsim hydraulic model can be found in [100].

3.4 Grid dependence

Grid dependence of the computational setup is examined by running a series of simulations where the embed scale is increased from 1 to 4: this corresponds to a reduction in cell size from 0.7 mm down to 0.0875 mm which is below the nozzle diameter. With Lagrangian-Eulerian spray modelling it is necessary to increase the

Table 3.8: Grid dependence parameters.

Grid	I	II	III	III-limit	IV
Embed level	1	2	3	3	4
Min cell size [mm]	0.7	0.35	0.175	0.175	0.0875
Spray parcels*1000 [-]	75	150	300	300	600
Max cell number*1000 [-]	110	240	840	400	3200
Runtime 64-cores [h]	0.2	0.5	6	4	72

number of spray parcels as the grid is refined, this is to ensure liquid penetration is not over-predicted as a result of negligible drag on parcels outside the core of the spray [101]. An overview of the grid setup can be seen in Table 3.8. From Figure 3.5 it can be seen that in-cylinder pressure and chemical heat release rate show a clear trend of increasing as the grid is refined from 0.7 mm to 0.175 mm. As the grid is refined further to 0.0875 mm the solution deviates away from the trend seen earlier with both in-cylinder pressure and peak chemical heat release rate both reduced compared to the 0.175 mm grid. This indicates that grid convergence has not been reached even at this level of refinement and further refinement would be needed to determine if a grid converged solution exists. These trends are observed for local variables where in Figure 3.6 the flame shape as given by the temperature field can clearly be seen to follow a similar pattern from 0.7 mm to 0.175 mm. At 0.0875 mm the flame shape differs quite considerably with flame lift-off being predicted much further downstream of the injector. Previous studies have also shown similar trends with an engines of this size using the same grid sizes [82, 102]. CONVERGE allows additional optimisation of grids, and consequently runtime, by allowing the user to specify a limit to the number of cells the adaptive mesh refinement algorithm can embed within a domain. The cell count was limited to 300,000 for a grid size of 0.0175 mm (Grid-III-limit in Table 3.8) and it was found that the solution does not differ much to Grid-III as seen in Figure 3.6. As such, Grid-III-limit was used for all engine simulations as it provided a reasonable compromise between accuracy and return time.

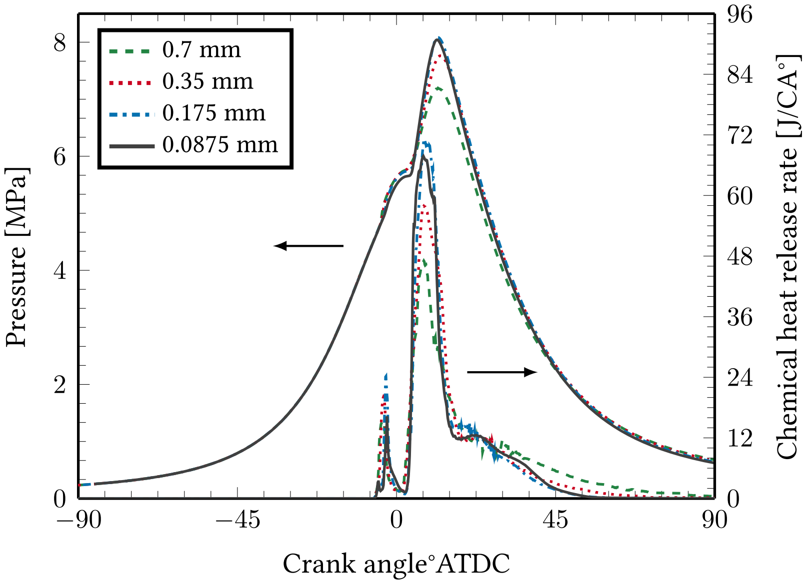

Figure 3.5: In-cylinder pressure and heat release rate for different cell sizes

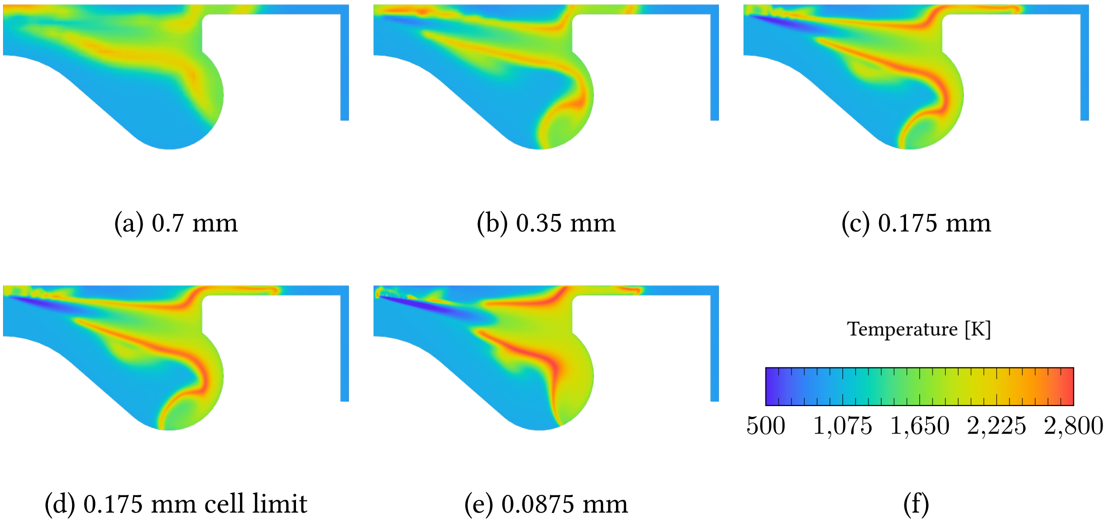

(a) 0.7 mm

(b) 0.35 mm

(c) 0.175 mm

(d) 0.175 mm cell limit

(e) 0.0875 mm

(f)

Figure 3.6: Temperature field for different cell sizes: X-Z plane, 10°ATDC

3.5 Computational setup validation

The computational setup described in previous sections was validated at the baseline condition for each test point: 0% EGR, NTP 2.25 mm with the re-entrant piston bowl. From Figure 3.7, the CFD model compares well to the experimental data at both part and full load test points. Some minor deviations can be seen during the pilot burn and after top dead centre which can be attributed to the uncertainty in the injector flowrate profiles and the imposed wall temperatures. As the flowrate profiles are generated from a dynamic 1D model of the injection system, accuracy of this input is dependent upon the extensiveness of the injector model and its relevant input. The wall temperatures applied to in-cylinder surfaces were generated through an iterative process of coupled CFD-FEM heat transfer studies where the combustion phase is first simulated using CFD with guessed wall temperatures, the heat transfer coefficient is then parsed as an input to an FEM simulation of the engine block which outputs spatial wall temperature data. This process is then looped until convergence. Furthermore, for the same wall temperature the choice of wall heat transfer model will greatly affect total heat flux. This is identical to previous studies [93, 103] which have shown the Angelberger model [104] to consistently under-predict heat flux, Han & Reitz model [84] to consistently over-predict heat flux and the O'Rourke model [65] to predict a heat flux between the two extremes. As such, the model of Han & Reitz was selected for this work as it produced closest prediction of total cumulative heat loss when compared to the experiment.

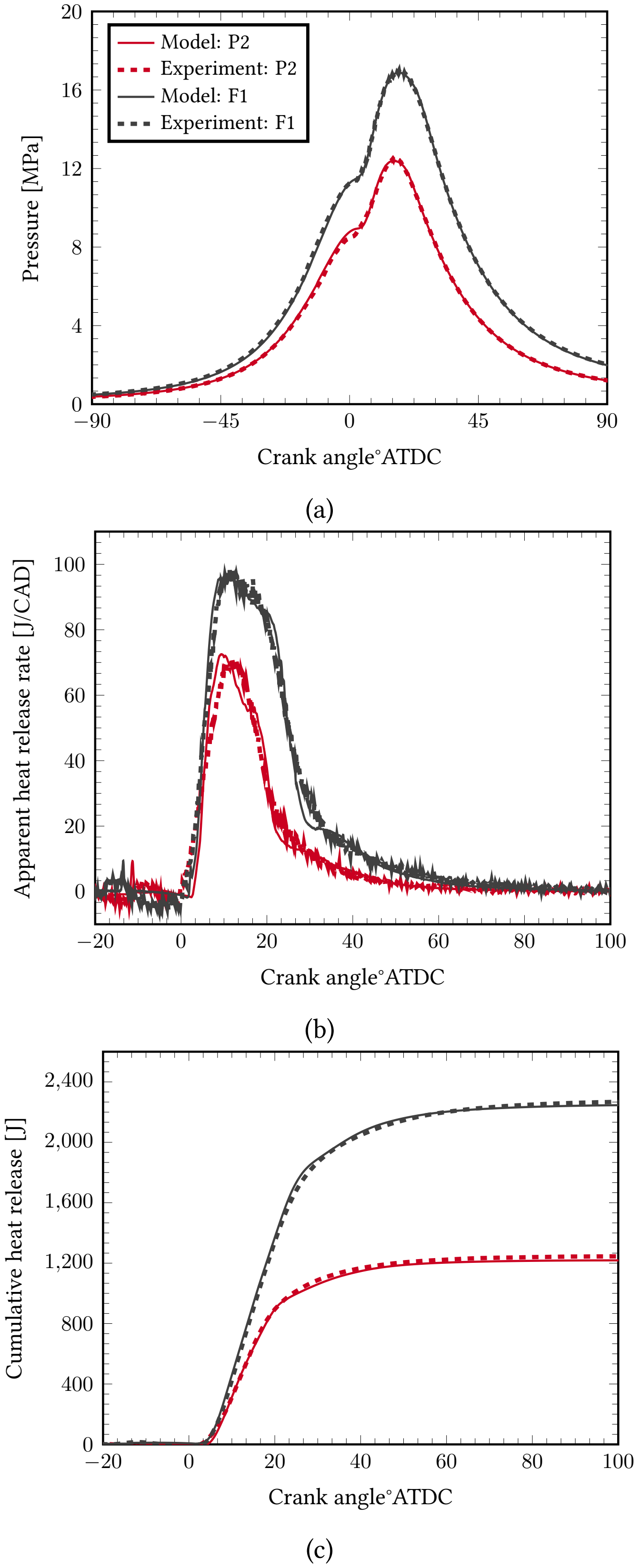

Figure 3.7: Comparison of experimental and CFD model for in-cylinder pressure (a), apparent heat release rate (b) and cumulative heat release (c).

3.6 Results and discussion

3.6.1 Part load

Figure 3.8 and Figure 3.9 show the NO_x-Soot trade-off at both part load test points for both bowls and NTP values. Experimental data is shown for three samples of the same test point in order to highlight typical spread in measured data. A good agreement between simulation and experiment is observed with major trends being predicted correctly for both test points. The deviations between experiment and simulation can be attributed in part, to variation in experimental EGR rate away from the nominal target value (which is exact in simulations). As expected, increasing EGR rate results in a reduction in NO_x emissions at an expense of increased soot emissions. It can be seen that NTP change has a much greater effect on NO_x-Soot trade-off than piston geometry with an increased NTP of 2.75 mm leading to a reduction in soot for both bowls across the EGR range with a marginal increase in NO_x. This effect is more pronounced at test point P2 with clear benefits seen for both bowls at all EGR rates.

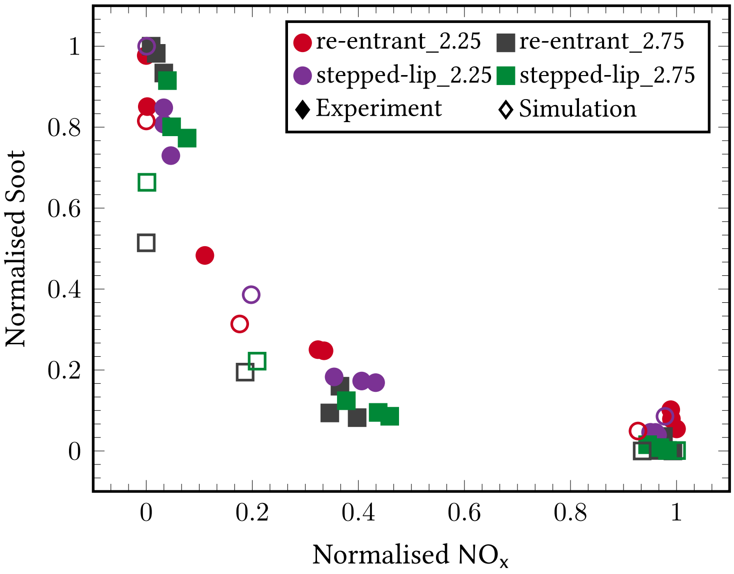

Figure 3.8: Normalised NO_x-Soot trade-off at test point P1 comparing both NTP and piston bowl across EGR range. Experimental NO_x and Soot in [ppm] and [FSN] respectively, Simulation NO_x and Soot mass in [kg]. Experimental data is represented by filled symbols and simulation results by hollow symbols.

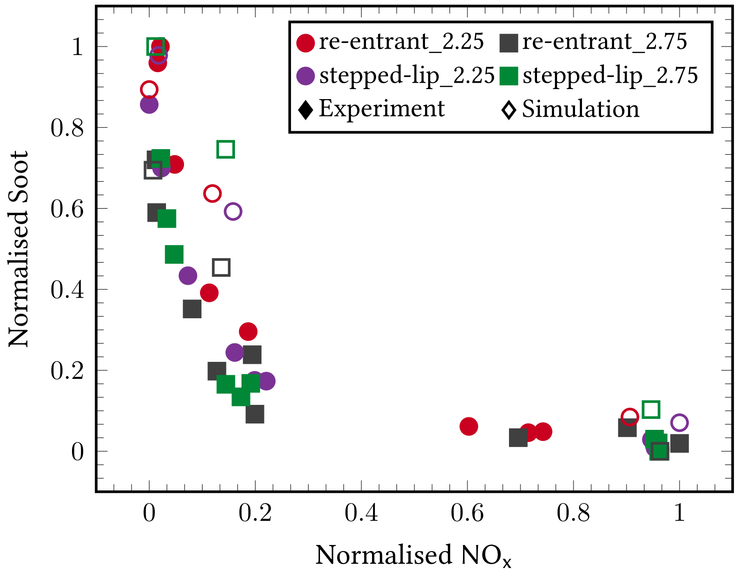

Figure 3.9: Normalised NO$_x$-Soot trade-off at test point P2 comparing both NTP and piston bowl across EGR range. Experimental NO$_x$ and Soot in [ppm] and [FSN] respectively, Simulation NO$_x$ and Soot mass in [kg].Experimental data is represented by filled symbols and simulation results by hollow symbols.

Figure 3.10 shows the formation, oxidation and cumulative soot mass for both NTP values at P1 where it is clear that soot formation is greatly increased at an NTP of 2.25 mm. As soot oxidation is based on the NSC model, it is expected that the much higher concentration of soot at NTP 2.25 mm will have a proportionally higher oxidation rate as Equation 3.7 is a function of soot concentration. The reason for higher soot formation at NTP 2.25 mm is explained through spray targetting: when increasing NTP to 2.75 mm, the spray jet is directed more towards the bowl region than fire-land as shown in Figure 3.11. The increased spray momentum in the bowl, (Figure 3.12) forces fuel vapour away from the piston walls and further towards the piston crown - increasing air entrainment and improving mixing as seen in Figure 3.13. This leads to less fuel-rich regions especially along the piston walls and consequently less soot formation in these regions as shown in Figure 3.14. Conversely, with the lower NTP of 2.25 mm, the fuel jet penetrates further into the fire-land region and impinges on the piston, resulting in high soot formation near the piston walls which can be seen clearly in Figure 3.15.

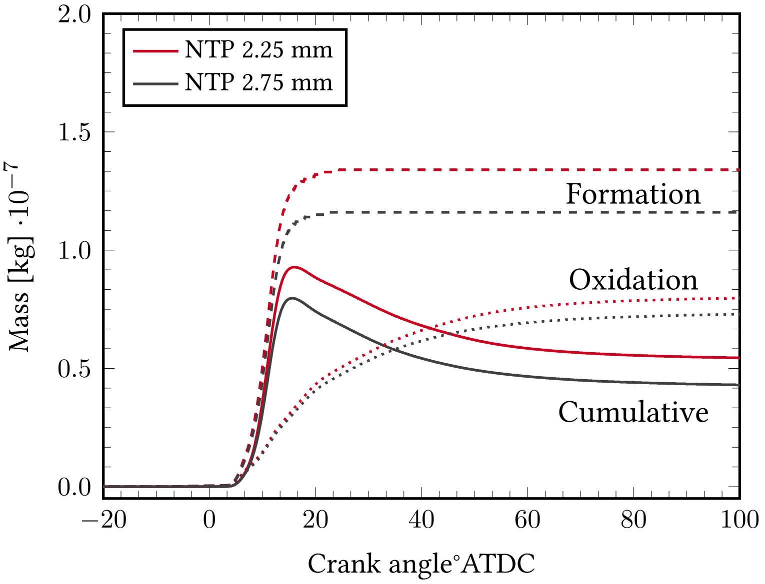

Figure 3.10: Soot formation, oxidation and cumulative soot mass for both NTP values with the re-entrant bowl at P1, 40% EGR.

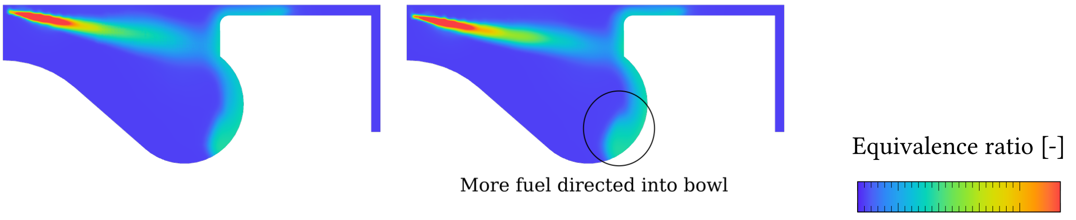

(a) NTP 2.25 mm

(b) NTP 2.75 mm

Figure 3.11: Equivalence ratio distribution for both NTP values at P1, 40% EGR: X-Z plane, 10°ATDC.

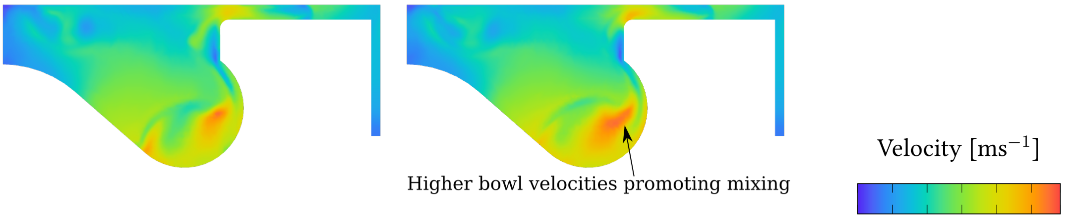

(a) NTP 2.25 mm

(b) NTP 2.75 mm

Figure 3.12: Velocity field for both NTP values at P1, 40% EGR: X-Y plane, 13°ATDC.

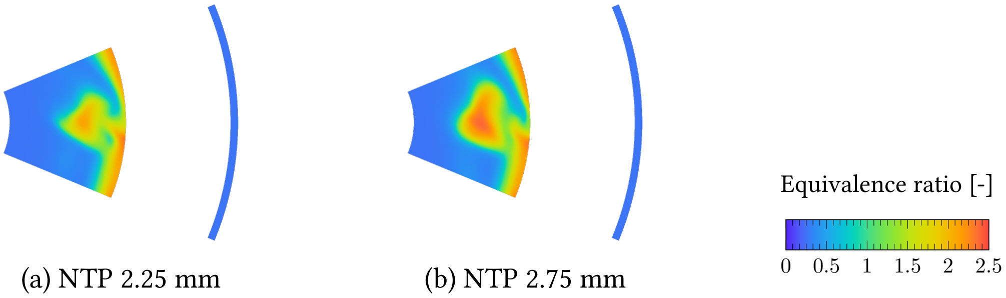

(a) NTP 2.25 mm (b) NTP 2.75 mm

Figure 3.13: Equivalence ratio distribution for both NTP values at P1, 40% EGR: X-Y plane, -12 mm from head, 13°ATDC.

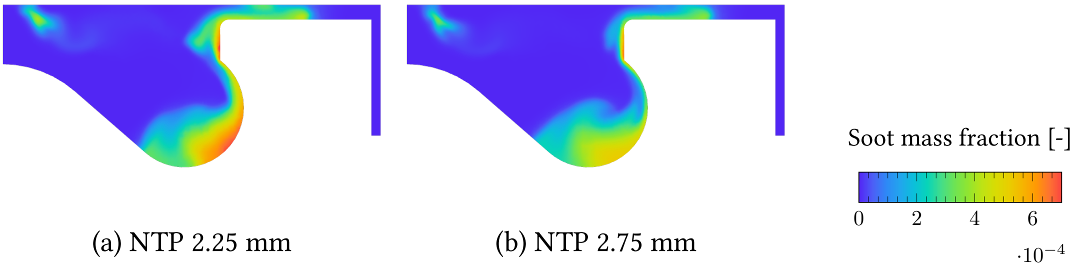

(a) NTP 2.25 mm (b) NTP 2.75 mm

Figure 3.14: Soot concentration for both NTP values at P1, 40% EGR: X-Z plane, 13°ATDC.

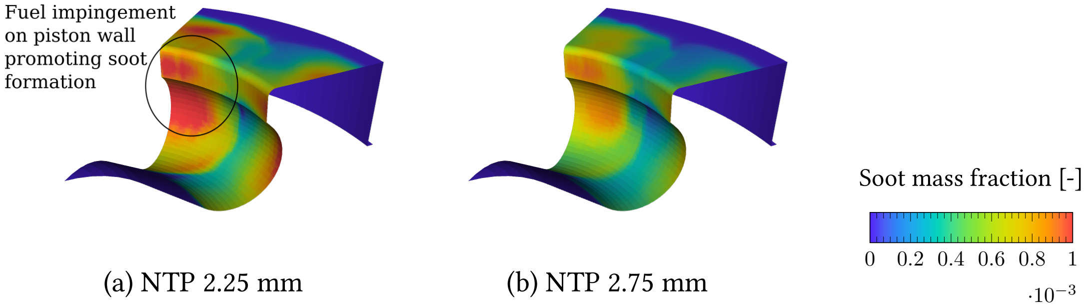

(a) NTP 2.25 mm (b) NTP 2.75 mm

Figure 3.15: Soot concentration along piston wall for both NTP values at P1, 40% EGR: 13°ATDC.

At the higher load point P2, soot formation between both NTP values is very similar as seen in Figure 3.16. At this load point, reduction in soot is due to soot oxidation through improved mixing in the later stages of the cycle. This is seen in Figure 3.17 and Figure 3.18 where the principle oxidising agent OH is higher in concentration as well as slightly more oxygen being consumed for an NTP of 2.75 mm.

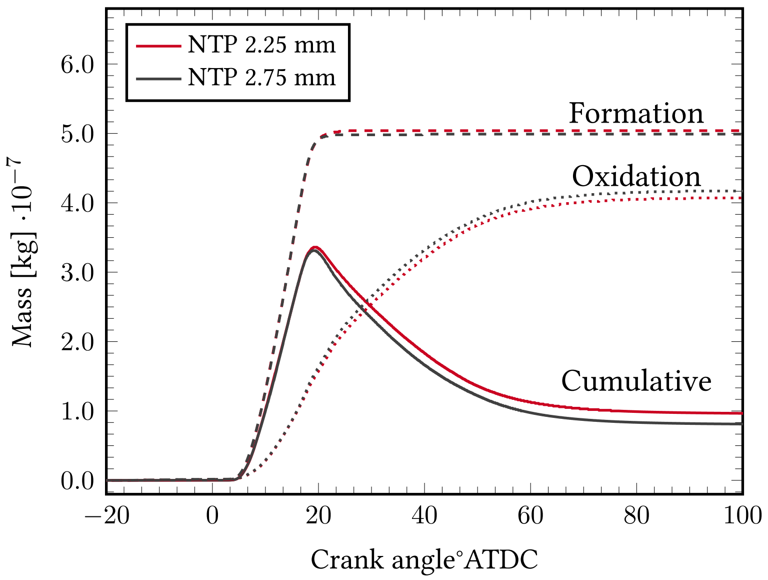

Figure 3.16: Soot formation, oxidation and cumulative soot mass for both NTP values with the re-entrant bowl at P2, 25% EGR.

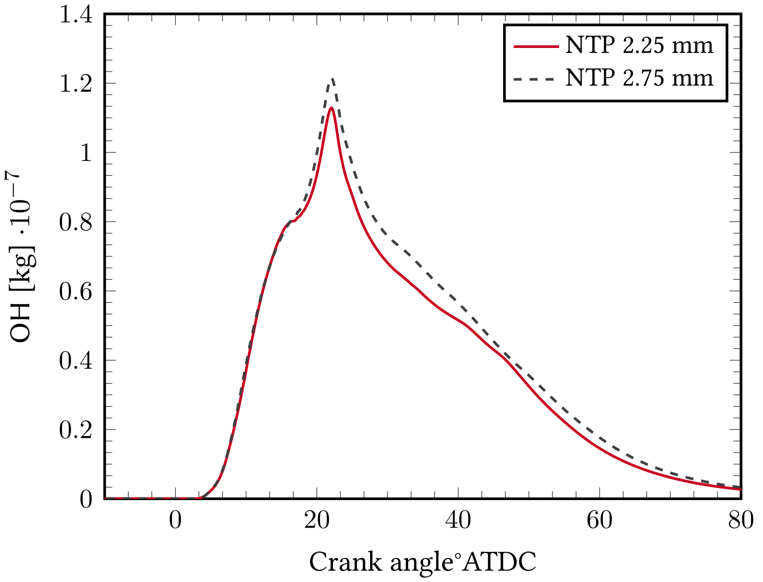

Figure 3.17: Volume averaged OH mass for both NTP values at P2, 24% EGR.

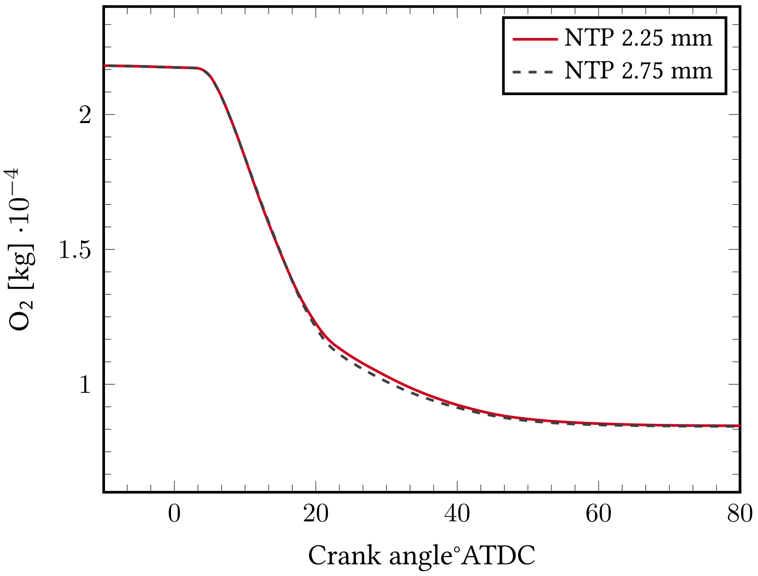

Figure 3.18: Volume averaged oxygen consumption for both NTP values at P2, 24% EGR.

From Figure 3.8 and Figure 3.9 it can be seen that experimentally for the same NTP value, the stepped-lip piston generally leads to lower soot with a marginal increase in NO_x. This trend is captured by the simulations for some points but not for others, this can partly be attributed to the variation in EGR rates away from the nominal value in the experiments. Additionally, as detailed in [7], the difference in soot emissions between piston bowls in the experiment is within one standard deviation and although the trends are consistent, there is limited statistical certainty in the measurements. A clear trend seen in both experiment and captured with simulations is the increase in NO_x with the stepped-lip piston. From Figure 3.19, the piston lip can be seen to impede the spray jet penetrating into the fire-land, leading to an accumulation of fuel vapour along the lip. Additionally, as the lip acts a forward facing step, once fuel injection ends, the loss of momentum leads to a low velocity zone forming in the lip region seen in Figure 3.20 and Figure 3.21.

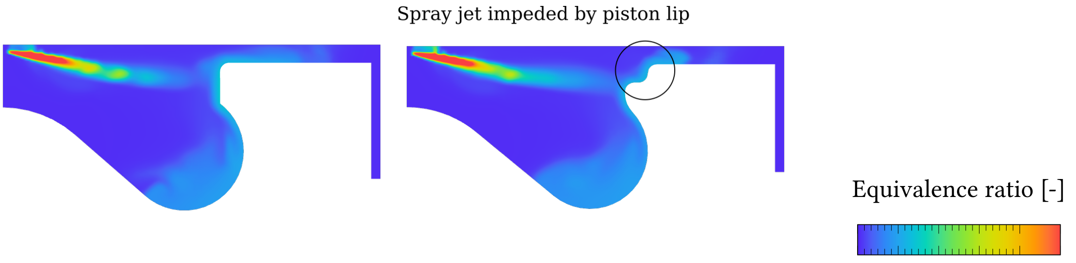

(a) Re-entrant (b) Stepped-lip

Figure 3.19: Equivalence ratio distribution for both piston bowls with NTP 2.25 mm at P2, 16% EGR: X-Z plane, 15°ATDC.

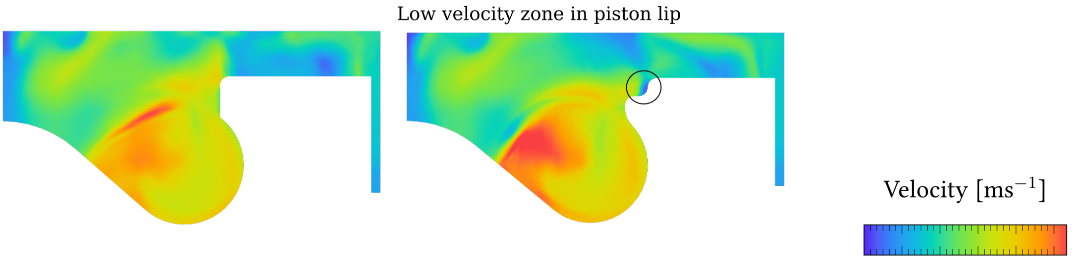

(a) Re-entrant (b) Stepped-lip

Figure 3.20: Velocity field for both piston bowls with NTP 2.25 mm at P2, 16% EGR: X-Z plane, 25°ATDC.

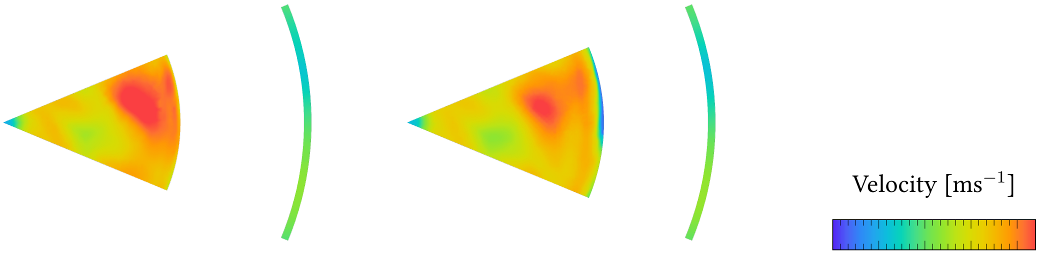

(a) Re-entrant (b) Stepped-lip

Figure 3.21: Velocity field for both piston bowls with NTP 2.25 mm at P2, 16% EGR: X-Y plane, -6 mm from head, 25°ATDC.

It is well known thermal NO_x is a function of high temperatures and residence time of nitrogen at those temperatures. As such, the effect of the piston lip is to increase the residence time due to the low velocity zones formed in the lip region. This coupled with high combustion temperatures (Figure 3.22) leads to areas of high NO_x in the vicinity of the lip as seen in Figure 3.23 and Figure 3.24. This can also be described with the equivalence ratio - temperature plots in Figure 3.25 and Figure 3.26 where combustion

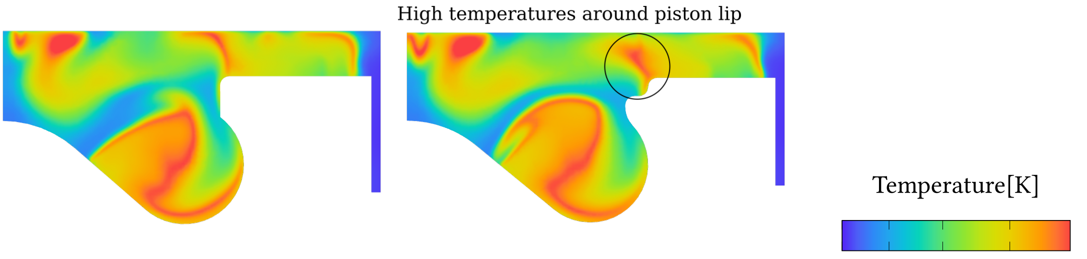
High temperatures around piston lip

(a) Re-entrant (b) Stepped-lip

Figure 3.22: Temperature field for both piston bowls with NTP 2.25 mm at P2, 16% EGR: X-Z plane, 25°ATDC.

in the stepped-lip piston extends towards the high temperature zones - especially later in the cycle.

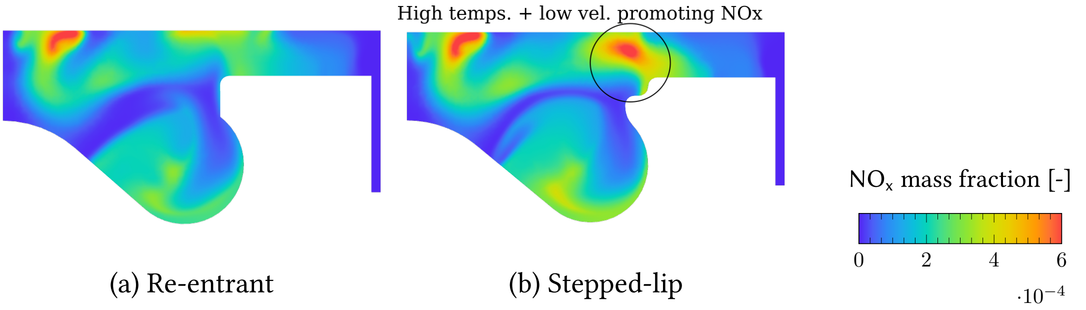
High temps. + low vel. promoting NOx

(a) Re-entrant (b) Stepped-lip

Figure 3.23: NO_x distribution for both piston bowls with NTP 2.25 mm at P2, 16% EGR: X-Y plane, 25°ATDC.

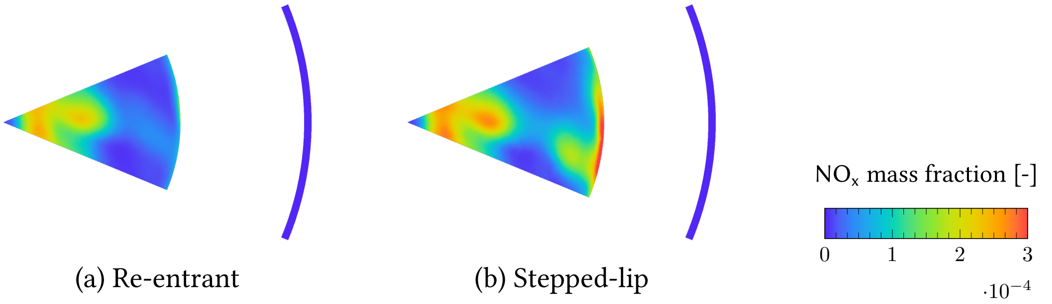

(a) Re-entrant (b) Stepped-lip

Figure 3.24: NO_x distribution for both piston bowls with NTP 2.25 mm at P2, 16% EGR: X-Y plane, -6 mm from head, 25°ATDC.

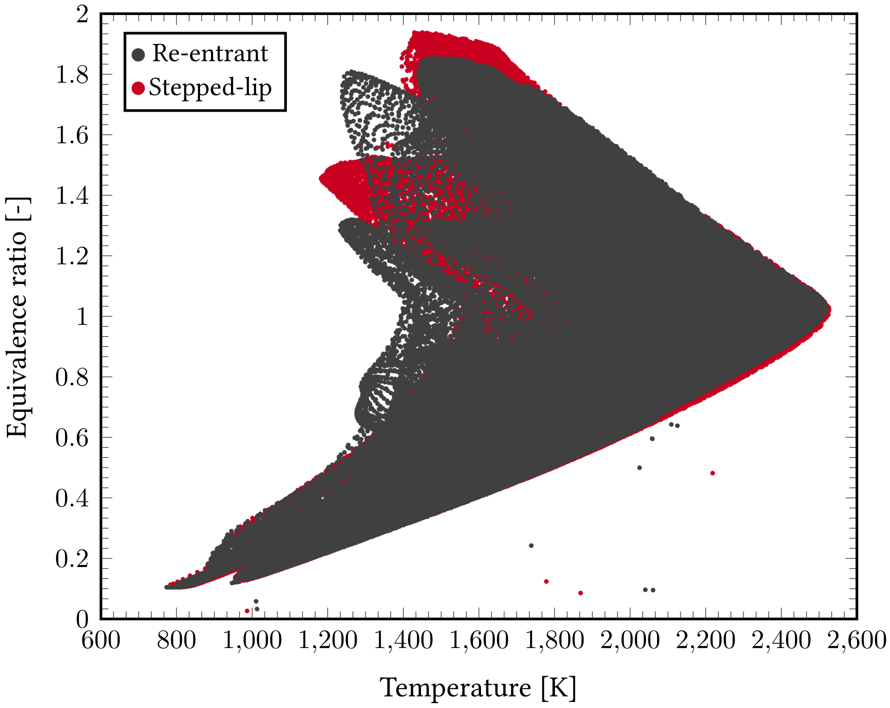

Figure 3.25: $\phi - T$ map at 25°ATDC for both bowls with NTP 2.25 mm at P2, 16% EGR.

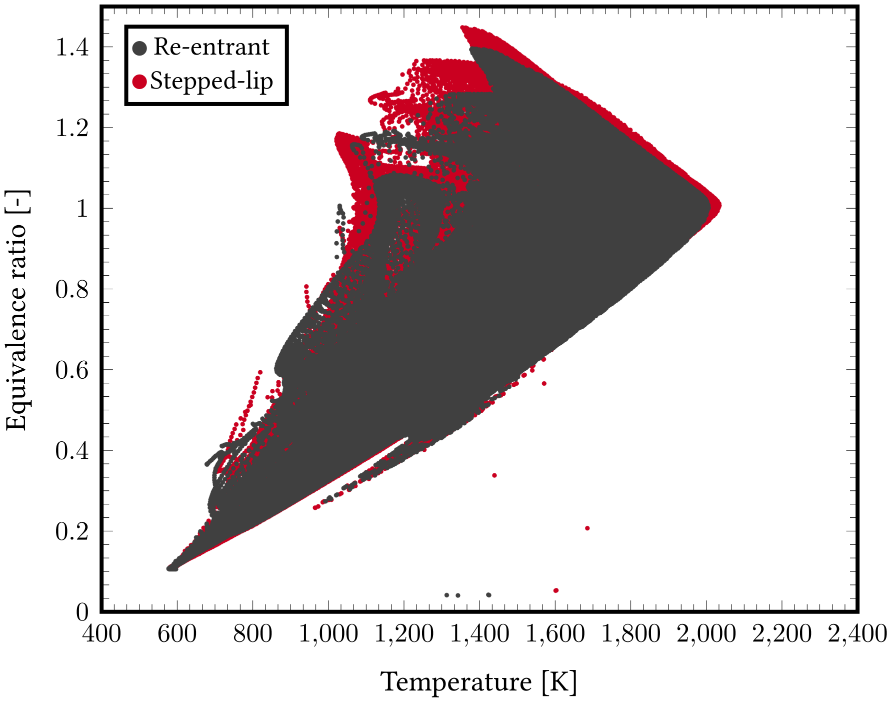

Figure 3.26: $\phi - T$ map at 50°ATDC for both bowls with NTP 2.25 mm at P2, 16% EGR.

The 90% MFB durations across the EGR range for both bowls, NTP values and test points can be seen in Figure 3.27 and Figure 3.28. NTP increase leads to a longer CA90 duration (≈ 0.5°-1.0°CA) for both piston bowls across the EGR range at P1. Simulation results agree well with experimental data in reproducing trends, however, magnitude of the differences (between piston bowl and NTP) is much less pronounced in simulation results.

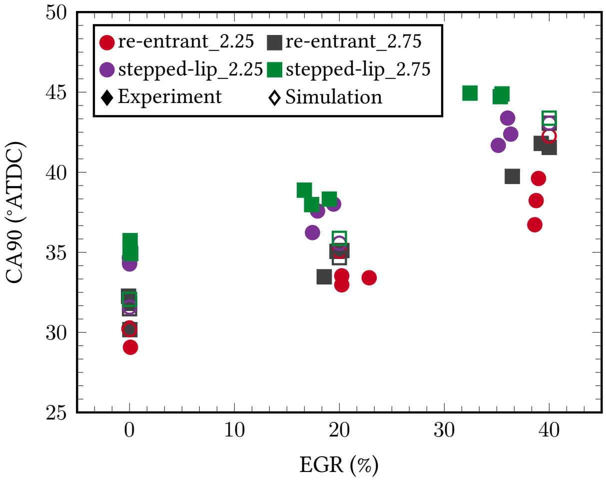

Figure 3.27: Crank angle of 90% MFB for both piston bowls and both NTP values at P1. Experimental data is represented by filled symbols and simulation results by hollow symbols.

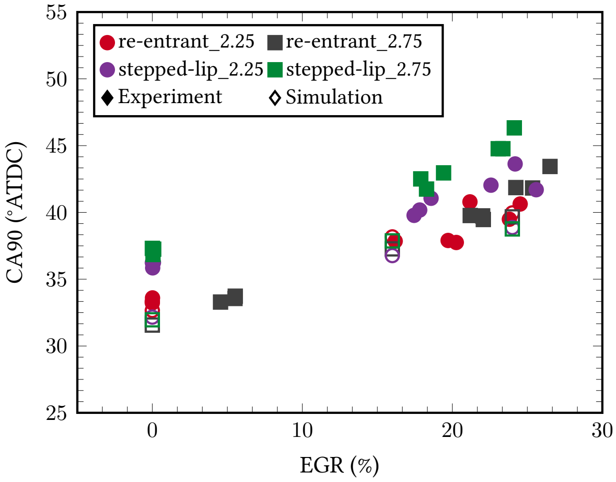

Figure 3.28: Crank angle of 90% MFB for both piston bowls and both NTP values at P2. Experimental data is represented by filled symbols and simulation results by hollow symbols.

The increase in burn duration at NTP 2.75 mm at P1 is attributed to spray targetting into the bowl region, which limits the amount of combustible mixture in the fire-land leading to slower combustion in this region. Figure 3.29 qualitatively describes combustion progression through the H_2O distribution where it is clear more H_2O has been produced for an NTP of 2.25 mm. Additionally, the unmixed fuel (gaseous fuel that has not entered the mixing zone in the ECFM-3Z model cf. Figure 2.3) is greater for the deeper NTP during the later stages of injection as shown in Figure 3.30, this leads to less time available for mixing and therefore, a reduction in burn rate.

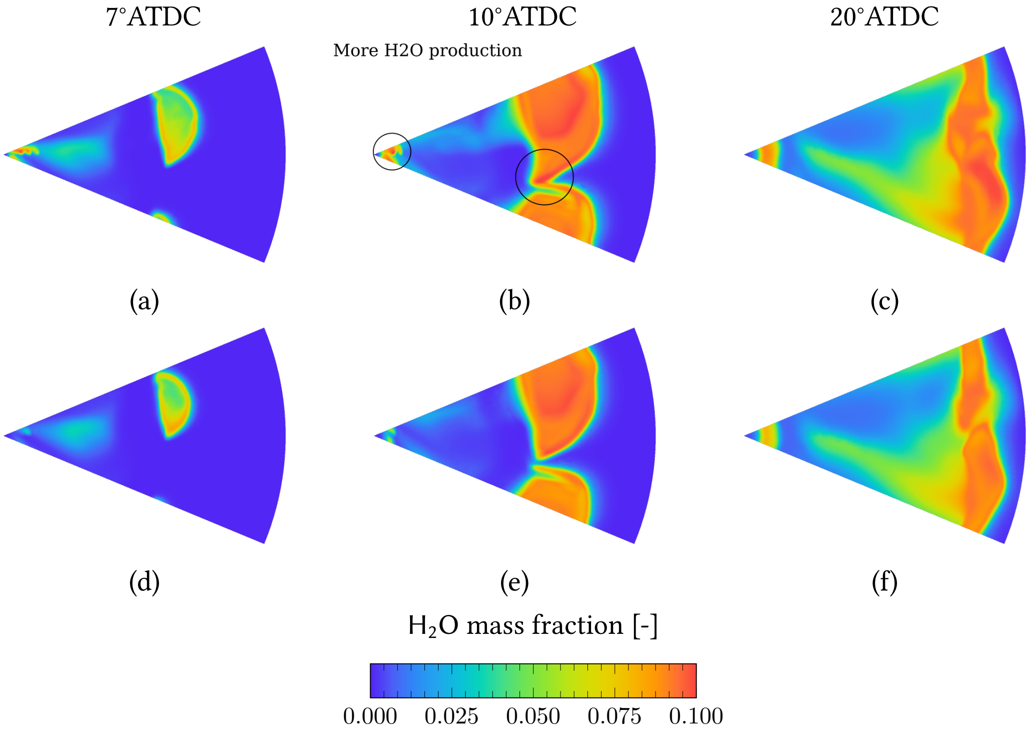

Figure 3.29: H_2O distribution for both NTP values with the re-entrant bowl at P1, 0% EGR: X-Y plane, -0.6 mm from head, NTP 2.25 mm (Upper), NTP 2.75 mm (Lower).

NTP difference has a smaller effect on burn duration at the higher load test point P2, however, increasing NTP still leads to a longer burn duration for the stepped-lip piston. In contrast, NTP 2.75 mm at P2 leads to a faster burn duration for the re-entrant bowl, especially at the 0% EGR test point. As seen earlier, an NTP of 2.75 mm directs the spray more into the bowl region. As such, at P2, where more fuel is injected and at a higher

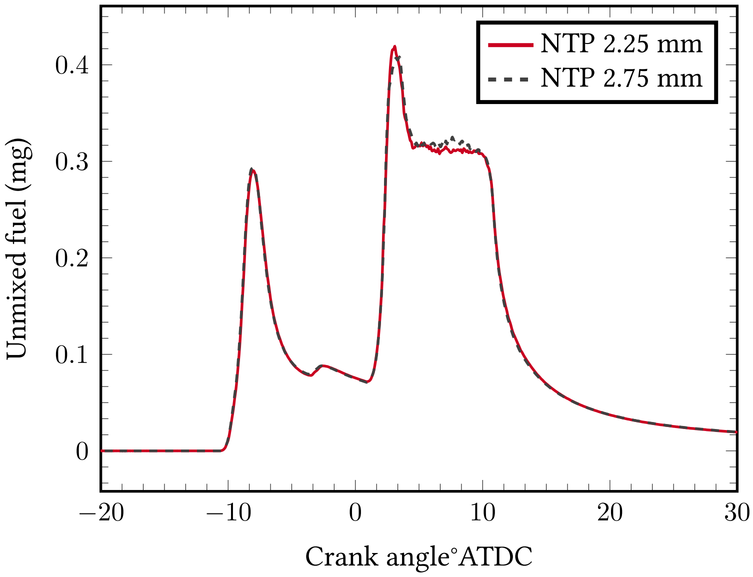

Figure 3.30: Total fuel quantity in unmixed zones for both NTP values with the re-entrant bowl at P1: 0% EGR

pressure, an NTP of 2.75 mm increases fuel-air mixing in the bowl region and promotes greater entrainment of this larger quantity of fuel than an NTP of 2.25 mm. Therefore, even though the burn rate is faster in the fire-land region with an NTP of 2.25 mm at P2 0% EGR (Figure 3.31), the burn rate in the bowl is much greater for an NTP of 2.75 mm as shown in Figure 3.32 and Figure 3.33 where it is clear from the H_2O distribution and temperature field, the flame area and intensity is higher.

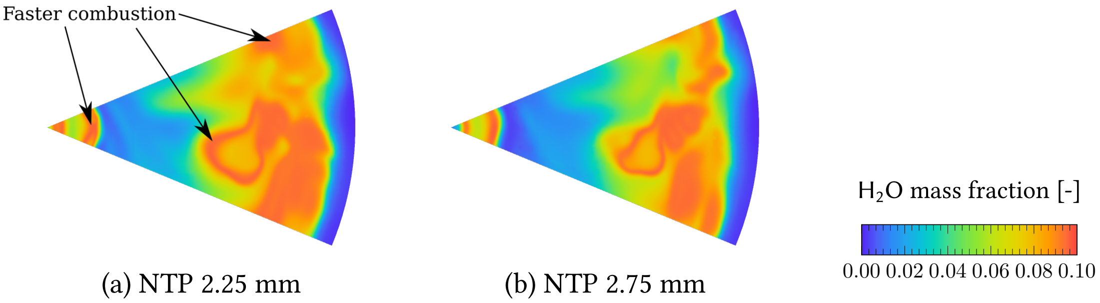

(a) NTP 2.25 mm

(b) NTP 2.75 mm

Figure 3.31: H_2O distribution for both NTP values with the re-entrant bowl at P2, 0% EGR: X-Y plane, -0.6 mm from head, 20°ATDC

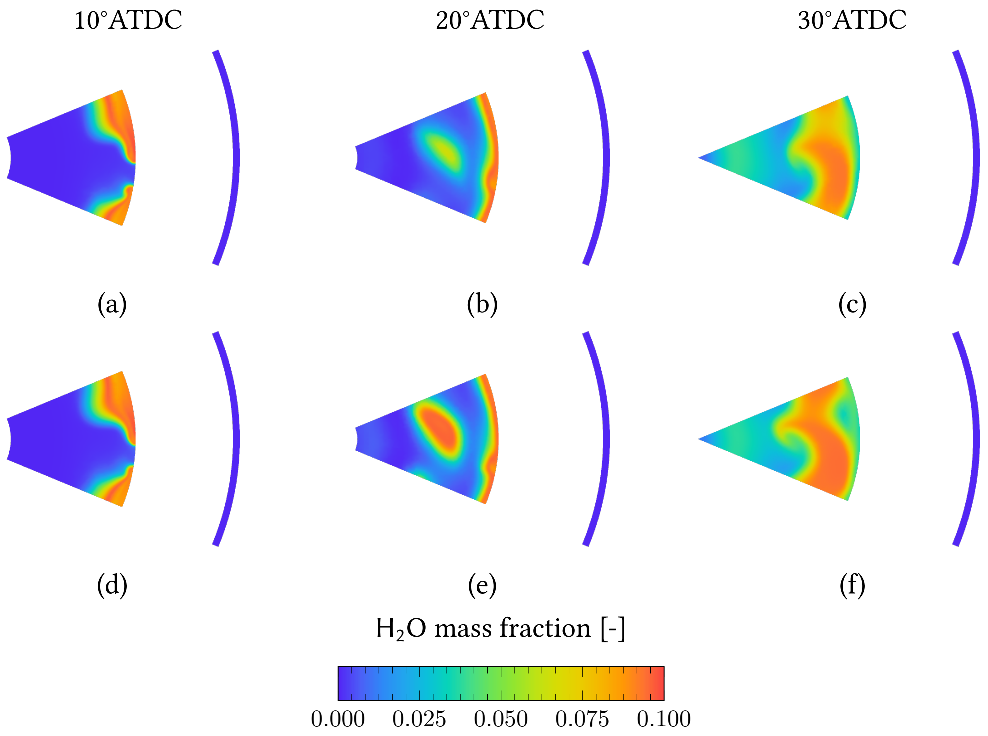

(a) (b) (c)

(d) (e) (f)

Figure 3.32: H_2O distribution for both NTP values with the re-entrant bowl at P2, 0% EGR: X-Y plane, -9 mm from head, NTP 2.25 mm (Upper), NTP 2.75 mm (Lower).

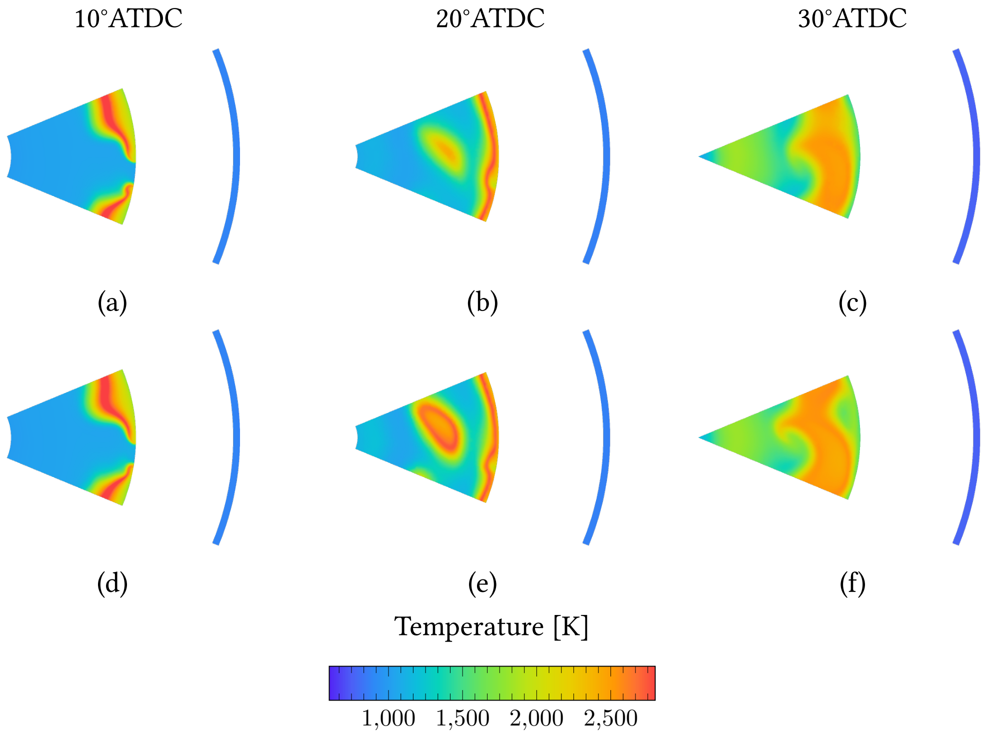

(a) (b) (c)

(d) (e) (f)

Figure 3.33: Temperature field for both NTP values with the re-entrant bowl at P2, 0% EGR: X-Y plane, -9 mm from head, NTP 2.25 mm (Upper), NTP 2.75 mm (Lower).

At both part load test points the stepped-lip piston has a longer combustion duration for both NTP values at all EGR rates. From comparing the cumulative heat release rates of both piston geometries in Figure 3.34, it can be seen that the burn rate reduces for the stepped-lip piston after end of injection (10.6°ATDC). As described earlier, the stepped-lip piston is akin to a forward facing step inhibiting fuel jet penetration into the fire-land and forming a low velocity zone near the lip edge. This limits flame propagation into the fire-land region resulting in a reduction of burn rate locally. Longer burn duration shown for the stepped-lip piston is in contrast to literature, where results presented show a reduction in burn duration with stepped-lip pistons compared to re-entrant pistons for similar load points [73, 74].

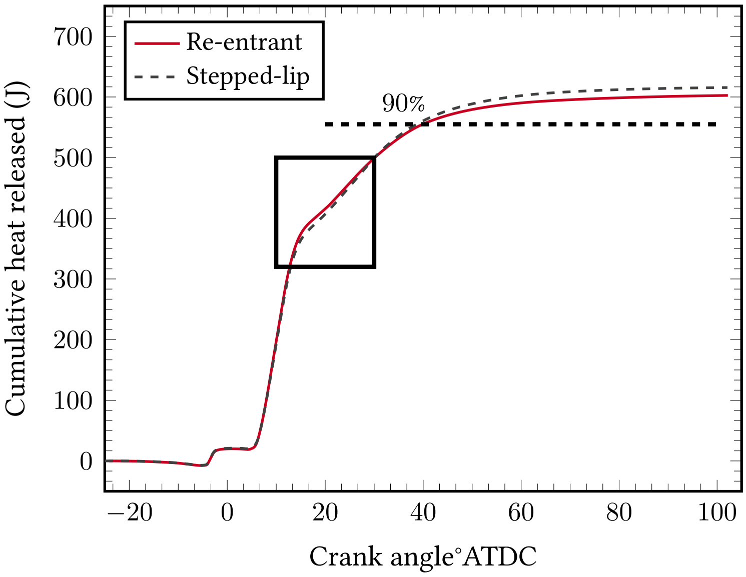

Figure 3.34: Cumulative heat release for both piston geometries with NTP 2.25 mm at P1, 0% EGR.

When comparing this study to those in literature, similar flow field behaviour is found for the stepped-lip piston where squish velocities are lower (Figure 3.35) and momentum distribution is away from the lip edge (Figure 3.36) when compared to the re-entrant design. The main difference arises from the lip geometry: where in this investigation it resembles an actual step, whilst in the aforementioned studies, the lip(s) resemble an inclined ramp from bowl to fire-land. As such, the effect of the lip in this investigation is far more constraining as it physically suppresses flame propagation into the fire-land as shown by the temperature field in Figure 3.37.

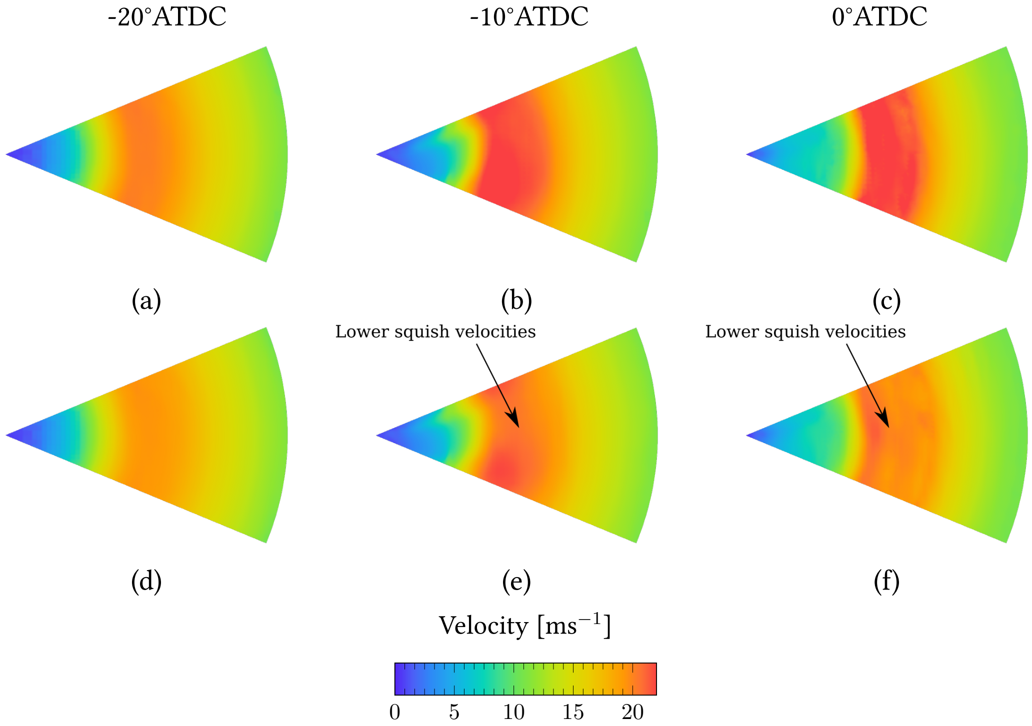

Figure 3.35: Velocity field in fire-land for both piston bowls with NTP 2.25 mm at P2, 0% EGR: X-Y plane, -0.5 mm from head, Re-entrant (Upper), Stepped-lip (Lower).

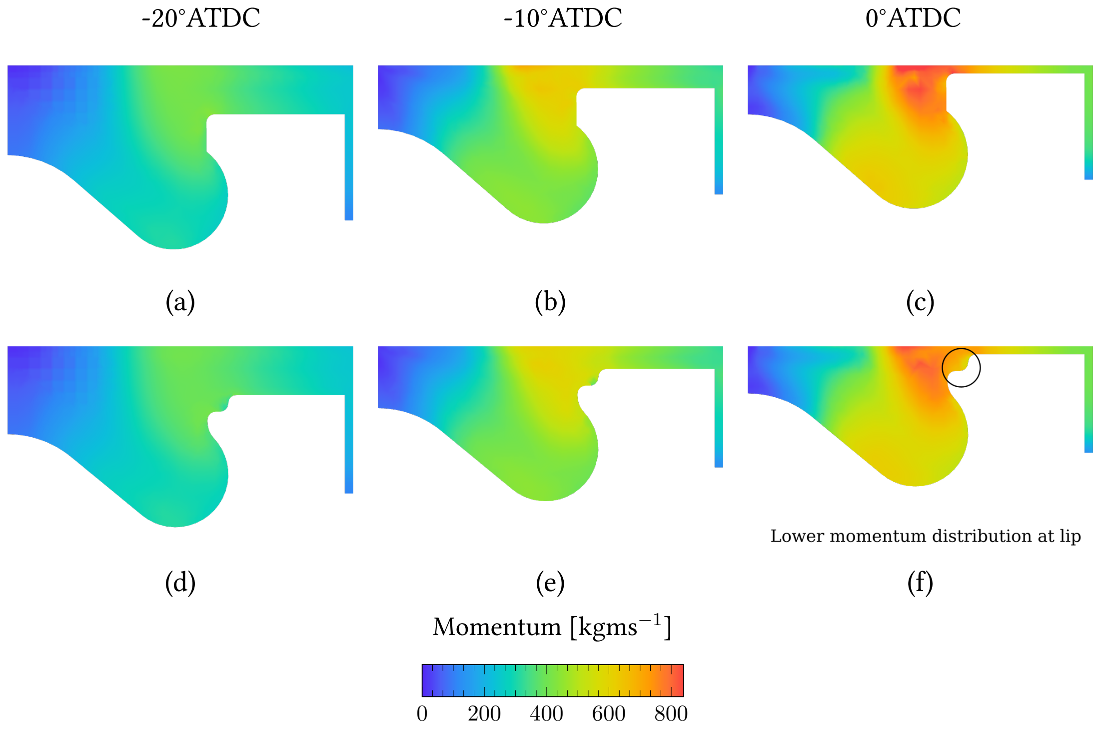

Figure 3.36: Momentum distribution for both piston bowls with NTP 2.25 mm at P2, 0% EGR: X-Y plane, -0.5 mm from head, Re-entrant (Upper), Stepped-lip (Lower).

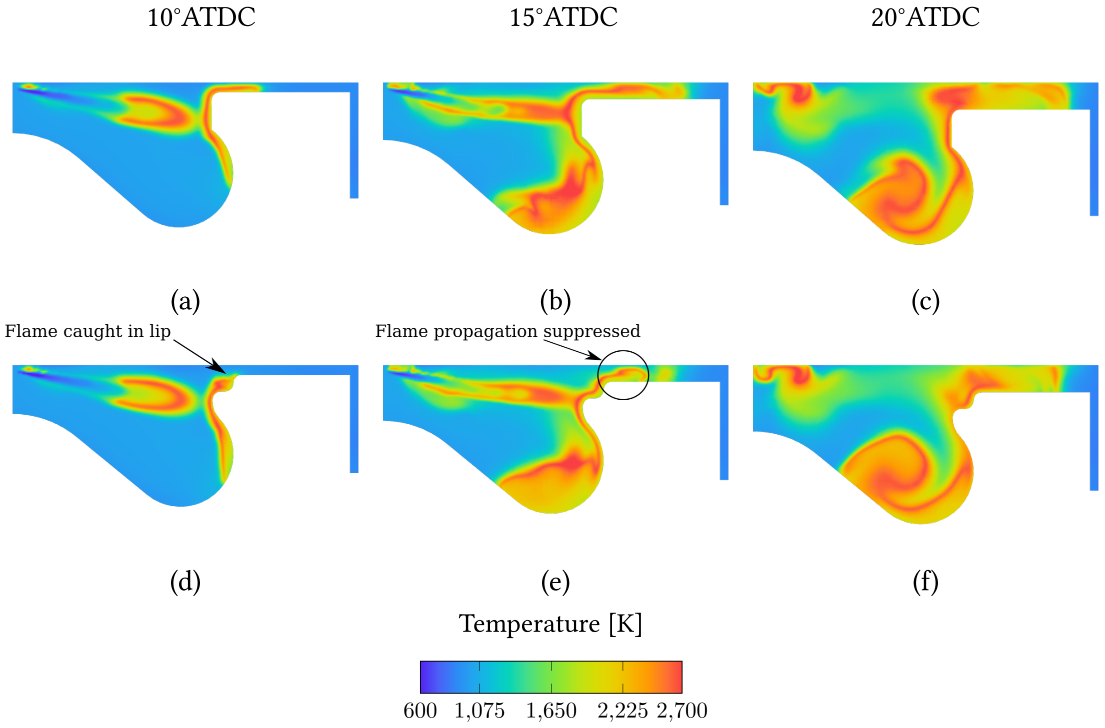

Figure 3.37: Temperature field for both piston bowls with NTP 2.25 mm at P2, 0% EGR: X-Y plane, -0.5 mm from head, Re-entrant (Upper), Stepped-lip (Lower).

3.6.2 Full load

In the interest of succinctness, only a limited set of full load results that highlight significant differences of the effects of NTP and piston geometry at the full load conditions will be presented here. Figure 3.38 and Figure 3.39 compare the soot and NO_x emissions between simulation and experiment for both NTP values. For a fixed engine speed, a good agreement between experiment and simulation is seen with NTP trends correctly predicted for both NO_x and soot emissions. However, when comparing across engine speeds, only NO_x emissions trends are captured correctly in simulations. The reduction in measured soot emissions at 4000 rpm has been attributed to post flame oxidation of soot during the exhaust stroke as a result of high exhaust temperatures (above 810℃) [6]. As the simulation is limited to only the closed part of the engine cycle, it is expected that soot mass at 4000 rpm will be over-predicted.

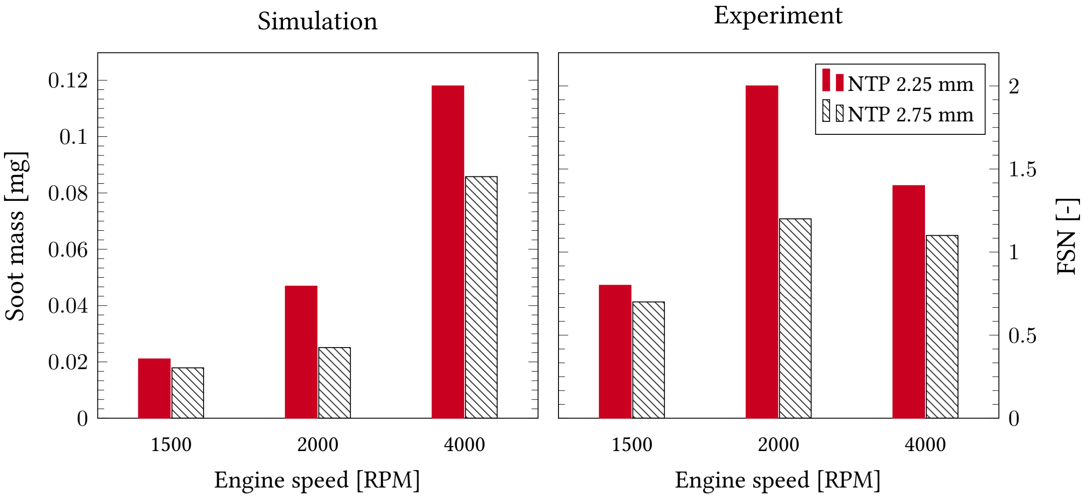

Figure 3.38: Simulated and measured soot emissions at full load for both NTP values with the re-entrant piston bowl.

Generally, the soot trends seen at part load are also observed at the full load conditions, where increasing NTP leads to lower soot emissions. The primary reason for this being spray targetting with an NTP of 2.75 mm leading to better air utilisation in the bowl region as well as reduced spray impingement on the piston walls. This is seen in Figure 3.40 where there is a greater equivalence ratio distribution in the bowl

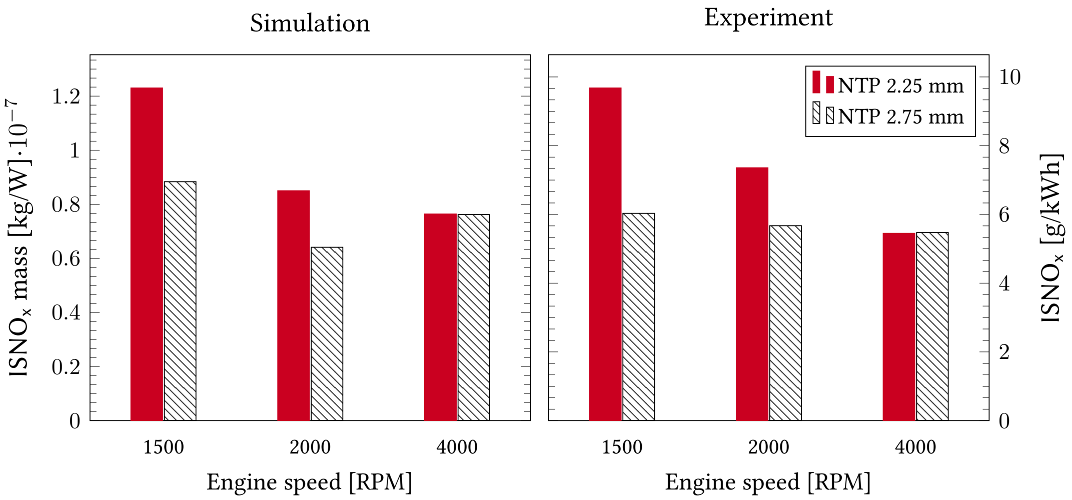

Figure 3.39: Simulated and measured NO_x emissions at full load for both NTP values with the re-entrant piston bowl.

region and less high concentration areas of fuel with an NTP of 2.75 mm. Similar to the part load points, it is clear from Figure 3.41 that there is more spray impingement on the piston walls with NTP 2.25 mm, leading to areas of high soot formation. This can also be observed in Figure 3.42 which shows the cumulative soot mass, formation and oxidation quantities for both NTP values at the 4000 rpm full load test point.

NTP 2.75 mm results in a reduction in NO_x for 1500, 2000 rpm and very little change at 4000 rpm. The reduction in NO_x is thought to be the effect of reduced combustion in the fire-land and increased mixing in the bowl region with NTP 2.75 mm. Combustion progression in the fire-land is much faster for NTP 2.25 mm as seen by the production of H_2O in Figure 3.43. This in turn leads to high temperatures, and as there is an availability of both oxygen and nitrogen, high NO_x is produced in this area as shown in Figure 3.44.

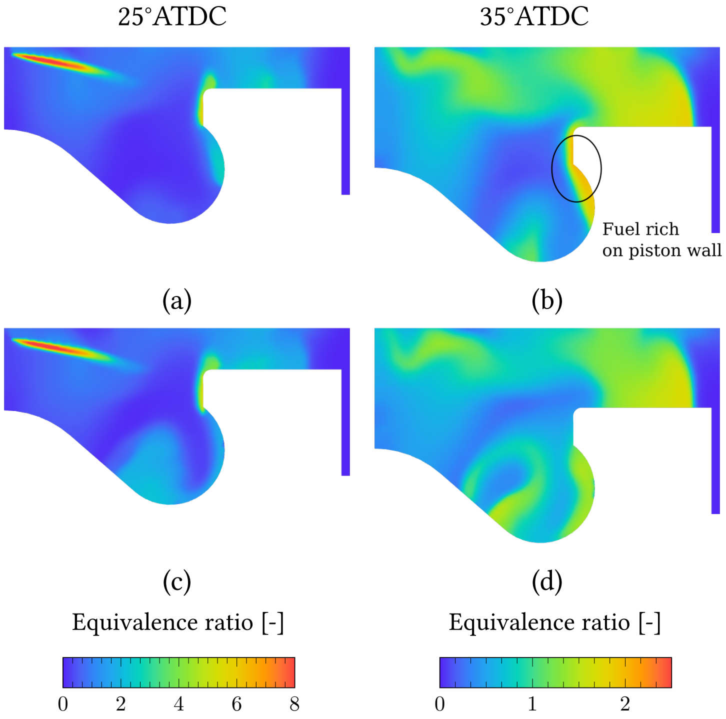

Figure 3.40: Equivalence ratio distribution for both NTP values with re-entrant bowl at 4000 rpm: NTP 2.25 mm (Upper), NTP 2.75 mm (Lower), X-Z plane.

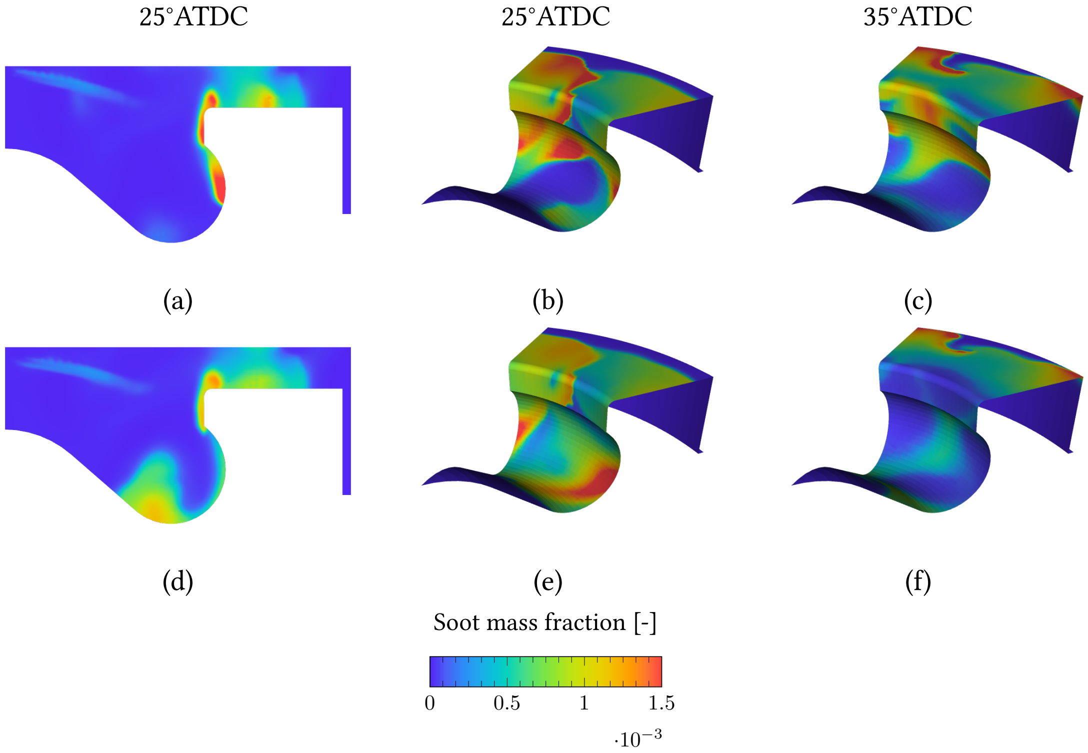

Figure 3.41: Soot mass fraction for both NTP value with re-entrant bowl at 4000 rpm: NTP 2.25 mm (Upper), NTP 2.75 mm (Lower), X-Z plane.

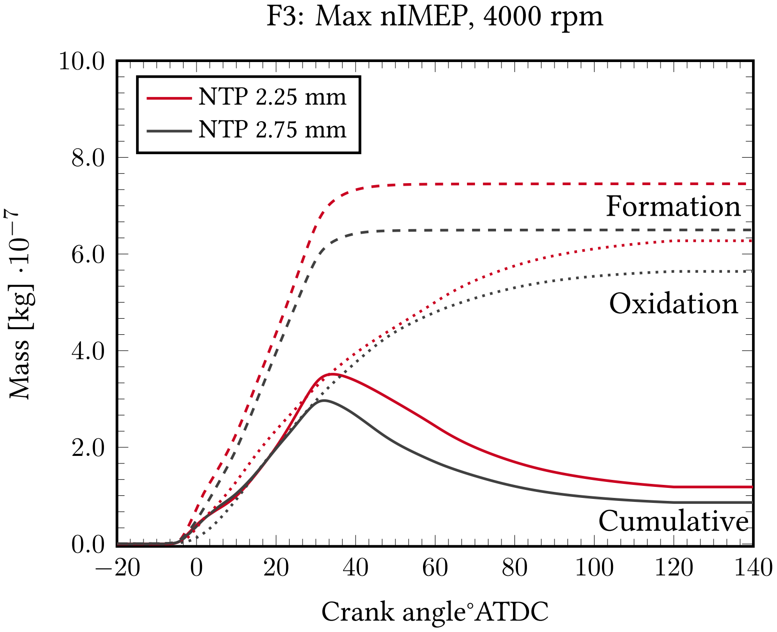

Figure 3.42: Soot formation, oxidation and cumulative soot mass for both NTP values with the re-entrant bowl at 4000 rpm.

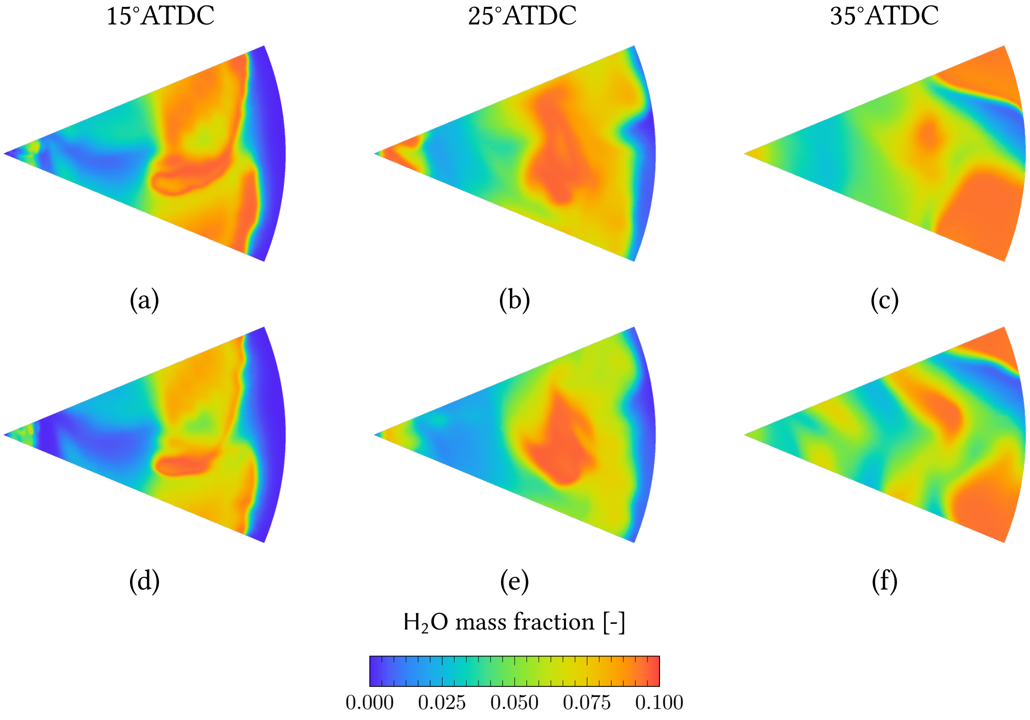

Figure 3.43: H_2O mass fraction for both NTP values with re-entrant bowl at 1500 rpm: X-Y plane, -1 mm from head, NTP 2.25 mm (Upper), NTP 2.75 mm (Lower).

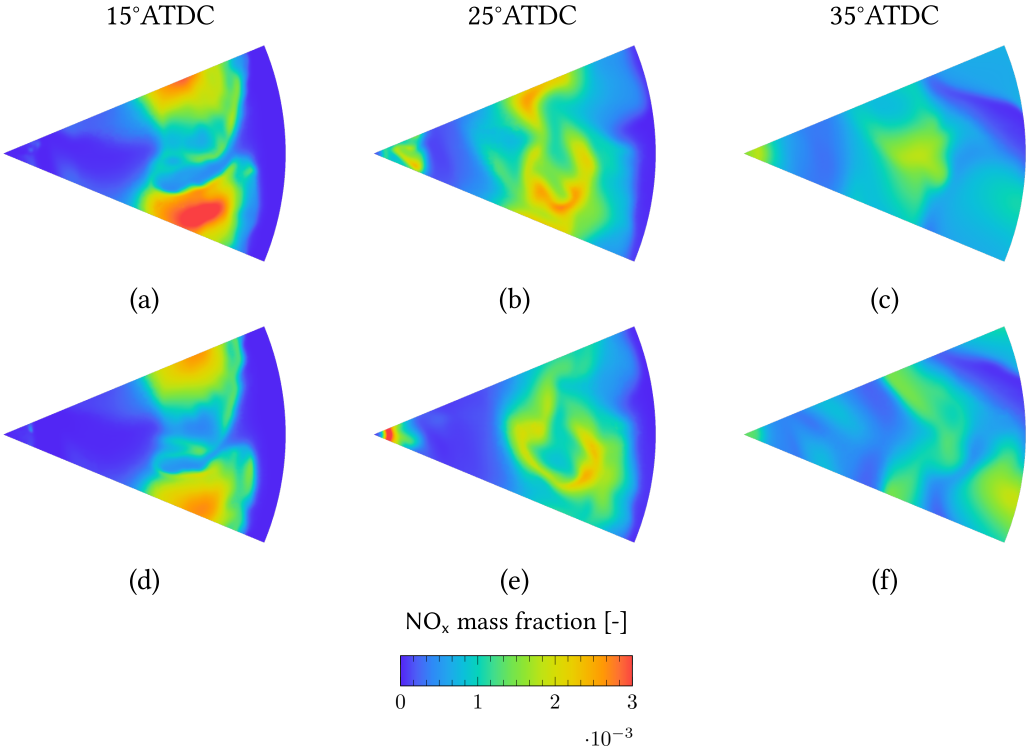

Figure 3.44: NO$_x$ mass fraction for both NTP values with re-entrant bowl at 1500 rpm: X-Y plane, -1 mm from head, NTP 2.25 mm (Upper), NTP 2.75 mm (Lower).

Similar to the part load test points, the stepped-lip piston results in an noticeable increase in NO$_x$ emissions, especially at 2000 and 4000 rpm as shown in Figure 3.45. Simulation results are consistent with experimental observations, however, the relative differences in NO$_x$ emissions between piston bowls are lower for 2000 and 4000 rpm simulation results.

As with the part load test points, the stepped-lip can be seen to suppress fuel penetration into the fire-land (Figure 3.46), leading to an accumulation of fuel vapour in the lip region. The low velocity zones formed (Figure 3.47) in this area coupled with high in-cylinder temperatures (Figure 3.48) leads to an increase in NO$_x$ in these areas (Figure 3.49). Furthermore, later into the cycle, the fuel vapour that was impeded by the piston lip and is now occupying the region near the cylinder head burns leaner - resulting in high combustion temperatures and increased NO$_x$ formation.

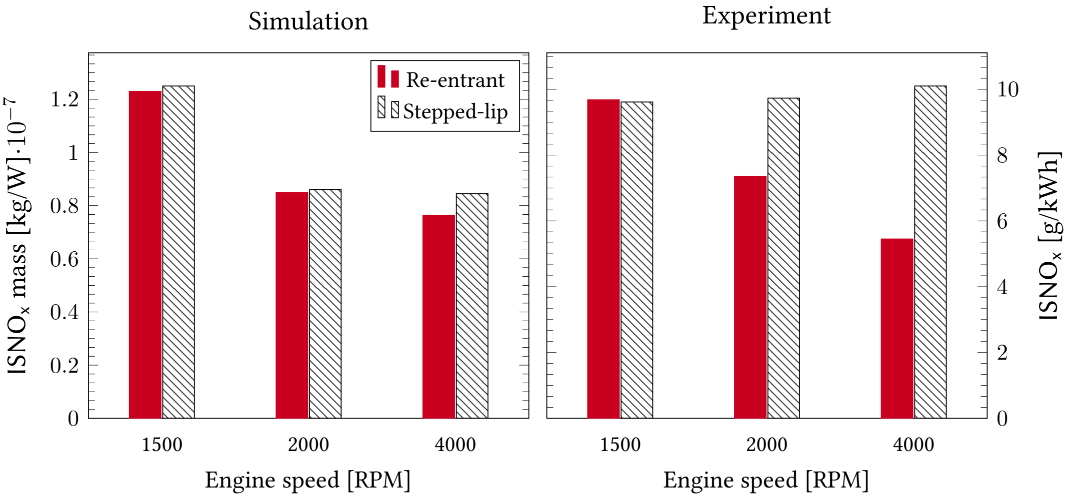

Figure 3.45: Simulated and measured NO$_x$ emissions at full load for both piston bowls with NTP 2.25 mm.

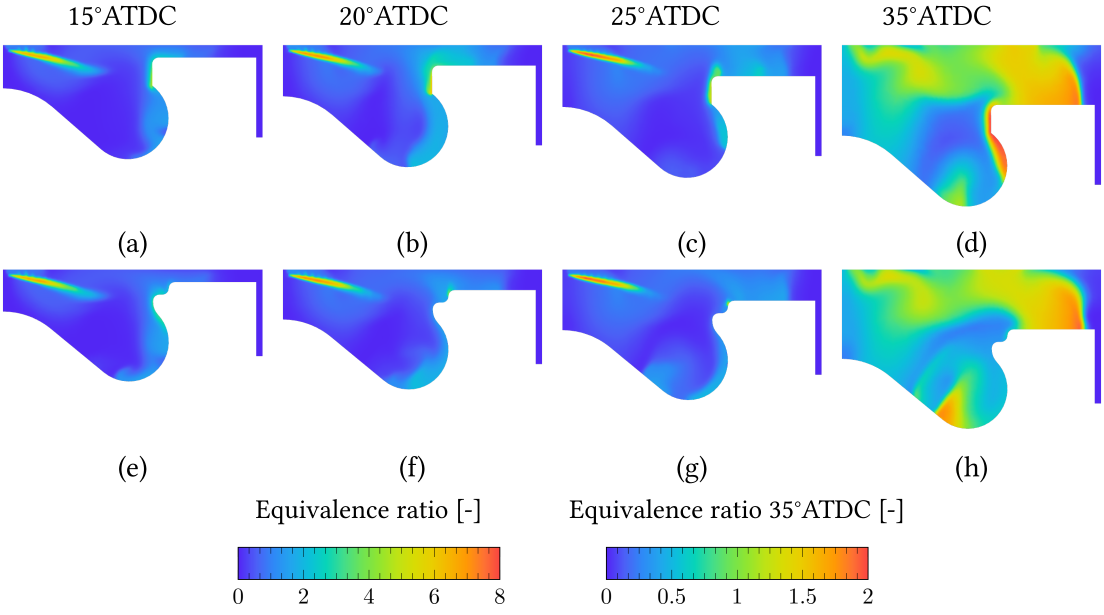

Figure 3.46: Equivalence ratio distribution for both piston bowls with NTP 2.25 mm at 4000 rpm: X-Y plane, Re-entrant (Upper), Stepped-lip (Lower).

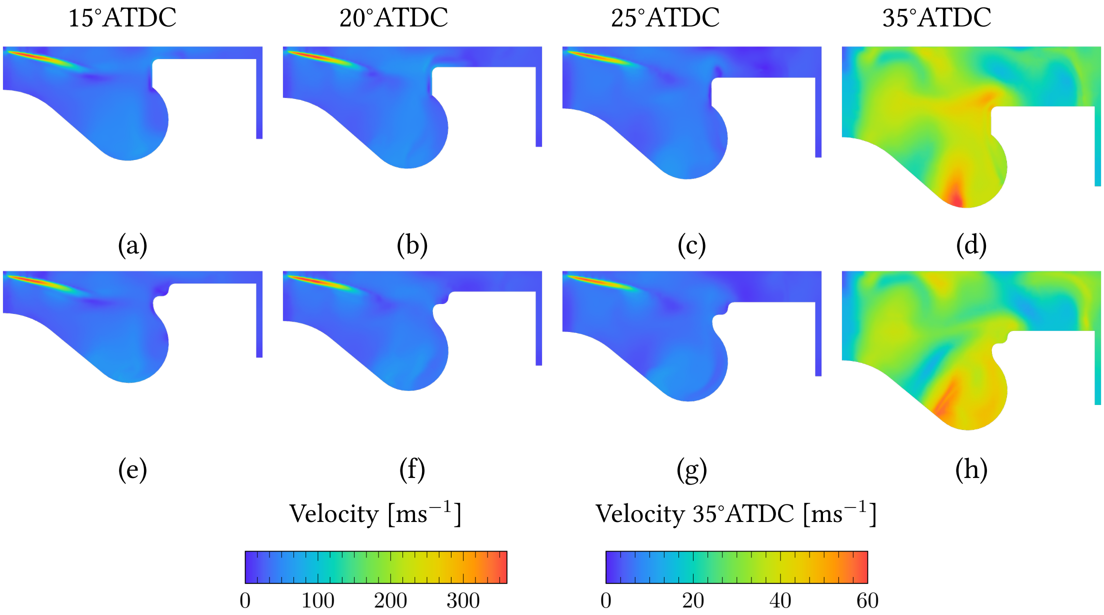

Figure 3.47: Velocity field for both piston bowls with NTP 2.25 mm at 4000 rpm: X-Y plane, Re-entrant (Upper), Stepped-lip (Lower).

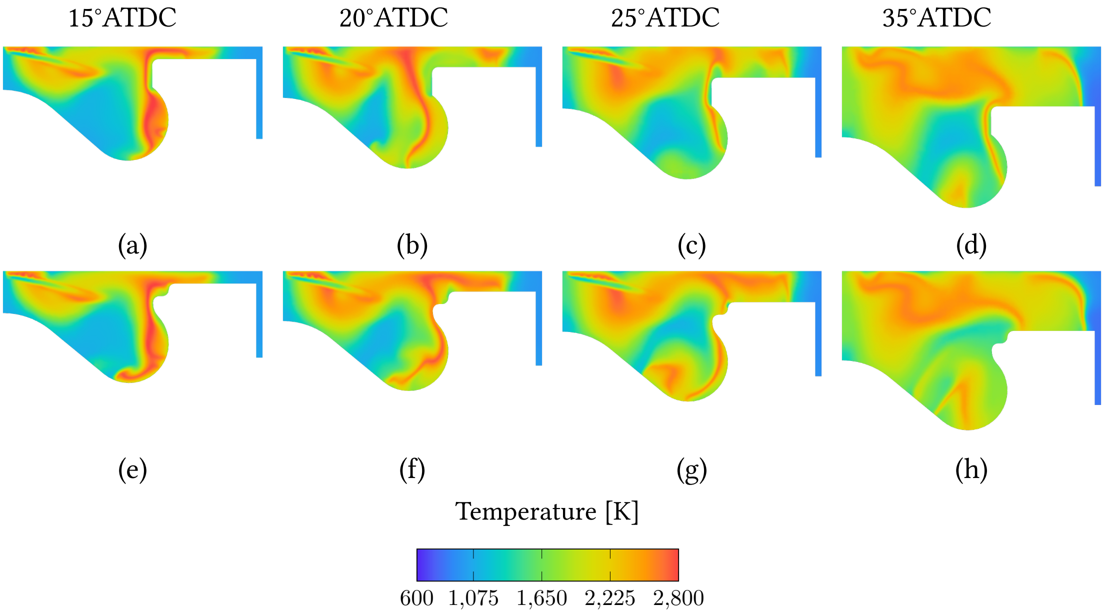

Figure 3.48: Temperature distribution for both piston bowls with NTP 2.25 mm at 4000 rpm: X-Y plane, Re-entrant (Upper), Stepped-lip (Lower).

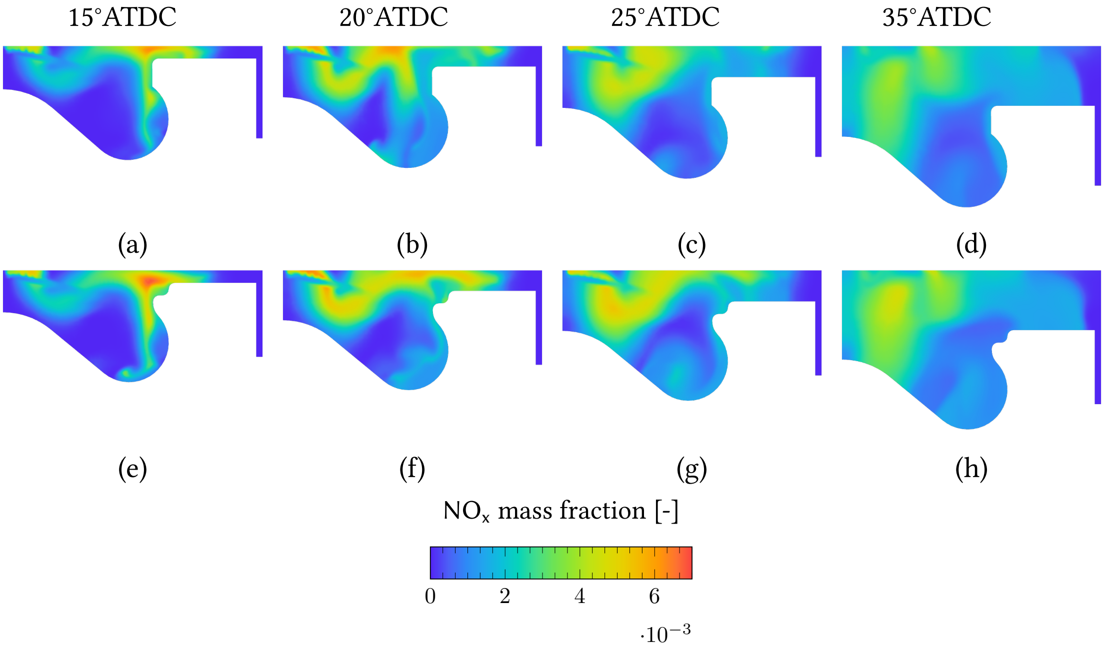

Figure 3.49: NO$_x$ distribution for both piston bowls with NTP 2.25 mm at 4000 rpm: X-Y plane, Re-entrant (Upper), Stepped-lip (Lower).

3.7 Summary

The results shown demonstrate the sensitivity of the combustion event to even the smallest of changes in spray targetting and piston bowl geometry. The CFD model predictions agreed with experimental measurements across load points and EGR rates. However, the relative differences between piston geometry and NTP values were less pronounced in the simulation results compared to the experiment.

In general, the effect of NTP on emissions and combustion progression was greater than the effect of piston geometry. It was found that increasing NTP led to soot reduction across load points and EGR rates for both piston bowls with a marginal increase in NO_x emissions. A deeper NTP was found to increase air utilisation resulting in less fuel-rich areas which promote soot formation. However, the deeper NTP led to an increase in burn duration at all load points for both piston geometries due to limited fuel availability in the fire-land region early in the cycle. Although, this effect was noticeably less pronounced at higher loads.

For the same NTP value, the stepped-lip piston was found to generally reduce soot formation at a marginal expense of increased NO_x emissions. The stepped-lip acted as a forward facing step leading to a re-circulation region in the vicinity of the lip. This resulted in increased residence time of nitrogen at higher temperatures which promoted NO_x formation. Furthermore, the stepped-lip piston led to an increase in burn duration for all load points at both NTPs and across EGR rates when compared to the re-entrant bowl. This result is in direct contrast with existing literature where the effect of the stepped piston bowl was to reduce burn duration when compared to the re-entrant bowl. This difference was attributed to the characteristics of the piston geometry, where in this investigation the piston lip resembles a 'true' step, with an almost right angled change in height, as opposed to the more ramped shaped lip of the relevant investigations in literature. This 'true' step geometry was found to limit fuel penetration into the fire-land region and suppress flame propagation - leading to an increase in burn duration.

From the results presented here, it can be concluded that the ECFM-3Z model is able to successfully capture global combustion parameters such as in-cylinder pressure and heat release rate over a range of operating points. However, the model has difficulty in predicting pollutant formation to comparable degrees as seen in the experiment. This is mainly attributed to the simplified combustion chemistry used in the ECFM-3Z model as it limits the emissions models that can be coupled to it. Additionally, the description of sub-grid mixing is modelled as function of turbulent time-scale in the ECFM-3Z model which effectively assumes that only one turbulent scale influences the flame. Furthermore, the reaction source terms in the ECFM-3Z model are based on Arrenhius type functions - which use the mean temperature to compute the chemical time-scale. As described earlier in Section 2.5.1, this approach can lead to large errors. Moiz [105] compared the well mixed, RIF, ECFM-3Z and shell-CTC combustion models in predicting low temperature split injections in a constant volume combustion chamber. It was found that no model was able to capture all the evaluated combustion criteria to a high degree of accuracy when compared to experimental measurements. For example, the ECFM-3Z model was able to successfully predict ignition delay and flame lift-off length but failed in predicting flame reactivity (ratio of flame length to inert spray length). In contrast, the RIF model was able predict flame reactivity very close to the experimental measurements, indicating the combustion chemistry was described accurately. However, the RIF model is computationally much more expensive to run than the ECFM-3Z model, especially when the number of flamelets are increased. The results presented in this chapter as well as the work by Moiz [105] highlight the need for a combustion model that includes detailed chemistry, provides a comprehensive description of TCI and is computationally efficient. Developing a model to fulfil these criteria is the second objective of this thesis and will be presented in the next chapter.

Chapter 4

Conditional source-term estimation

The content in this chapter is a result of the collaborative efforts of the author and his colleague XiaoHang Fang. The author was responsible for chemistry reduction and tabulation using flamelet generated manifolds. XiaoHang Fang was responsible for the implementation of the main conditional source-term estimation combustion routine and its interfacing to the CFD code. Additionally, the author assisted XiaoHang Fang with debugging throughout various stages of the implementation. The content in this chapter has been published in [8, 9].

4.1 Formulation

As described earlier in Section 2.5.1, the mean chemical source term cannot be recovered from the mean scalar field due to its highly non-linear nature.

$$\overline{\dot{\omega}}_k \neq \dot{\omega}_k \left(\overline{T}, \overline{Y}_k, \overline{\rho}\right) \tag{4.1}$$

CSE proposed by Bushe and Steiner [51] invokes the same 1^{st} order CMC hypothesis in evaluating the chemical source term, whereby conditionally averaged scalars are used to determine the conditionally averaged chemical source term - which is then used to recover the mean chemical source term. Using conditional averages suppresses fluctuations of the scalar field leading to a better approximation of the mean chemical source term [47].

$$\langle \dot{\omega}_k | \eta \rangle \approx \dot{\omega}_k \left(\langle T | \eta \rangle, \langle Y_k | \eta \rangle, \langle \rho | \eta \rangle \right) \tag{4.2}$$

where $\langle\dot{\omega}_k|\eta\rangle$ is the conditionally averaged chemical source term for species k conditioned on the mixture fraction, $\langle T|\eta\rangle$ is the conditional temperature, $\langle Y_k|\eta\rangle$ is the conditional species mass fraction and $\langle\rho|\eta\rangle$ is the conditional density. In non-premixed combustion, the mixture fraction is commonly selected as the conditioning variable as it is a conserved quantity and thermochemical quantities are strongly correlated to it [11, 48, 50]. Once the conditional scalars are known, the conditional chemical source term for each species is retrieved as Equation 4.2 through a chemistry model. Finally, the mean chemical source term is computed through integrating the conditional chemical source term with a presumed PDF of the mixture fraction as:

$$\bar{\dot{\omega}}_k(\vec{x},t) = \int_0^1 \langle\dot{\omega}_k|\eta\rangle\left(\eta,\vec{x},t\right)\overline{P}\left(\eta,\vec{x},t\right)d\eta \tag{4.3}$$

Unlike CMC, where transport equations are solved for the conditionally averaged scalars, CSE approximates the conditionally averaged scalars through inversion of the following integral knowing the unconditional Favre averaged scalars and presuming a PDF for the mixture fraction:

$$\widetilde{f}\left(\vec{x},t\right) = \int_0^1 \langle f_k|\eta\rangle\left(\eta,\vec{x},t\right)\widetilde{P}\left(\eta,\vec{x},t\right)d\eta \tag{4.4}$$

where $\widetilde{f}$ is the unconditional Favre averaged scalar as computed from the Favre averaged scalar equation, $\langle f_k|\eta\rangle$ is the conditionally averaged scalar conditional on the mixture fraction and $\widetilde{P}$ is the density weighted presumed β-PDF of the mixture fraction (Equation 2.70). Additionally, as conditionally averaged scalars vary much less in space than unconditionally averaged scalars [50], CSE assumes spatial homogeneity for the conditional averages for defined ensembles of points. Equation 4.4 can now be written as:

$$\widetilde{f}\left(\vec{x}_j,t\right) = \int_0^1 \langle f_k|\eta\rangle\left(\eta,t\right)\widetilde{P}\left(\eta,\vec{x}_j,t\right)d\eta \qquad j\in E \tag{4.5}$$

where $\vec{x}_j$ is the spatial coordinate of the j^{th} point in the ensemble E. Equation 4.5 is a Fredholm equation of the first kind with $\widetilde{P}\left(\eta,\vec{x},t\right)$ as the kernel. Recovering the conditional scalars from this integral begins with discretizing Equation 4.5 using m bins for mixture fraction:

$$\vec{b} \;=\; \mathbf{A}\vec{\alpha} \tag{4.6}$$

$$\mathbf{A} \;=\; A_{j,i} = \int_{\eta_1}^{\eta_2} \widetilde{P}\left(\eta, \vec{x}_j, t\right) d\eta \tag{4.7}$$

where $\vec{b}$ is the vector containing $\widetilde{f}\left(\vec{x}_j, t\right)$, $\vec{\alpha}$ is vector containing $\langle f_k|\eta\rangle\left(\eta, t\right)$ and $A_{j,i}$ is the integrated PDF in the i^{th} bin over mixture fracture interval η_1 to η_2. The solution to Equation 4.6 is:

$$\vec{\alpha} = \mathbf{A}^{-1}\vec{b} \tag{4.8}$$

This inverse problem is susceptible to ill-posedness due to the solution being sensitive to small perturbations in the system (Type III ill-posed according to Hadamard [106]). Consequently, regularization needs to be employed to achieve a smooth, stable and unique solution. Commonly used regularization methods in CSE are Truncated Singular Value Decomposition (TSVD) [107] and Tikhonov regularization [108]. Zeroth order Tikhonov regularization is used in the present study as it has been successful in many earlier CSE investigations [109, 110, 111, 112, 113, 114]. Zeroth order Tikhonov regularization leads to the solution of the following least-squares problem:

$$\vec{\alpha} = \arg\min \left\| \begin{bmatrix} \mathbf{A} \\ \lambda \mathbf{I} \end{bmatrix} \vec{\alpha} - \begin{bmatrix} \vec{b} \\ \lambda \vec{\alpha}^0 \end{bmatrix} \right\|_2^2 \tag{4.9}$$

where λ is the regularization parameter, $\mathbf{I}$ is the Identity matrix, $\vec{\alpha}^0$ is some *a-priori* knowledge of the solution and $\|\cdot\|_2^2$ is the L2-norm of the vector. The *a-priori* solution is taken as the solution of the previous time-step as per the method of Grout *et al.* [114] with the optimum regularization parameter computed using the L-curve method of Hansen [115]. Further details on inversion and regularization can be found in the thesis of Salehi [116].

4.2 Chemistry Reduction

Combustion of hydrocarbon fuels involves thousands of species and tens of thousands of reactions. Therefore, simulations of multi-dimensional combustion with detailed kinetics is unfeasible due to the prohibitive computational expense and numerical difficulties that arise from stiffness in the representative ODEs due to the large range of chemical time-scales. Conventional reduction techniques rely on time-scale analysis where fast and slow processes are decoupled through quasi steady state (QSSA) [117, 118] or partial equilibrium assumptions (PEA) [119, 120]. This enables certain species/reactions to be omitted leading to what is known as a reduced mechanism. However, using these methods requires detailed knowledge of the chemical kinetics and the resulting mechanisms are only valid for a limited range of conditions.

A more general approach to chemistry reduction is the Intrinsic Low Dimensional Manifold (ILDM) method of Maas & Pope [121], where combustion is considered as movement along a trajectory in composition space. Starting from different initial conditions a chemical system will reach the same equilibrium state after a long enough time. This equilibrium state is determined by conserved quantities of absolute enthalpy, pressure and element mass fraction with combustion progression determined from the evolution of species mass fractions. The main idea in ILDM is that after a short period of time, the entire chemical system can be described by a reduced set of control variables in composition space (a low dimensional manifold). Thermochemical quantities such as temperature and species mass fractions are tabulated and parametrised as a function of these control variables and looked-up via multi-linear interpolation during combustion simulations. The ILDM method is computationally efficient and provides good results for high temperature chemistry close to equilibrium, however, low temperature chemistry is not well accounted for in the ILDM method due to the dimension of the manifold increasing substantially in this region to be able to account for the similar time-scales of flow and chemistry - leading to this region usually being determined from linear interpolations [11, 122]. Numerical challenges with the ILDM approach present additional difficulties in attaining converged solutions and so an alternative approach - Trajectory Generated Low Dimensional Manifold (TGLDM) was proposed by Pope & Maas [123]. The TGLDM is based on the same principles as ILDM but instead of generating a manifold from the chemical system, TGLDM computes the manifold along reaction trajectories - which is a path the chemical system takes through composition space from its initial state to the chemical equilibrium state. Huang & Bushe [124] and Lee *et al.* [125] successfully built TGLDM databases using auto-ignition trajectories to simulate non-premixed methane and methanol flames with CSE respectively. Additionally, Salehi *et al.* [112], Dovizio *et al.* [110] and Shahbazian *et al.* [126] successfully used unstrained one-dimensional premixed flames to generate TGLDM databases to simulate premixed methane flames with CSE. As can be seen from these studies CSE-TGLDM has performed very well in simulating combustion with methane and lighter fuels, however, when the CSE-TGLDM (auto-ignition trajectories) method was applied to an n-heptane spray flame, the manifold was unable to converge with species composition progressing towards points on the edge or even outside the realizable region of the manifold [127]. This phenomenon was attributed to the complexity of n-heptane fuel and the high number of degrees of freedom in the reaction mechanism. To overcome the limitations of ILDM, the Flame Prolongation of ILDM (FPI) method of Gicquel *et al.* [128] and the Flamelet Generated Manifold (FGM) methodology of van Oijen *et al.* [30, 31] independently extended the ILDM approach through computing the manifold from simulations of one-dimensional premixed laminar flames using detailed chemistry. Using flamelet solutions to compute the low dimensional manifold allows transport effects to be considered and depending on the flame of interest, different types of flamelets can be used - leading to an effective and flexible approach to chemistry tabulation.

4.2.1 Flamelet Generated Manifold

In the present work, chemistry tabulation is based on the FGM approach where one-dimensional flamelet solutions are pre-computed using detailed chemistry and parametrised using a reduced number of control variables.

Canonical flame configuration

Depending on the combustion application, a flame configuration must be selected that adequately represents the chemical processes taking place in the flame of interest. Diesel combustion is predominantly non-premixed and is therefore best represented by the igniting counter-flow diffusion flame (ICDF). In this flame, oxidiser and fuel streams are opposed to each other forming a reaction zone perpendicular to the streams as illustrated in Figure 4.1.

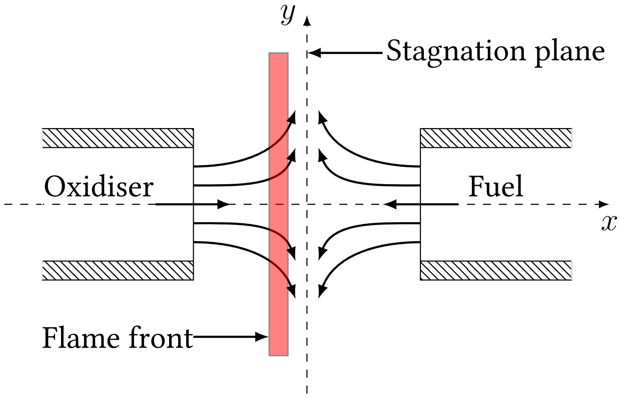

Figure 4.1: Schematic of a laminar counterflow diffusion flame.

Straining of the flame is achieved by either increasing the flow velocities or reducing the distance between the two streams. An unstrained flame will depart from chemical equilibrium with increasing strain up until it quenches.

Following Stahl & Warnatz [129] the one-dimensional governing equations for an ICDF are given as:

$$\frac{\partial \rho}{\partial t}+\frac{\partial \rho u}{\partial x} = -\rho K \tag{4.10}$$

$$\frac{\partial \rho h}{\partial t}+\frac{\partial \rho u h}{\partial x} = \frac{\partial}{\partial x}\left(\rho D\frac{\partial h}{\partial x}\right)-\rho K h \tag{4.11}$$

$$\frac{\partial \rho Y_i}{\partial t}+\frac{\partial \rho u Y_i}{\partial x} = \frac{\partial}{\partial x}\left(\rho D\frac{\partial Y_i}{\partial x}\right)+\dot{\omega}_i-\rho K Y_i \qquad i\in[1,N_s-1] \tag{4.12}$$

$$\frac{\partial \rho K}{\partial t}+\frac{\partial \rho u K}{\partial x} = \frac{\partial}{\partial x}\left(\mu\frac{\partial K}{\partial x}\right)+\rho_{ox}a^2-\rho K^2 \tag{4.13}$$

where D is the diffusion coefficient and is given as $D = \frac{\lambda}{\rho c_p}$ assuming unity Lewis number. λ is the heat conductivity and c_p is the specific heat. K is the stretch rate which accounts for the y-component of flow and its effect on the flame. K is a function of (x,t) and varies by the prescribed strain rate a at the oxidiser boundary:

$$K(x,t)=\frac{\partial u_y}{\partial y} \tag{4.14}$$

$$K(x\rightarrow-\infty)=a, \qquad K(x\rightarrow\infty)=a\sqrt{\frac{\rho(x\rightarrow-\infty)}{\rho(x\rightarrow\infty)}} \tag{4.15}$$

In this work the CHEM1D code of Einhoven University of Technology [130] is used to solve one-dimensional ICDF in physical space and time with detailed chemistry. Figure 4.2 illustrates temperature evolution as a function of spatial coordinate x and time for a laminar counter-flow diffusion flame at engine-like conditions. n-Dodecane fuel flows in from the right and oxidiser diluted with EGR flows in from the left at a strain rate of 500 s^{-1}. A purely mixing solution (frozen chemistry) at the test conditions (temperature, pressure, species mass fraction and strain rate) is used as initialisation to the ICDF as indicated by the green line. The ignition process is then tracked from this mixing solution in time (black lines) until a quasi steady state flame is reached (red line).

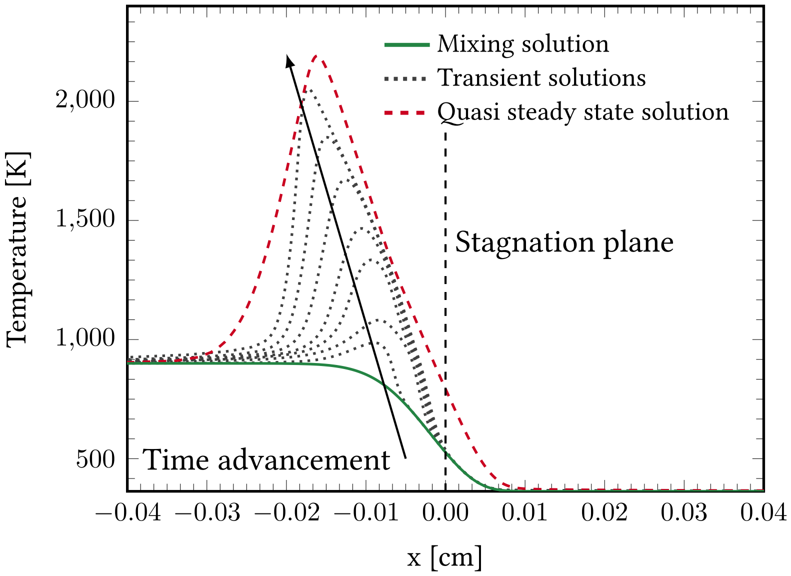

Figure 4.2: Temperature evolution in space, x and time, t for an igniting counter-flow diffusion flame with n-Dodecane: $a = 500$ s^{-1}, $T_{fu} = 363$ K, $T_{ox} = 900$ K, $P_{amb} = 60.0$ MPa, $O_2 = 15$ %.

FGM Parametrization

Full composition space of the flamelet solutions is described by $N_s + 2$-dimensional solutions spanned by enthalpy, pressure and N_s number of species. Through careful consideration, a reduced set (any number or combination) of controlling variables can be used to parametrize the flamelet solutions as long as the full mixture composition is described. Increasing the number of controlling variables will increase accuracy up to $N_s + 2$ dimensions, where eventually the full composition space will be recovered. As this work will focus on spray combustion applications: fuel-oxidiser mixing, ignition and combustion progression in the diffusion flame are the main physical phenomena of interest. Mixing can be described by the mixture fraction, Z as seen earlier in Section 2.5.3 using the definition of Bilger [40] in Equation 2.69. The mixture fraction is a monotonic function of spatial coordinate x which allows direct mapping of flamelet solutions from physical space to mixture fraction space as shown in Figure 4.3. Starting from the mixing solution up until chemical equilibrium, any variable that continuously increases or decreases with time can be used to describe ignition and combustion progression. In this work, the reaction progress variable $\mathcal{C}$, is defined as weighted linear combination of certain key species mass fractions that represent each stage of combustion evolution:

$$\mathcal{C} = \frac{Y_{\mathrm{CH_2O}}}{Y^{eq}_{\mathrm{CH_2O}}} + \frac{Y_{\mathrm{CO}}}{Y^{eq}_{\mathrm{CO}}} + \frac{Y_{\mathrm{CO_2}}}{Y^{eq}_{\mathrm{CO_2}}} \tag{4.16}$$

To capture ignition, formaldehyde ($\mathrm{CH_2O}$) is included as it is found in high concentrations at the onset of ignition [131, 132]. Major combustion products of CO and $\mathrm{CO_2}$ represent the intermediate and end phases of combustion. In order for each species in the reaction progress variable definition to have a balanced contribution, it is weighted by its equilibrium mass fraction.

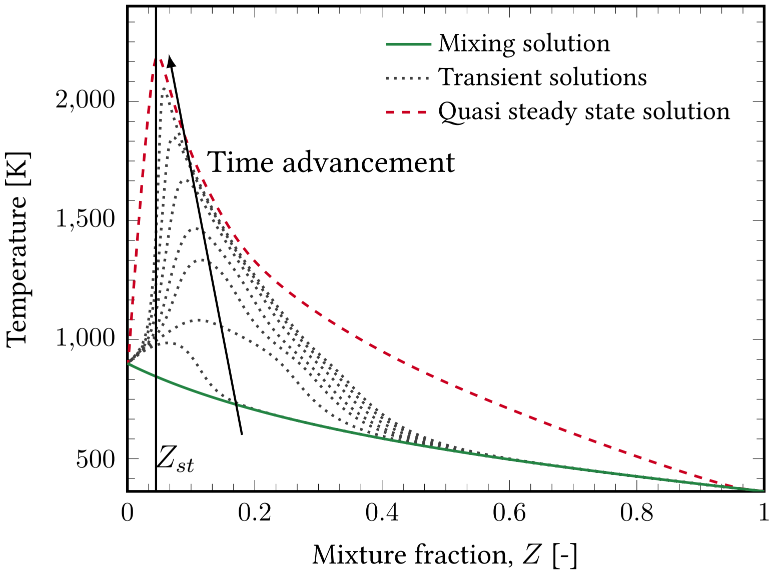

Figure 4.3: Temperature evolution in mixture fraction space for an igniting counter-flow diffusion flame with n-Dodecane: $a = 500$ s^{-1}, $T_{fu} = 363$ K, $T_{ox} = 900$ K, $P_{amb} = 6.0$ MPa, $\mathrm{O_2} = 15$ %.

To account for combustion in a steady flame, the FGM database generated by ICDFs is extended further by including solutions of steady flamelets at strain rates varying from the highest non-quenching strain rate down to $a = 1$ s^{-1}. This covers the entire Z-$\mathcal{C}$ space from the mixing line up to chemical equilibrium. A typical sub-space describing the FGM generation process is shown in Figure 4.4 and the resultant manifold is shown in Figure 4.5. All flamelet calculations are carried out assuming constant pressure and conserved enthalpy, therefore, if variations in any of these quantities occur, additional dimensions will be required in the FGM database in order to account for the influence of these variables on combustion.

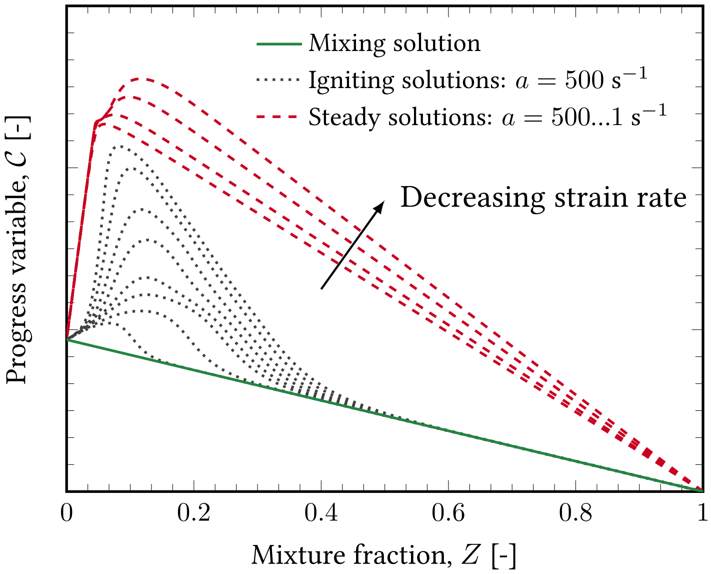

Figure 4.4: Schematic representation of progress variable as a function of mixture fraction for a series of counter-flow diffusion flamelets.

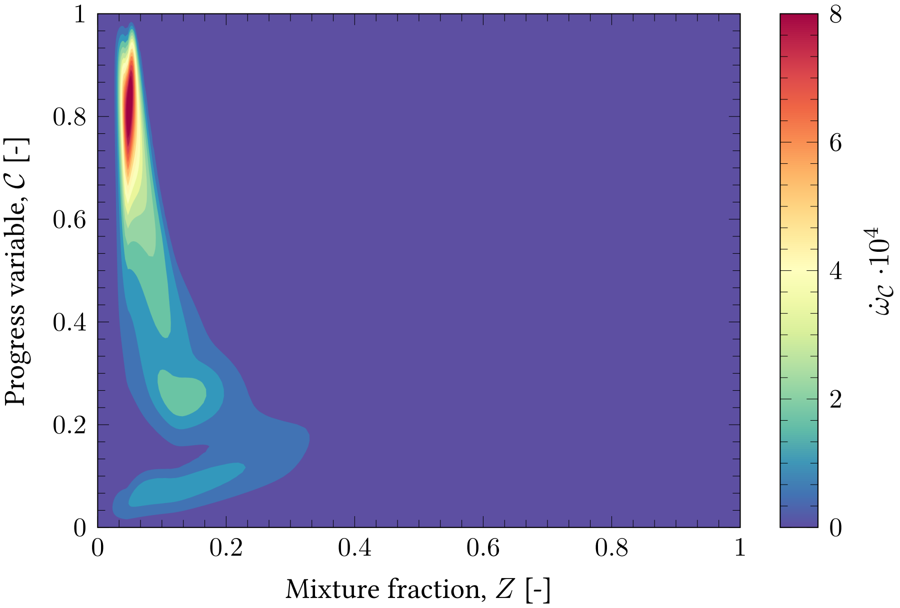

Figure 4.5: Example of a flamelet generated manifold showing reaction rate of $\mathcal{C}$ as a function of mixture fraction and progress variable.

4.3 CSE-FGM Implementation

Interaction of the CSE-FGM combustion model with the CFD code is shown in Figure 4.6. Coupling to the CFD solver is achieved by solving three additional transport equations for the progress variable, mixture fraction and the mixture fraction variance. The Favre averaged (filtered in LES) mixture fraction ($\widetilde{Z}$), and its variance ($\widetilde{Z''^2}$) are used in computation of the β-PDF. This along with the Favre averaged progress variable ($\widetilde{\mathcal{C}}$) are parsed into the CSE routine where the conditionally averaged progress variable ($\langle \mathcal{C}|\eta \rangle$) is computed via inversion as described earlier. The conditionally averaged progress variable along with the Favre averaged mixture fraction are used to lookup the conditionally averaged reaction rate of the progress variable ($\langle \dot{\omega}_{\mathcal{C}}|\eta \rangle$) and conditional species mass fractions ($\langle Y_k|\eta \rangle$) from the FGM table. These are then integrated with the β-PDF to retrieve the respective mean values which are then parsed back into the CFD solver.

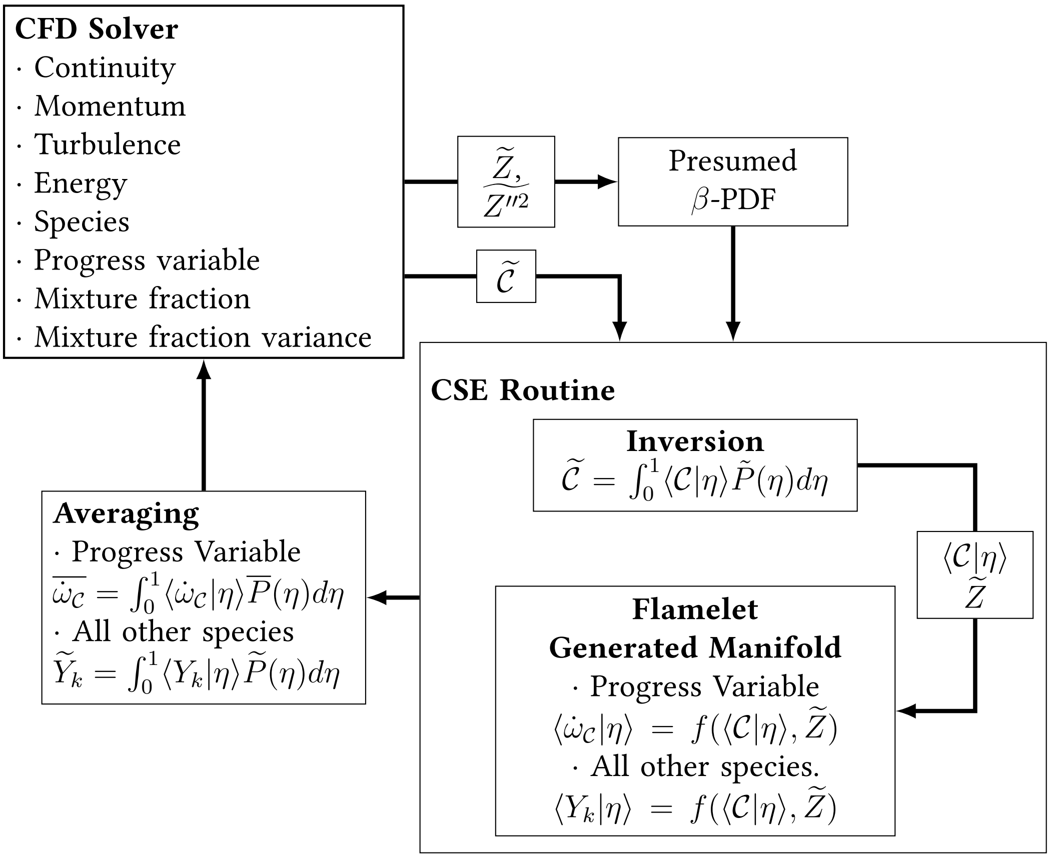

Figure 4.6: CSE-FGM and CFD code interaction.

CHAPTER 5

CSE-FGM Applied to Constant Volume Spray Combustion

5.1 Experimental Test Conditions

Experimental data for model validation is obtained from Sandia National Laboratories through the Engine Combustion Network [133]. A comprehensive set of non-reacting and reacting data are available for spray experiments at engine-relevant conditions. The experimental setup consists of a constant volume combustion vessel approximately cubic in shape with edge length of 108 mm and optical access as shown in Figure 5.1. A 90 micron diameter, single hole, axially aligned injector is mounted centrally with n-Dodecane as the primary injected fuel. A premixed gas-mixture is burned to completion and is used to achieve the relevant ambient conditions before fuel injection. The experimental cases selected for model validation are given in Table 5.1. The 0% ambient O_2 case is used to validate the spray model and ensure the computational model is able to adequately capture the experimental velocity and mixture fraction fields. Both ambient temperature and oxygen concentration sweeps are investigated to evaluate the efficacy of the CSE-FGM combustion model in predicting ignition delay and flame lift-off length over a wide range of operating conditions. The initial species mole fractions used in all simulations are presented in Table 5.2. The presence of CO_2 and H_2O is a result of pre-combustion required to get the combustion vessel to relevant ambient conditions before start of injection.

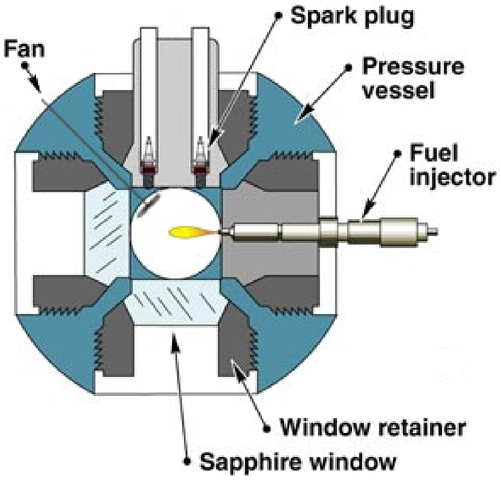

Figure 5.1: Sandia constant volume combustion vessel [133].

Table 5.1: ECN Sandia Spray A experimental nominal test conditions [133]. Test II denotes ECN 'baseline' condition.

Test	O_2 [% volume]	T_{amb} [K]	Unchanged
0	0	900	Fuel = NC12H26
I	15	800	Fuel mass = 14 [mg]
II	**15**	**900**	ϕ_{nozzle} = 0.090 [mm]
III	15	1100	ρ_{amb} = 22.8 [kgm^{-3}]
IV	13	900	T_{fu} = 363 [K]
V	21	900	P_{inj} 150 [MPa]

Table 5.2: ECN Sandia spray A combustion vessel initial species mole fractions [133].

O_2	N_2	CO_2	H_2O
00.00	89.71	06.52	03.77
13.00	77.09	06.26	03.64
15.00	75.15	06.23	03.62
21.00	69.33	06.11	03.56

5.2 Computational Setup

Simulations were performed using the CONVERGE CFD code version-2.4.18 [78]. As in Section 3.3, the PISO algorithm [79] was used to solve the transport equations with the Rhie-Chow [80] algorithm enabled to prevent checker-boarding. Second-order accurate central differencing schemes were used for spatial discretization in all spray simulations, with fully implicit first-order accurate time integration. A variable time-step was used based on CFL, chemistry and spray criteria as detailed in Table 5.3. These settings lead to a time-step which varied between $1 \cdot 10^{-8}$ s to $1.5 \cdot 10^{-7}$ s.

Table 5.3: Time-step control input parameters.

	Value
Initial time-step [s]	1e-8
Maximum time-step [s]	5e-6
CFL$_u$ [-]	0.75
CFL$_\nu$ [-]	2.0
CFL$_c$ [-]	50.0
$mult_{spray}$ [-]	1.0
$mult_{chem}$ [-]	0.5

As in Section 3.3, the Lagrangian-Eulerian framework was used to model the liquid phase with all sub-models used stated in Table 5.4

Table 5.4: Spray simulation discrete phase sub-models.

Sub-models	
Injection	Blob method [85]
Droplet breakup	KH-RT without breakup length [86, 87]
Droplet drag	Dynamic droplet drag [88, 89]
Droplet collisions	No Time Counter [90]
Vaporisation	Frossling correlation [65]
Droplet heat transfer	Ranz-Marshall [66]
Turbulent dispersion	O'Rourke [65]

Table 5.5: KH-RT breakup model constants.

B_0	B_1	C_1	C_t	C_{RT}
0.61	5.0	0.188	1.0	0.1

Primary validation of the CSE-FGM combustion model was done at the ECN baseline condition (Test II) using LES turbulence closure. In this investigation, the one-equation viscosity based LES model was used where the sub-grid turbulent kinetic energy, k_{sgs}, is used to compute the turbulent viscosity as:

$$\nu_t = C_k k_{sgs}^{1/2} \Delta \tag{5.1}$$

where C_k is a model constant and commonly set as 0.05 and Δ is the cube root of the cell volume. Following Yoshizawa *et al.*[134] and Menon *et al.*[135] the sub-grid kinetic energy, $k_{sgs} = \frac{1}{2}\left(\widetilde{u_i u_i} - \tilde{u}_i \tilde{u}_i\right)$, is modelled with a transport equation as:

$$\frac{\partial \bar{\rho} k_{sgs}}{\partial t} + \frac{\partial \bar{\rho} \tilde{u}_i k_{sgs}}{\partial x_i} = -\tau_{ij} \frac{\partial \tilde{u}_i}{\partial x_j} - \epsilon + \frac{\partial}{\partial x_i}\left(\bar{\rho} \frac{\nu_t}{\sigma_k} \frac{\partial k_{sgs}}{\partial x_i}\right) \tag{5.2}$$

The sub-grid stress tensor is then computed as:

$$\tau_{ij} = -2\nu_t \tilde{S}_{ij} + \frac{2}{3} k_{sgs} \delta_{ij} \tag{5.3}$$

where $\tilde{S}_{ij}$ is the strain rate tensor and δ_{ij} is the Kronecker operator. The sub-grid dissipation in this model, ϵ_{sgs} is given as:

$$\epsilon_{sgs} = C_\epsilon \frac{k_{sgs}^{3/2}}{\Delta} \tag{5.4}$$

where C_ϵ is a model constant and typically set as 1.0.

Combustion was modelled with the CSE-FGM combustion model as described in Chapter 4. Additional transport equations must be solved for the progress variable, mixture fraction and mixture fraction variance. These are given as:

$$\frac{\partial \bar{\rho} \widetilde{C}}{\partial t} + \frac{\partial \bar{\rho} \tilde{u}_j \widetilde{C}}{\partial x_j} = \frac{\partial}{\partial x_j}\left(\bar{\rho}\left(D + D_t\right) \frac{\partial \widetilde{C}}{\partial x_j}\right) + \overline{\dot{\omega}_C} \tag{5.5}$$

$$\frac{\partial \bar{\rho} \widetilde{Z}}{\partial t} + \frac{\partial \bar{\rho} \tilde{u}_j \widetilde{Z}}{\partial x_j} = \frac{\partial}{\partial x_j}\left(\bar{\rho}\left(D + D_t\right) \frac{\partial \widetilde{Z}}{\partial x_j}\right) + \overline{\dot{\omega}_Z} \tag{5.6}$$

where D is the diffusivity, $\overline{\dot{\omega}_C}$ is the progress variable source term which is obtained from the FGM tables, $\overline{\dot{\omega}_Z}$ is the spray source term from fuel evaporation and is provided by the spray model. Scalar fluxes are closed by applying the gradient diffusion hypothesis and unity Lewis number assumption, the turbulent diffusivity is then given as:

$$D_t = \frac{C_k \Delta k^{1/2}}{\mathrm{Sc}_t} \tag{5.7}$$

where $\mathrm{Sc}_t = 0.78$ is the turbulent Schmidt number.

In LES, the mixture fraction variance can be approximated through an algebraic relation as [136]:

$$\widetilde{Z''^2} = C_{var}\Delta^2 \left| \frac{\partial \widetilde{Z}}{\partial x_j} \right|^2 \tag{5.8}$$

where C_{var} is a dynamically computed model coefficient.

Flamelet libraries are generated using the methodology outlined in Section 4.2.1 for the conditions listed in Table 5.1. Starting from a mixing solution, a single ICDF is solved for a strain rate of $a = 500$ s^{-1} followed by a series of steady counterflow diffusion flames - which are solved using strain rates descending from $a = 500$ s^{-1} down to $a = 1$ s^{-1} (100 steps). Using a single igniting flamelet at a single strain rate, sampled at multiple time instances to compute the unsteady part of the flamelet libraries has been evaluated by Bekdemir [137] and Ayyapureddi [138], it was found that libraries computed with this configuration were able to correctly predict ignition delay times at low strain rates and maintain the functional dependence of strain rate on ignition delay at higher strain rates. A strain rate of $a = 500$ s^{-1} is selected as the highest non-quenching strain rate as ignition delay has been found to be insensitive for $a < 1000$ s^{-1} at ECN baseline conditions [132, 137]. This trend is also observed for the mechanism used in this study as shown in Figure 5.2. Additionally, strain rate was only shown to have a small effect on species composition at the onset to ignition [132]. All counterflow diffusion flame simulations have been computed with the skeletal mechanism of Luo *et al.*[139] containing 106 species and 420 reactions. The Luo mechanism was derived from the detailed Lawrence Livermore National Laboratory N-alkanes mechanism containing 2755 species and 11,173 reactions [140]. Reduction was carried out with a Direct Relation Graph with Expert Knowledge algorithm and

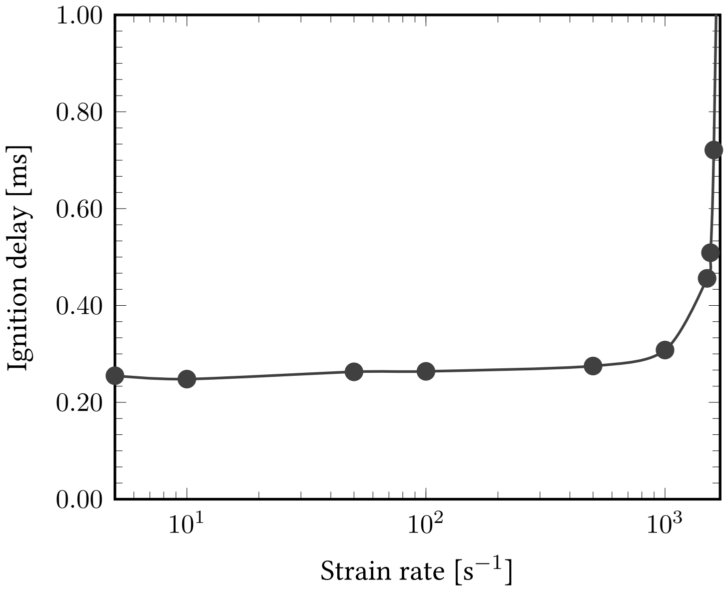

Figure 5.2: Ignition delay (defined as time of 10% increase from T_{ox}) as a function of strain rate for an ICDF using detailed chemistry with the Luo n-Dodecane mechanism: $T_{fu} = 363$ K, $T_{ox} = 900$ K, $P_{amb} = 6.0$ MPa, $O_2 = 15$ %.

sensitivity analysis. The reduced mechanism was then validated over a wide range of conditions against auto-ignition, Jet Stirred Reactor and counterflow flame experimental measurements. The computational domain is cylindrical in shape with a radius of 27 mm and edge length of 108 mm as shown in Figure 5.4. The injector is positioned centrally with injection into the positive x-direction. All boundaries are set as non-slip walls with constant temperature of 461 K as measured in the experiment. The injector nozzle diameter is set as 0.084 mm with discharge coefficient of 0.89 corresponding to Spray A injector 210677 [133]. Approximately 14 mg of n-Dodecane is injected over a duration of 6 ms for both non-reacting and reacting conditions. It should be noted the simulations are run for 1.5-2.0 ms as by this time a quasi steady state flame has been established. ECN recommend using a modelled rate of injection at the relevant test conditions which can be generated using the Virtual Injection Rate Generator tool of CMT-Motores Térmicos [141]. A comparison of the measured and modelled rates of injection at the non-reacting condition (Test 0 in Table 5.1) are shown in Figure 5.3. The experimental rate of injection is measured using momentum based techniques and ensemble averaged over 50 injections, still-more, spikes and consistent oscillations in the mass flow-rate are present throughout the measurement period as seen in Figure 5.3. The spikes are thought to be caused by mass accumulation at the head of spray and the oscillations are partly attributed to pressure fluctuations upstream of the injector [142, 143]. As there is no definitive origin of these artefacts, ECN caution use of the measured profile in CFD simulations. The modelled rate of injection is generated by applying a correction to the injection ramp-up so as to best match the experimental vapour and mixture fraction profiles. The steady state period of the rate of injection is based of filtering of the experimental rate of momentum measurements. Further details of the modelled rate of injection can be found in [144]. A structured grid is generated at runtime with a base cell size of 1.4 mm. Adaptive mesh refinement is enabled based on both velocity (0.1 ms^{-1}) and temperature (5 K) fluctuations with minimum cell refinement of 0.0875 mm. Furthermore, a conical fixed grid refinement of 0.0875 mm is placed along the injector axis to better resolve this high velocity region. In order to maintain a reasonable runtime, the maximum cell count is limited to 2.6 million cells. These cell sizes were determined

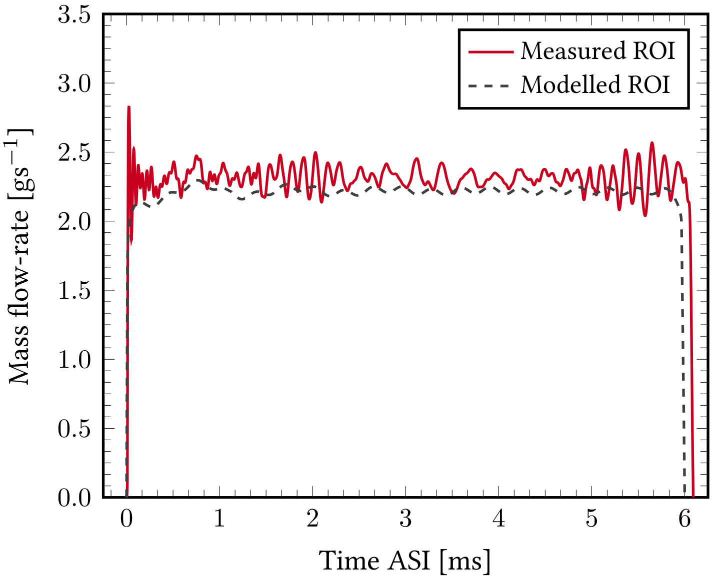

Figure 5.3: Comparison of the measured and modelled rate of injection for Spray A injector 210677 at non-reacting conditions with 6 ms injection duration: P$_{inj}$ = 150 MPa, P$_{amb}$ = 6.0 MPa, T$_{fu}$ = 363 K.

through a grid dependence study conducted at non-reacting conditions (Test 0) of the spray. Further details will be presented in Section 5.3.1. A section of the computational domain showing the computational grid and cell refinement can be seen in Figure 5.5 & Figure 5.6.

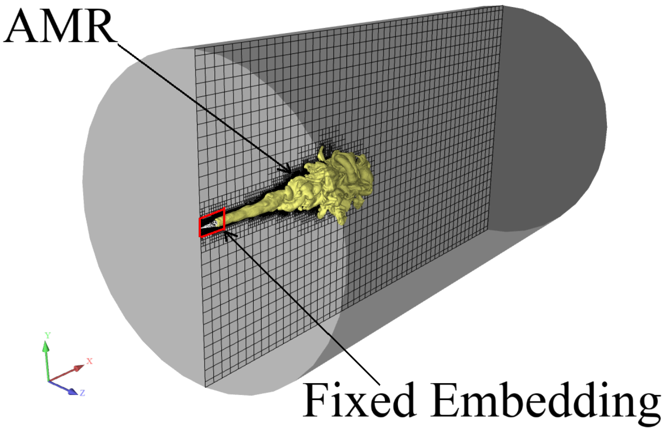

Figure 5.4: Spray computational domain with grid refinement methods.

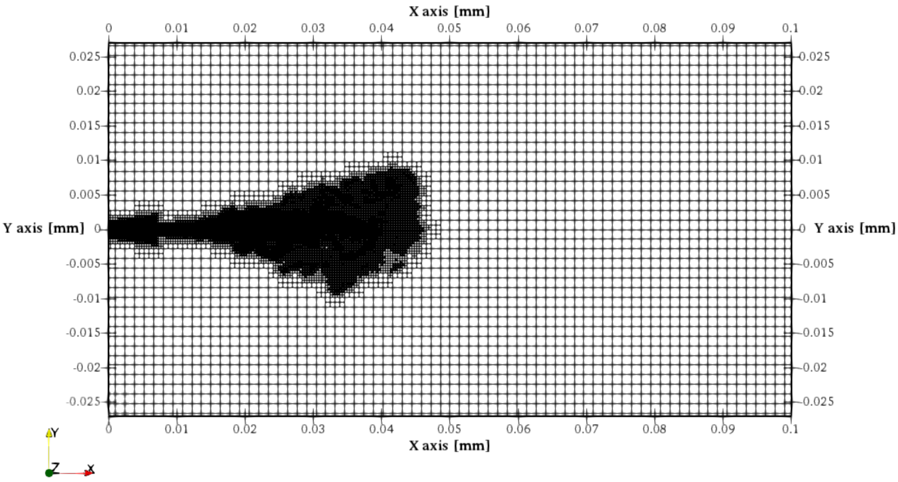

Figure 5.5: Spray computational domain X-Y plane clip showing LES grid.

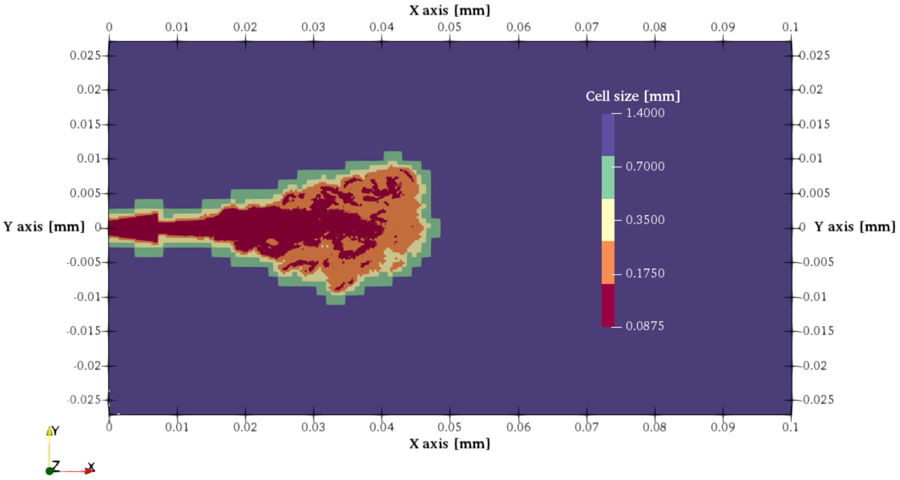

Figure 5.6: Spray computational domain X-Y plane clip showing LES AMR and fixed embedding grid sizes.

5.3 Results and Discussion

5.3.1 LES grid dependence

A grid dependence study of the LES computational setup was conducted for the non-reacting spray condition by varying the minimum grid size from 0.125 mm down to 0.0625 mm. An overview of the grid setup is shown in Table 5.6. Only a single LES realisation is used for the following grid dependence study as it has been demonstrated by Xue *et al.*[145] that a single LES realisation is sufficient to predict global spray parameters (liquid and vapour length) very close to ensemble averaged values. Figure 5.7 presents the liquid penetration lengths for all grid sizes, where it is clear that results are relatively insensitive to grid size after the stead state period is established. Additionally, with exception of the spikes at 0.2 ms for the coarse grid, simulation results compare

Table 5.6: LES grid dependence parameters.

Grid	Coarse	Medium	Fine
Min cell size [mm]	0.125	0.0875	0.0625
Spray parcels$\cdot 10^6$ [-]	0.8	2.4	3.2
Max cell number$\cdot 10^6$ [-]	1.4	2.6	5.0
Core-hours for 1 ms [-]	252	672	1440

well with experimental measurements over the injection duration. This behaviour could be attributed to the requirement of increasing the number of parcels as the grid is refined. As such, the liquid-volume fraction in each cell is maintained across grid sizes, thereby the liquid-gas phase interactions remain unaffected. The vapour penetration shown in Figure 5.8 is more sensitive to grid size, with the medium and coarse grids over-predicting vapour penetration length. The finest grid size of 0.0625 mm leads to an improved prediction of vapour length across the injection duration when compared to experimental measurements. However, it can be seen that the medium grid size of 0.0875 mm is in good agreement experimental measurements after 0.5 ms. Consequently, the medium grid was chosen for all further LES simulations as it provides a reasonable balance between computational expense and accuracy compared to experimental measurements.

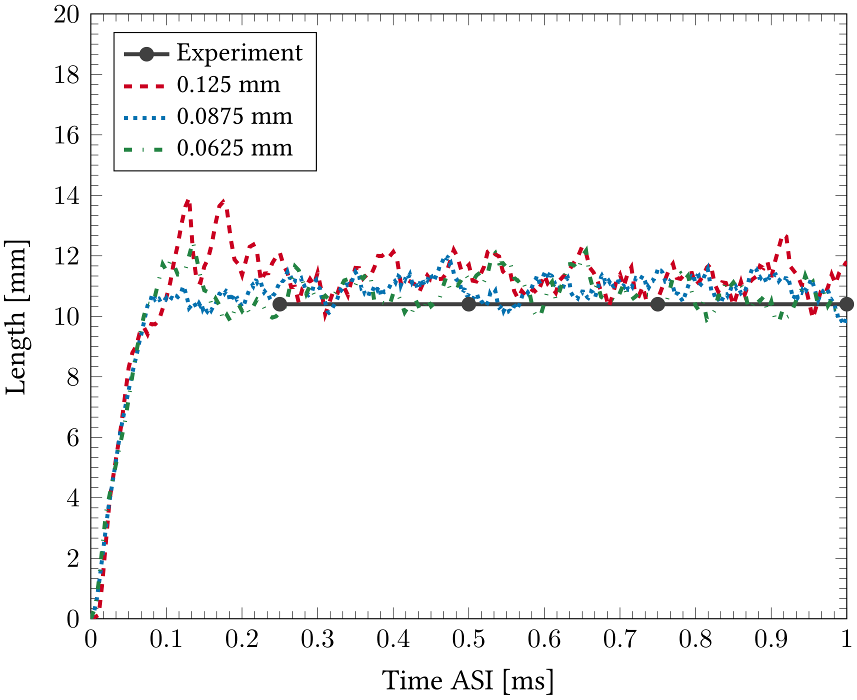

Figure 5.7: Liquid penetration length as a function of grid size. Liquid length is defined as the axial location of 99% liquid mass threshold. Experimental data repeated from [133].

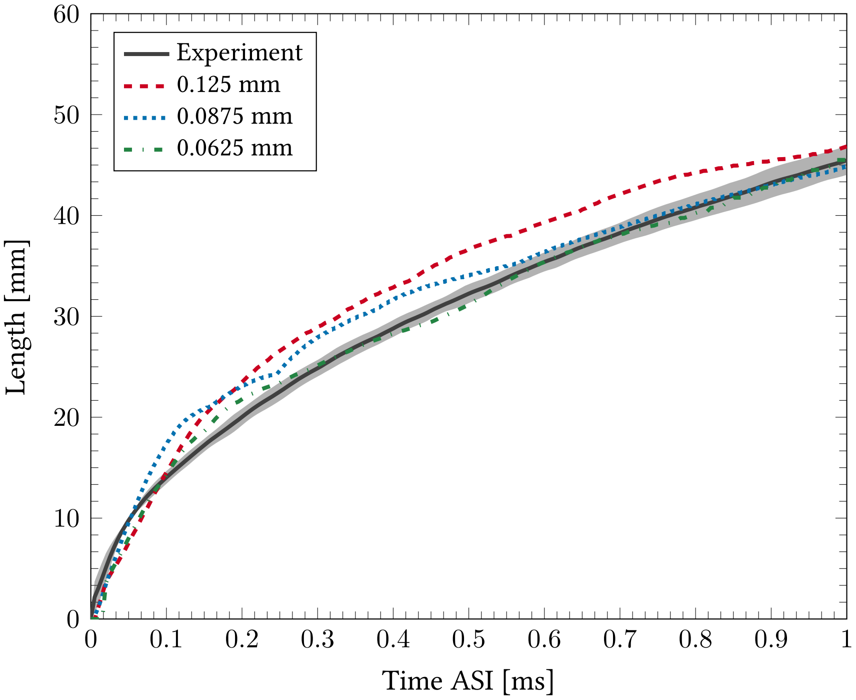

Figure 5.8: Simulation vapour penetration length as a function of grid size. Vapour length is defined as axial location of 1% vapour mass threshold. Shaded area represents experimental uncertainty. Experimental data repeated from [133].

Estimating LES quality

In order to further validate selection of the 0.0875 mm grid size, quality of the LES computational setup used here is estimated using the Pope criterion [16, 146]. The Pope criterion M, quantifies the fraction of resolved to modelled turbulent kinetic energy (TKE). A value of $M = 1$ is where all TKE has been resolved and a value of $M = 0$, is where all TKE has been modelled.

$$M\left(x,t\right) = \frac{k_r\left(x,t\right)}{k_r\left(x,t\right) + k_{sgs}\left(x,t\right)} \tag{5.9}$$

where k_{sgs} is the sub-grid TKE which is calculated by the one equation LES model as Equation 5.2 and k_r is the resolved TKE which is computed as:

$$k_r = \frac{1}{2}\left\langle u_{RMS}^2 + v_{RMS}^2 + w_{RMS}^2\right\rangle \tag{5.10}$$

where u_{RMS} denotes the root mean square (RMS) value of the velocity in the x-direction and '$\langle\ \rangle$' represents the ensemble average over the number of LES realisations or temporal average over the number of samples. The RMS quantities are computed as:

$$\phi_{RMS} = \sum_{i=1}^{N} \frac{\sqrt{\left(\tilde{\phi}_{avg} - \tilde{\phi}_i\right)^2}}{N}, \qquad \tilde{\phi}_{avg} = \sum_{i=1}^{N} \frac{\tilde{\phi}_i}{N} \tag{5.11}$$

where $\tilde{\phi}_{avg}$ is the mean value, i is the realisation index and N is the total number of realisations or samples.

Figure 5.9a shows the Pope criterion calculated for the non-reacting condition using a single realisation and temporal averaging once a quasi steady state jet has been established. Pope [146] recommends a value of $M = 0.8$ for 'Hi-Fidelity LES' whilst Rutland [147] recommends values between $M = 0.6 - 0.8$ for 'Engineering LES'. It can be seen from Figure 5.9a that in the near nozzle region ($x < 5$ mm) where the liquid jet penetrates and velocity gradients are large (Figure 5.9b), values of M are below 0.2 revealing a large proportion of the TKE is modelled in these areas even with the fixed embedding refinement. Further downstream, in most of the gas jet region where velocities are lower, values of M are 0.8 indicating the grid resolution is sufficiently fine for LES. It should be noted that the dissipative nature of the current numerical approach has not been explicitly studied, hence, caution must be applied when interpreting these results as the Pope criterion neglects TKE dissipation by the numerical method, as such, highly dissipative schemes would result in $k_{sgs} \to 0$, incorrectly indicating all the TKE has been resolved [148, 149].

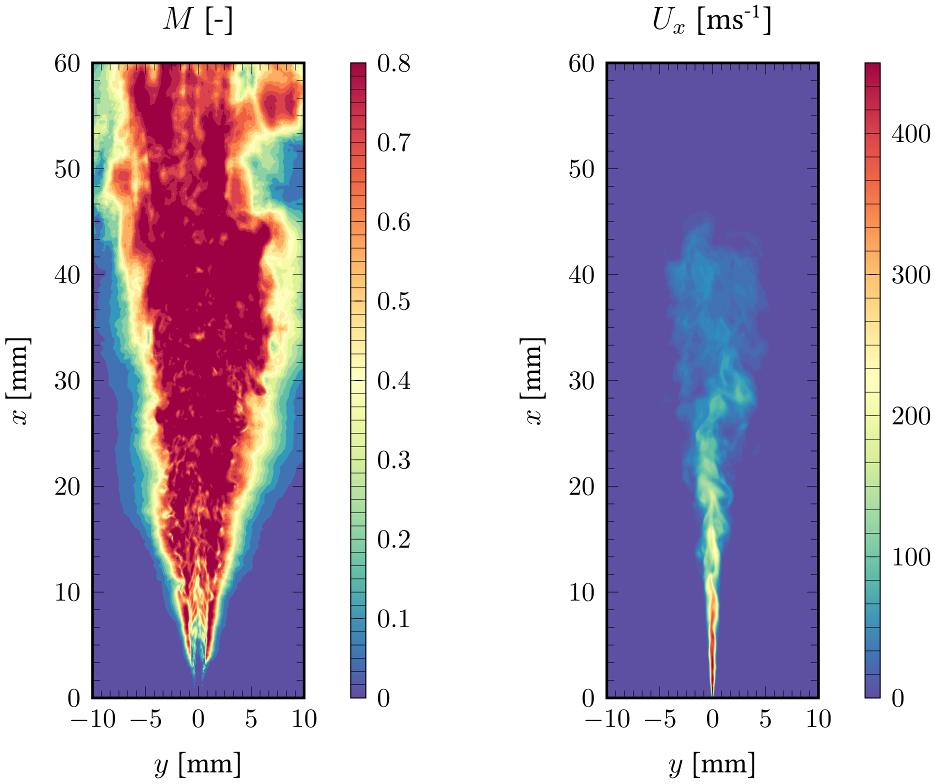

(a)

(b)

Figure 5.9: (a) Pope criterion M and (b) axial velocity in X-Y plane at non-reacting condition, Test 0.

5.3.2 Non-reacting vaporising spray

When using LES it is necessary to simulate multiple realisations or perform temporal averaging in order to obtain statistically relevant averaged quantities. Senecal *et al.*[150] simulated 20 realisations of ECN Spray A with LES and have shown nine realisations is a large enough sample to capture experimental velocity and mixture fraction distribution with mean absolute errors of 2.0 ms^{-1} and 0.005 – 95% of the time respectively. Pei *et al.*[151] found that ignition delay only varied by 5% over 5 realisations, however, flame lift-off length varied significantly between LES realisations. Ameen *et al.*[152] only simulated 5 realisations and took advantage of the axisymmetry of ECN Spray A and performed spatial averaging on 35 planes in the azimuthal direction, leading to self-similar profiles for mixture fraction, temperature, OH and soot. Expectedly, centreline profiles still showed large variance compared to the experiment as there are only five samples with all azimuthal planes sharing the same centreline. Further improvement in statistical convergence can be obtained by also applying time averaging once the jet has reached quasi steady state – where in non-reacting conditions, this can be considered the time after the gas jet has stabilised and in reacting conditions, the time once the flame lift-off length has stabilised [132, 153, 154, 155].

Stabilisation of the gas jet is taken as the time instance the head of the jet passes out of the test section. The test section is defined from 17.85 mm to 50 mm in the axial direction as this is the region for which experimental mixture fraction and velocity data is measured. Experimental mixture fraction is measured using Rayleigh Scattering with sampling done at long delays (3.2-7.0 ms) after the start of injection and ensemble averaged over 20-40 injections depending on the test condition [156]. This is to make certain the jet is steady state and at that jet transients do not affect measurements. Experimental velocity measurements are taken with time-resolved PIV and ensemble averaged over ≈20 injections at defined time instances after the start of injection [157]. Velocity measurements in the near nozzle region are not considered accurate as the proximity of the liquid jet generates high intensity Mie scattering signals that interfere with particle imaging. Additionally, the PIV particle density is too low in this region as not enough particles have been entrained in the spray. As such only velocity measurements downstream of $x = 20$ mm will be considered.

As it is computationally prohibitive to run simulations for long durations (3.2-7.0 ms) as in the experiment, as well as quasi steady state experimental reacting data being available before 1.5 ms – the following two approaches are used to validate the computational model with experimental measurements:

- Mixture fraction: temporal and spatial averaging of 1 LES realisation using 25 temporal samples between 1.5-2.0 ms and 12 azimuthal planes for each sample.
- Velocity: ensemble and spatial averaging of 5 LES realisations and 12 azimuthal planes for each realisation at 1.0 ms ASI.

Each LES realisation has been perturbed by varying a random number seed that is input into the random number generator within the injection model. Varying the random number seed will change the initial position and velocity of an injected spray parcel. Whilst this method of perturbation is purely numerical, using a random number seed is expected to account for the variations observed from one injection event to another. Furthermore, it was found by Ameen *et al.*[152] that results from random number seed perturbations were comparable to perturbations originating from varying the initial turbulence intensity. Figure 5.11 qualitatively shows the difference in mixture fraction distribution between the 5 realisations. Spatial averaging is applied in the azimuthal direction for each realisation as illustrated in Figure 5.10. Each plane is 60 mm long and 30 mm wide, which is then discretized by 0.08 mm to preserve resolution.

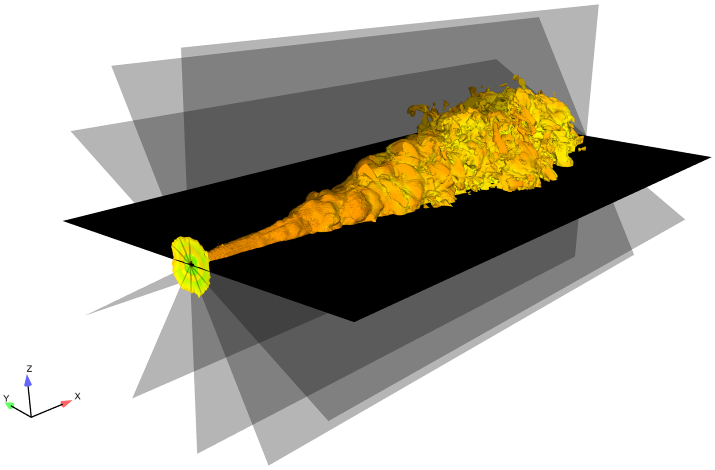

Figure 5.10: ISO volume of spray jet showing azimuthal averaging planes.

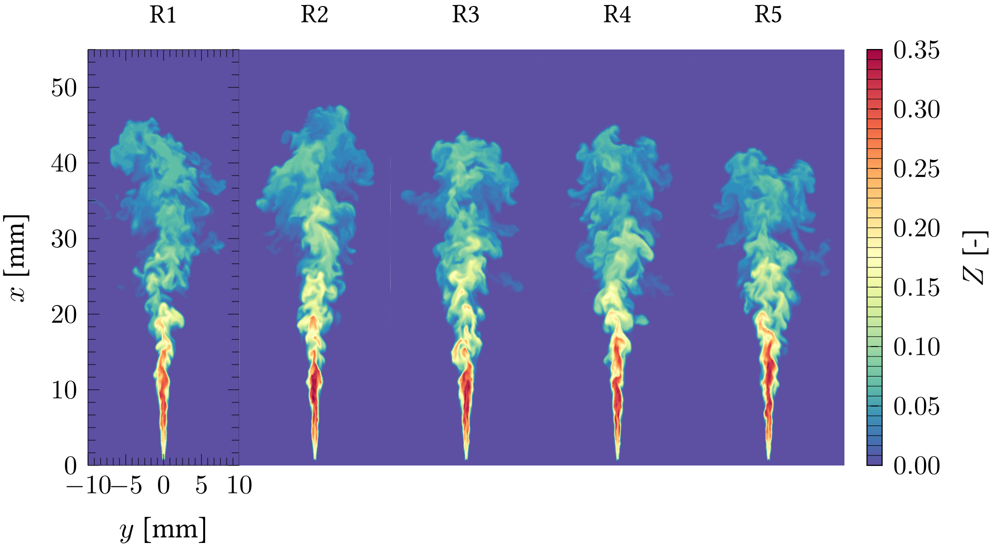

Figure 5.11: Mixture fraction distribution at 1.0 ms ASI for 5 LES realisations perturbed by a random number seed.

Figure 5.12 shows the liquid and vapour lengths between simulation and experiment. Only a mean value of liquid length is available from the experiment which is matched very well by the LES model. Vapour penetration length is slightly over-predicted by the LES model early in the injection duration. However, after 0.5 ms, the simulation is in good agreement with the mean experimental measurement.

The axial mixture fraction distribution is presented in Figure 5.13 where it can be seen that the averaged simulation result under-predicts mixture fraction compared to the experiment across most of the axial length. Standard deviation between simulation and experiment is comparable and the predicted results do fall within experimental variance. These results are consistent with LES studies of this experimental test point in literature – using similar models and grid resolution [132, 150, 154, 155, 158]. The under-prediction in centreline mixture fraction is attributed to the early sampling time in the simulations [150]. As experimental mixture fraction is measured at long delays (3.2-7.0 ms) after the start of injection, the mixture fraction field has not fully developed in the simulations which are only run until 2.0 ms. Furthermore, Wehfritz *et al.*[159] has reported that increased spatial resolution (47.5 μm) resulted in an improved

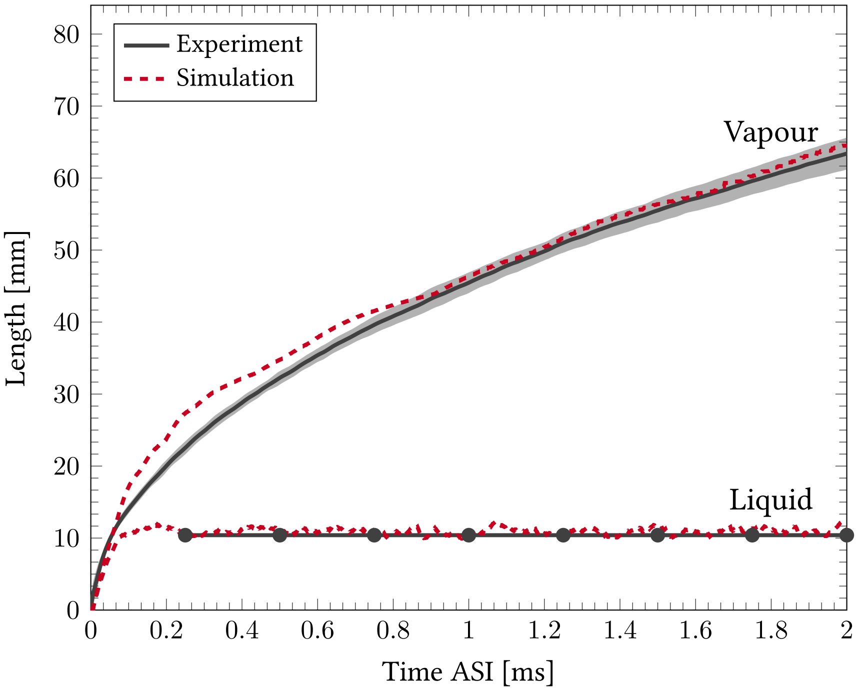

Figure 5.12: Experimental and simulation penetration lengths. Vapour length is defined as axial location of 1% vapour mass threshold. Liquid length is defined as the axial location of 99% liquid mass threshold. Shaded area represents experimental uncertainty.

centreline mixture fraction predictions. This has not been investigated due to the high computational cost. The velocity fields which are sampled at the same time instance after start of injection (1.0 ms) between simulation and experiment are shown in Figure 5.14. There is good agreement between the ensemble averaged simulations and experimental measurements across the axial distance. Expectedly, simulation variance is high due to the low number of samples (5). From Figure 5.15, it can be seen that simulation radial profiles of mixture fraction and velocity are in good agreement with experimental measurements at all axial locations. These axial locations have been selected as the experimental lift-off measurements fall between 8-30 mm (Non-reacting data is unavailable for $x < 17.85$ mm). Accordingly, there is an under-prediction in centreline mixture fraction, however, mean and variance predictions are improved when moving away from the centreline. As seen earlier, ensemble averaged velocity predictions correlate very well to experimental measurements with good agreement in the radial direction as well.

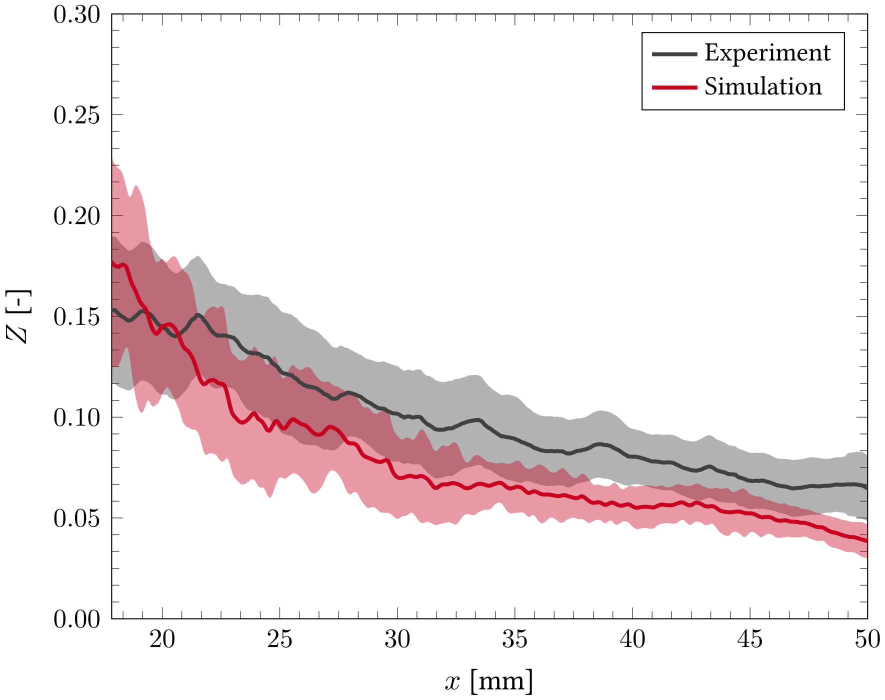

Figure 5.13: Axial comparison of experimental and simulation mixture fraction distribution. Shaded area represents standard deviation.

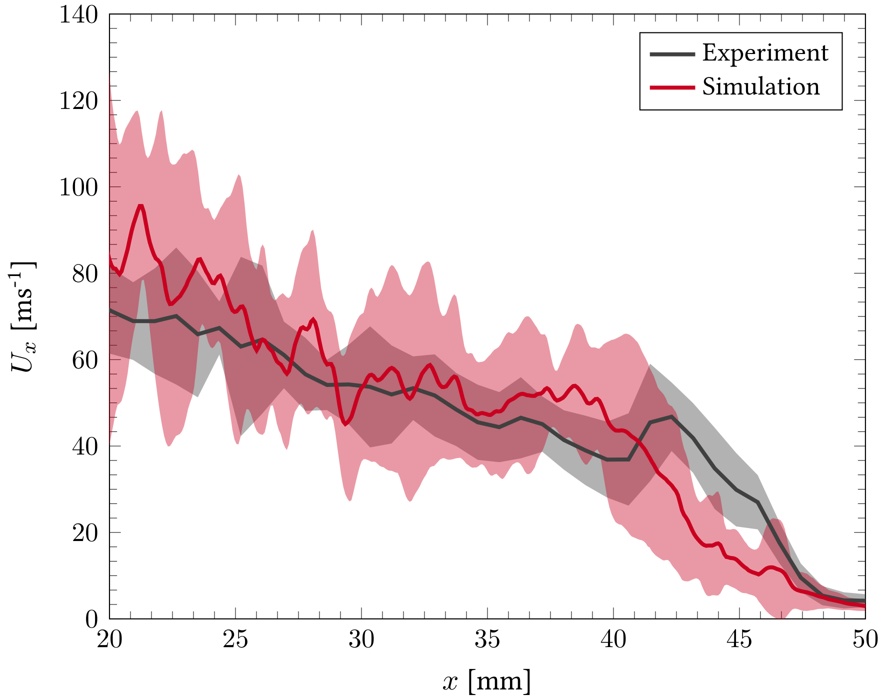

Figure 5.14: Axial comparison of experimental and simulation velocity fields at 1.0 ms ASI. Shaded area represents standard deviation.

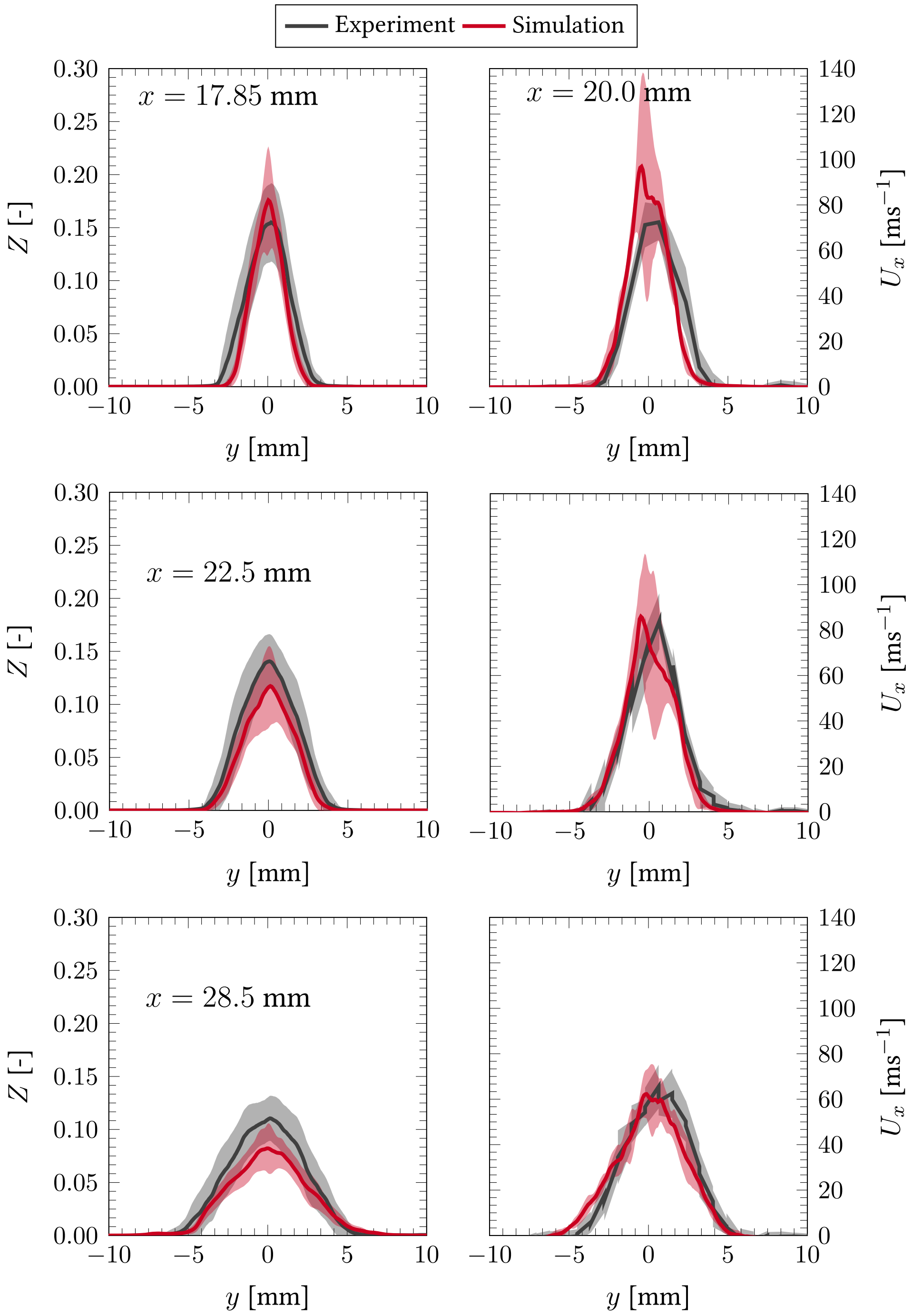

Figure 5.15: Radial profiles of mixture fraction (left) and axial velocity (right) for experiment and simulation at three axial positions. Shaded area represents standard deviation.

5.3.3 Reacting spray

The results of the CSE-FGM model applied to reacting ECN spray conditions will be presented in this section. Firstly, CSE-FGM/LES predictions of global combustion indicators will be given followed by comprehensive examination of the model's ability in predicting local flame dynamics and structures observed in the experiment for the ECN baseline condition. Lastly, CSE-FGM/RANS simulations of conditions given in Table 5.1 will be presented highlighting the CSE-FGM models capability in predicting combustion over a wide range of experimental test conditions.

In standard ECN experimental measurements, both flame lift-off length and ignition delay are measured using high-temperature chemiluminescence to detect light emitted from the OH* radical. For flame lift-off length, the OH* signal is integrated over a 0.5 ms duration when the flame has stabilised to provide a time-averaged image of OH*. The flame lift-off length is then computed by taking the first axial location in this image that reaches 50% of the levelled-off OH* signal intensity. In a similar manner to flame lift-off length, ignition delay is computed as the first time instance that the OH* signal intensity level reaches the 50% levelled-off intensity threshold value. Further details on experimental diagnostics can be found in [133, 157]. As most n-Dodecane mechanisms do not include OH* reactions, the agreed upon definitions for flame lift-off length and ignition delay by ECN members for CFD comparisons are given as [160]:

- Ignition delay: the time instance after start of injection of maximum temperature gradient:

  $$\tau_{idt} = \tau_{\left(\frac{dT_{max}}{dt}\right)} - \tau_{SOI} \tag{5.12}$$

  where $T_{max} = \max(T(x,y,z,t))$ and τ_{SOI} is the start of injection timing.

- Flame lift-off length: the first axial location (relative to injector position) at which the Favre averaged OH mass fraction reaches 2% of the domain maximum (instantaneous maximum).

5.3.4 Global view of ignition delay timing and flame lift-off length

Figure 5.16 shows the temporal evolution of the temperature field for the ECN baseline condition. The typical two-stage ignition behaviour of the n-Dodecane fuel jet is qualitatively predicted by the CSE-FGM/LES model. At 0.15 ms ASI, the cold fuel jet has penetrated far into the hot ambient gas and has not yet undergone significant mixing as shown by the narrow jet structure. By 0.30 ms ASI, low temperature reactions have begun, initiating first-stage ignition and low temperature heat release in the periphery of the vapour jet. The onset of second-stage ignition takes place approximately at 0.40 ms ASI and occurs in the head of the jet where the velocity field is relatively low. The vapour temperature here rises 300-400 K above the ambient temperature and volumetric ignition takes place with multiple ignition kernels. This is followed by expansion of a high temperature diffusion flame (0.6-0.8 ms) which eventually stabilises downstream of the injector. Additionally, at approximately $x = 30$ mm, the diffusion flame begins to thicken radially. This phenomenon has been observed in previous studies [151, 161] and is attributed to be the effect of the recirculation zone behind the head of the jet. These vortices enhance turbulence levels locally and lead to thickening of the flame in this area. Table 5.7 quantitatively shows the comparison of experimental and simulation ignition delay and flame lift-off length. It can be seen that the CSE-FGM/LES model is able to successfully predict both combustion metrics very close to experimental measurements.

Table 5.7: Ignition delay time and flame lift-off length for ECN Spray A baseline condition. Experimental data repeated from [133].

Test II (900 K, 15% O_2)	Experiment	CSE-FGM/LES
Ignition delay time [ms]	0.40-0.44	0.41
Flame lift-off length [mm]	15.80-17.90	18.08

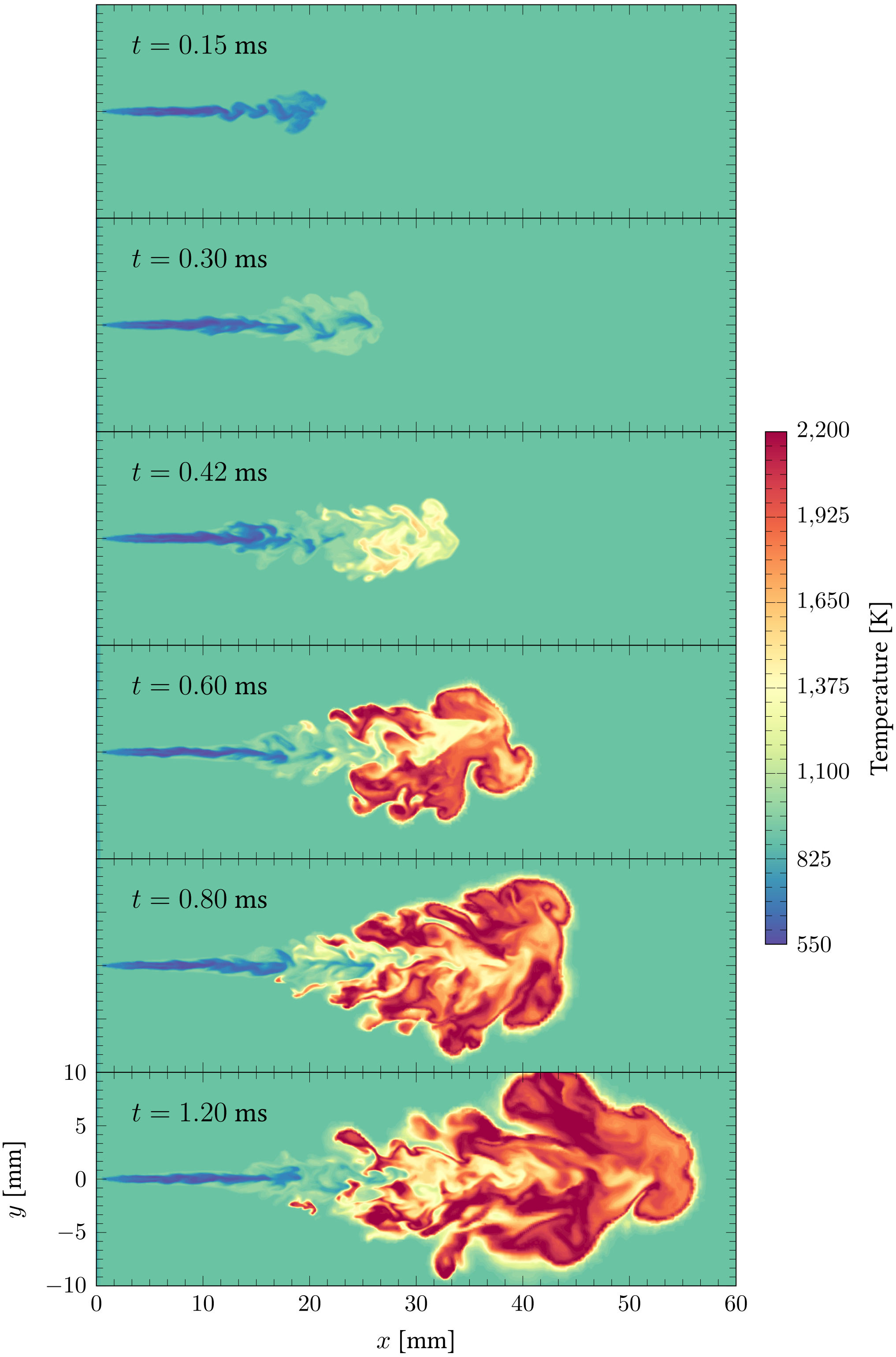

Figure 5.16: Instantaneous temperature fields from CSE-FGM/LES at the ECN baseline condition. The time after start of injection is shown in the top left hand-side of image.

5.3.5 Ignition in mixture fraction space

Figure 5.17 shows the temporal evolution of the simulation in mixture fraction-temperature space. A short time after injection, most points lie close to the mixing line. However, low temperature reactions have begun to take place in the radial spray periphery. These reactions first occur in leaner mixtures as these are at the highest temperature in the unburnt flow field. This is highlighted by the sub-label (i): which shows a minor increase in conditional temperature at 0.19 ms ASI in Figure 5.17. At 0.30 ms ASI, first-stage ignition is underway as seen by the increase in formaldehyde mass fraction, which is a key species used in tracking first-stage ignition. The low temperature reactions here coupled with the high scalar dissipation rate in this region initiate a turbulent cool-flame which transports species and heat release to colder and richer mixtures. This is clearly seen by the shift in conditional temperature (ii), from leaner to richer mixtures. At 0.40 ms ASI, second-stage ignition is initiated with multiple high temperature points (iii) seen over a broad range ($Z = 0.08 - 0.2$) of rich mixture fraction. The consumption of hydrogen-peroxide at the head of the spray also signifies the onset of second-stage ignition as its decomposition is critical in promoting high temperature reactions. Between 0.40-0.44 ms ASI, the highly stratified flow field formed from high temperature ignition initiates turbulent flame propagation (iv) from richer to leaner mixtures. The consumption of formaldehyde and hydrogen-peroxide are clearly seen at the head of the spray. Additionally, the increase in hydroxyl mass fraction and its associated hot-spots confirm the occurrence of high temperature reactions and volumetric ignition. At 1.20 ms ASI a quasi-steady state diffusion flame has been established downstream of the injector and maxmimum temperatures peak at the stoichiometric mixture fraction (v). Furthermore, the spatial distribution of formaldehyde and hydrogen-peroxide stabilise upstream of the high temperature diffusion flame. This is illustrated in the Figure 5.18 which highlights main characteristics of a typical spray flame and their visual definition. The results presented here are consistent with experimental observations [157, 162, 163, 164] and previous numerical studies [132, 151, 154, 155, 165, 166, 167, 168, 169] - confirming the CSE-FGM/LES model is successfully able to capture not only ignition delay but also correctly predict the underlying physical processes in combustion of high pressure fuel sprays.

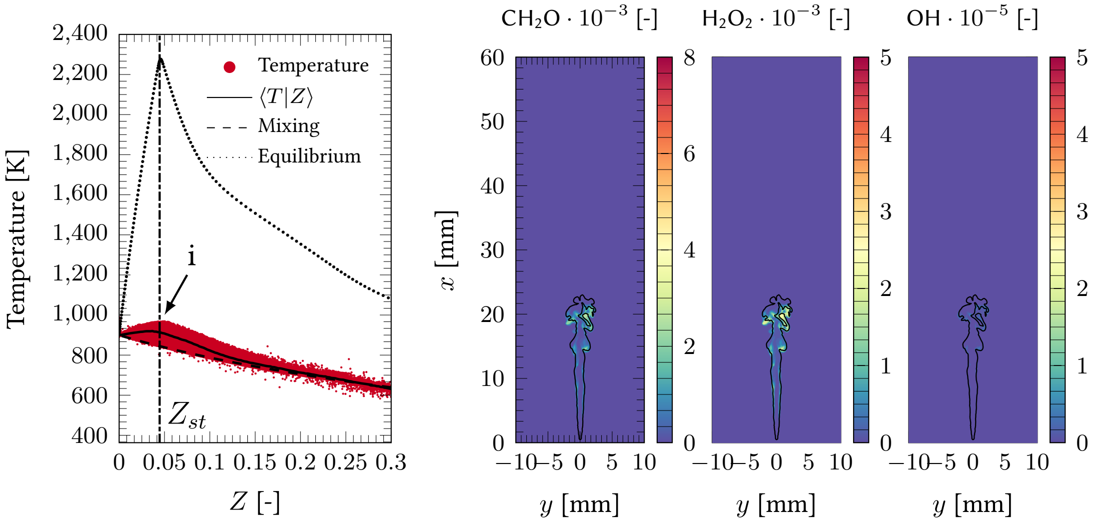

(a) 0.19 ms ASI.

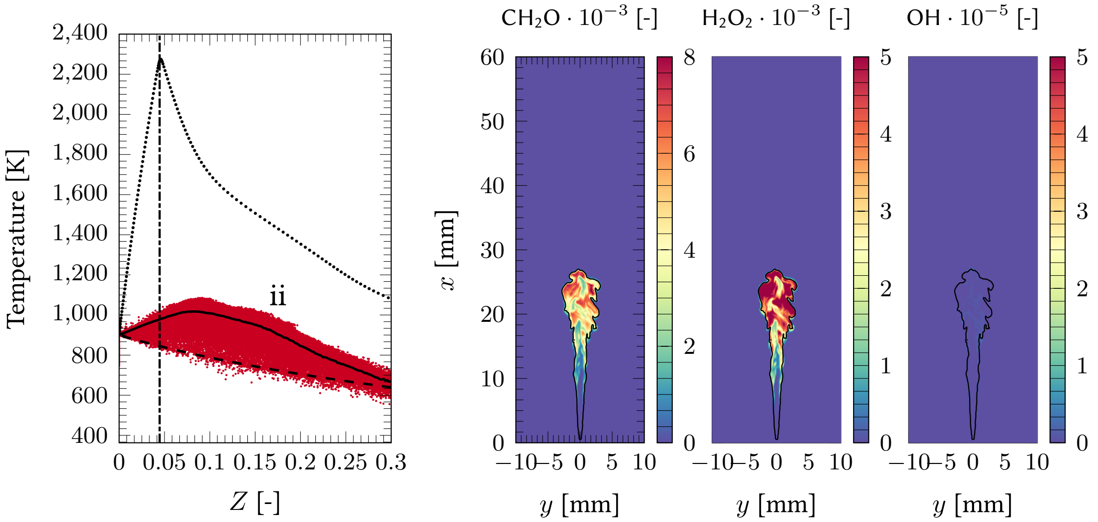

(b) 0.30 ms ASI.

Figure 5.17: Scatter plot in Z-T space with X-Y cut-planes of (1) formaldehyde, (2) hydrogen-peroxide and (3) hydroxyl. $Z_{st} = 0.045$ denotes the stoichiometric mixture fraction. The solid black line in X-Y cut-planes is the contour of stoichiometric mixture fraction.

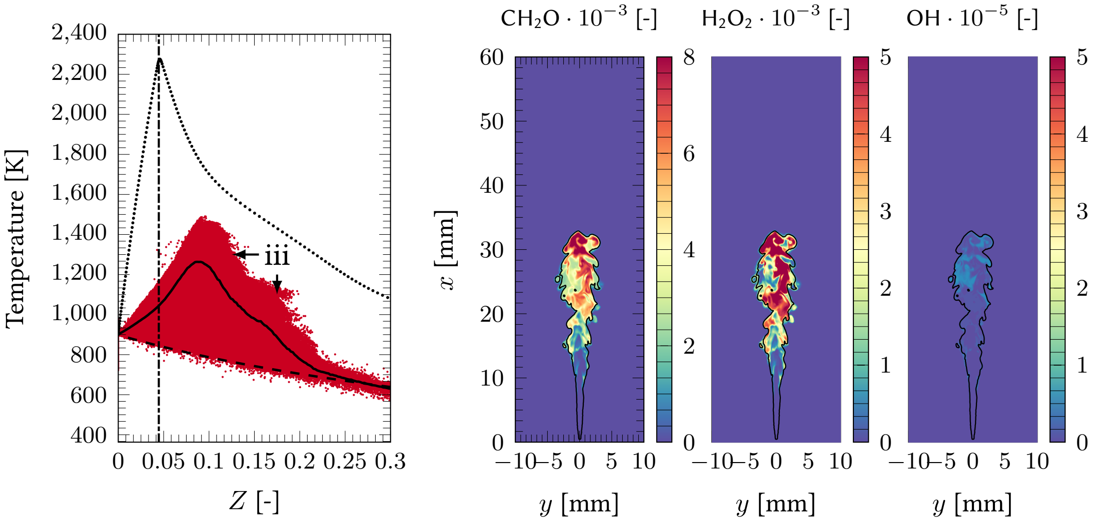

(c) 0.40 ms ASI.

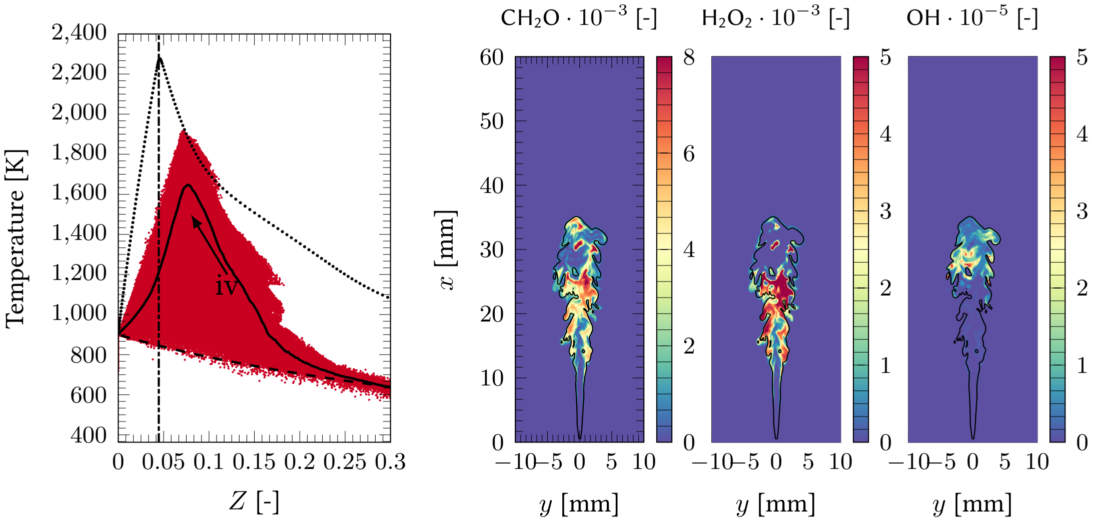

(d) 0.44 ms ASI.

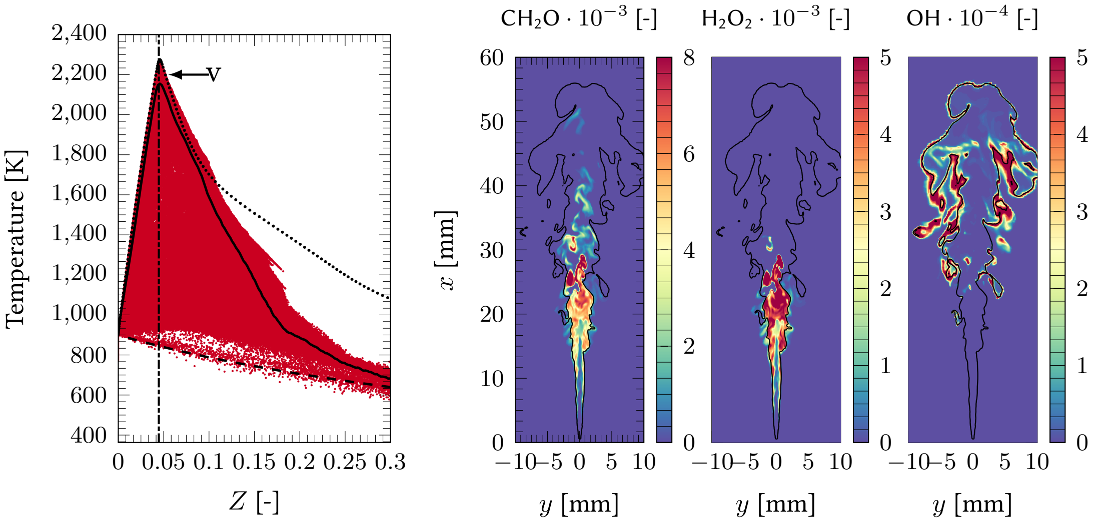

(e) 1.20 ms ASI.

Figure 5.17: Continued

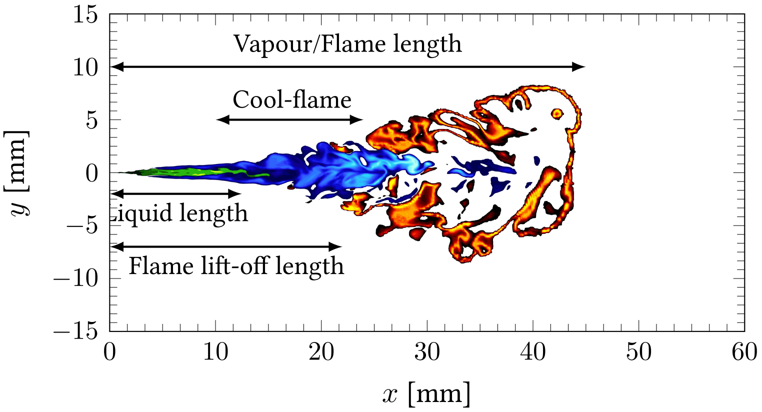

Figure 5.18: Schematic of a stabilised spray flame: green is the n-Dodecane fuel, blue is the cool-flame and is defined by presence of formaldehyde and orange is the high temperature diffusion flame which is defined by the presence of hydroxyl.

5.3.6 Flame stabilisation

The position of flame stabilisation is known as the flame lift-off length and as explained previously, is measured using OH^* chemiluminescence. As the 2% OH criterion is applied in CFD, it is important to evaluate the CFD prediction of the OH field. Maes *et al.*[170] performed experimental measurements using planar laser-induced fluorescence (PLIF) of OH at various ECN Spray A conditions. A comprehensive set of data was gathered with ensemble averaged images generated using 5-20 injections depending on the test condition. A complete description of the optical setup and measurement procedures can be found in [170]. Figure 5.19 shows the predicted OH mass fraction distribution compared to the experimental PLIF measurements at 0.8 ms ASI. The loss of signal intensity in the right hand branch of OH PLIF measurements is a result of attenuation of the excitation laser light by poly-aromatic-hydrocarbons and soot in central areas of the spray [171, 172]. The macro features of the OH field are captured reasonably well by the simulation as shown by the two distinct branches of OH, with each branch expanding in the radial direction as the axial distance is increased. In addition, the onset of OH is comparable between simulation and experiment at approximately $x = 15$ mm.

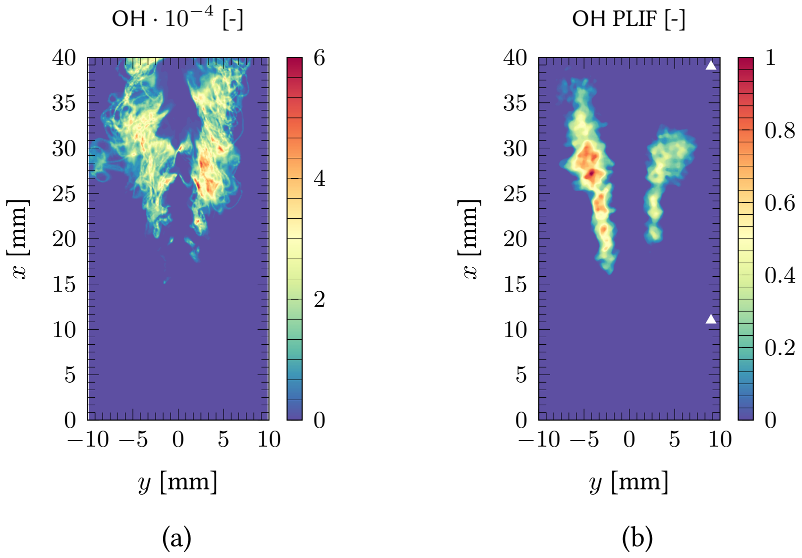

Figure 5.19: Comparison of (a) CSE-FGM/LES spatially averaged OH mass fraction and (b) ensemble-averaged experimental PLIF OH measurements at 0.8 ms ASI. Laser sheet location is marked by white triangles. Experimental images reproduced from [170].

Figure 5.20 illustrates the OH distributions once a quasi steady-state flame has been established. Qualitatively, the predicted OH distribution is comparable to the experiment with two branches expanding in both radial and axial directions. However, the onset location of OH is under-predicted at this time instance as well as the OH field being more diffuse than the separate OH branches seen in the experiment. This could be attributed to the experimental methodology, where it can be seen from [170] that differences in optical setup resulted in qualitatively different OH distributions at the same test condition. These differences are shown in Figure 5.21 where the OH structure as measured by IFP Énergies nouvelles (IFPEn) is considerably more diffuse than that of Eindhoven University of Technology (TU/e). In general, the typical spray structure is observed where a fuel rich core is enveloped by a high temperature field as indicated by the presence of OH. It is also interesting to note that in the experimental measurements, the onset of OH (18.94 mm) is approximately 1.55 mm downstream of the onset of OH* (17.39 mm). This is an important consideration as it will influence confidence in the CFD flame lift-off length in that the OH threshold may not be a suitable enough criteria to make absolute comparisons against experimental measurements based on OH*.

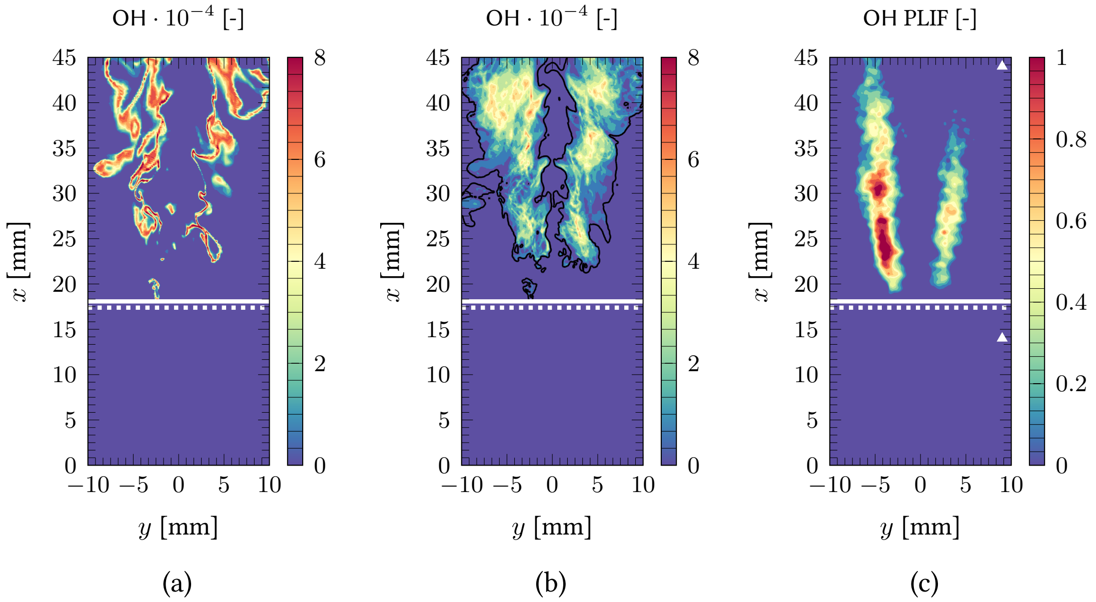

Figure 5.20: Comparison of (a) CSE-FGM/LES instantaneous OH mass fraction field at 1.20 ms ASI, (b) spatially-averaged CSE-FGM/LES OH mass fraction field at 1.20 ms ASI, (c) ensemble-averaged OH PLIF measurements at 4.70 ms ASI. The white solid line denotes CSE-FGM/LES flame lift-off value, the white dashed line denotes steady state experimental flame lift-off value (based on OH*) from Maes *et al.*[170]. Laser sheet location marked by white triangles. Experimental images reproduced from [170].

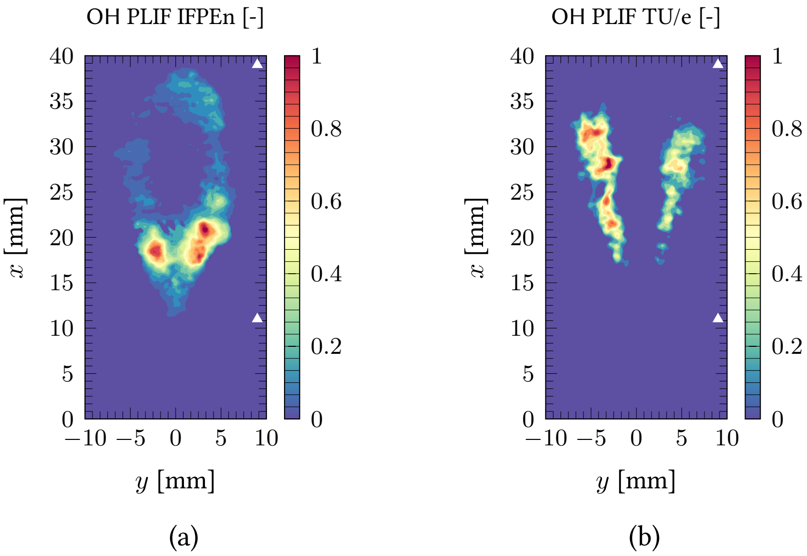

Figure 5.21: Comparison of ensemble-averaged experimental PLIF OH measurements at 0.7 ms ASI for (a) IFPEn and (b) TU/e. Laser sheet location is marked by white triangles. Experimental images reproduced from [170].

Flame stabilisation in high pressure fuel sprays is generally understood as being controlled by auto-ignition and moderated by turbulent diffusion of heat and radicals in/out of the flame. Thereby, flame lift-off length is regulated by the axial distance at which flow conditions do not support the formation and growth of ignition kernels. Influence of the flow field on the flame structure can be quantified using the scalar dissipation rate. In LES, the scalar dissipation is modelled as:

$$\widetilde{\chi} = \widetilde{\chi}_{sgs} + \widetilde{\chi}_r = \frac{D_t}{\Delta^2}\widetilde{Z''^2} + 2D\left|\frac{\partial \widetilde{Z}}{\partial x}\right|^2 \tag{5.13}$$

where $\widetilde{\chi}_r$ is the resolved and $\widetilde{\chi}_{sgs}$ is the sub-grid component of the scalar dissipation rate. The process of flame stabilisation visualised by tracking an ignition kernel near the flame lift-off height. Figure 5.22 shows the temperature and scalar dissipation rate evolution near the flame lift-off location for the CSE-FGM/LES model. The highly unsteady flow leads to large fluctuations in scalar quantities and as shown in Figure 5.22, streaks of low and high scalar dissipation rates are intervolved within the flame. Following the ignition at 0.95 ms ASI as highlighted by the sub-label (i). It can be seen that this ignition event takes place in regions of low scalar dissipation rate where $\chi < 1$ s^{-1} and $Z \approx Z_{st}$. This is confirmed by plotting the radial profiles of temperature and scalar dissipation rate at point (i) which are shown in Figure 5.23. These kernels begin to grow (ii) and merge (iii) with other ignited gas pockets as seen at 0.99 ms ASI. Convection drives these hot regions further downstream merging with other gas pockets and finally the main flame (iv) at 1.02 ms ASI. This process takes place throughout the flame with multiple ignition spots forming, growing and then merging with the main flame. In addition to ignition taking place, extinction is also occurs in this flame. This is observed by tracking a ignited gas pocket denoted by sub-label (A) at 0.95 ms ASI in Figure 5.22. The radial profiles of temperature and scalar dissipation at this point (Figure 5.24) show similar behaviour to that seen in Figure 5.23. However, at 0.97 ms ASI, convection of the vapour jet upstream leads to large scalar gradients in the region around point (A) and local extinction of the flame occurs as highlighted by (B) and shown in Figure 5.25.

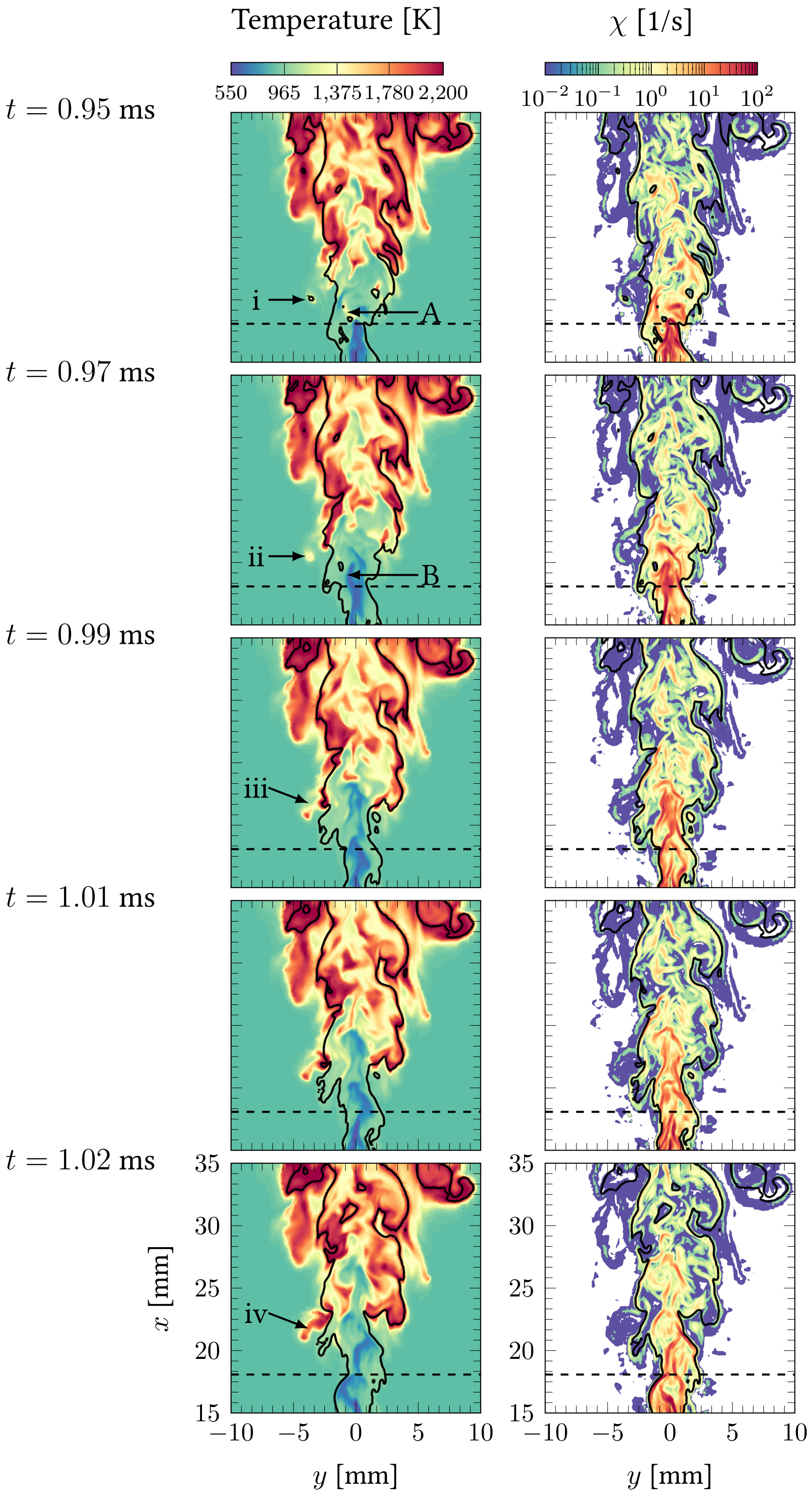

Figure 5.22: Temperature (left) and scalar dissipation (right) evolution near the flame lift-off length. The black dashed line marks the simulations flame lift-off length. The solid black line is the contour of stoichiometric mixture fraction.

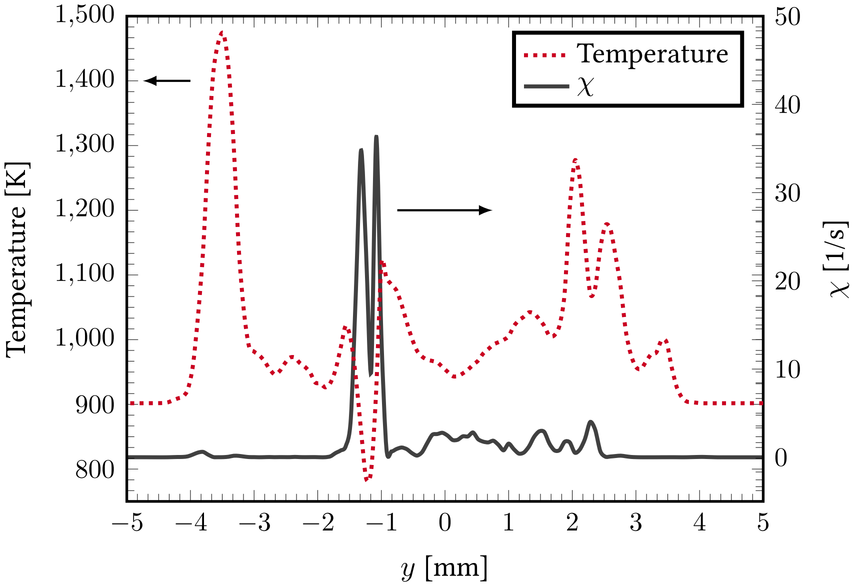

Figure 5.23: Radial scalar field distribution at 0.95 ms ASI at point (i) in Figure 5.22.

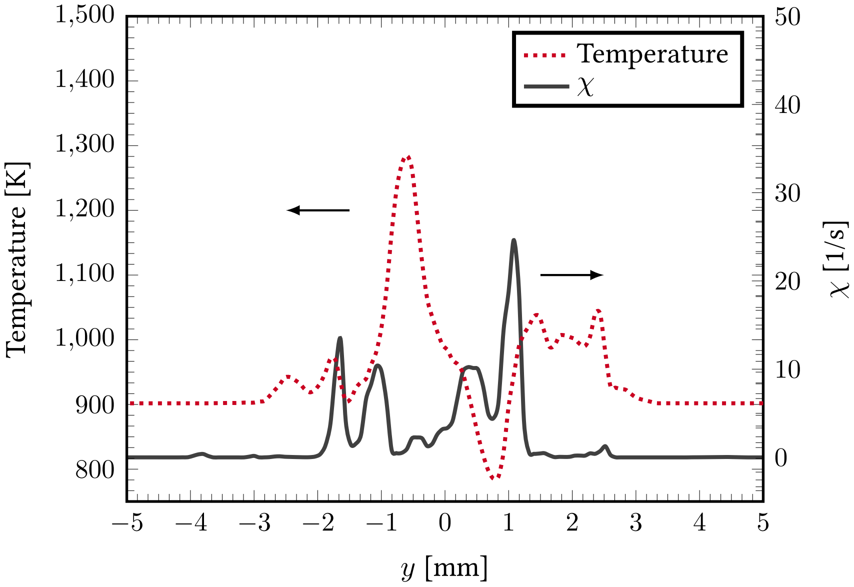

Figure 5.24: Radial scalar field distribution at 0.95 ms ASI at point (A) in Figure 5.22.

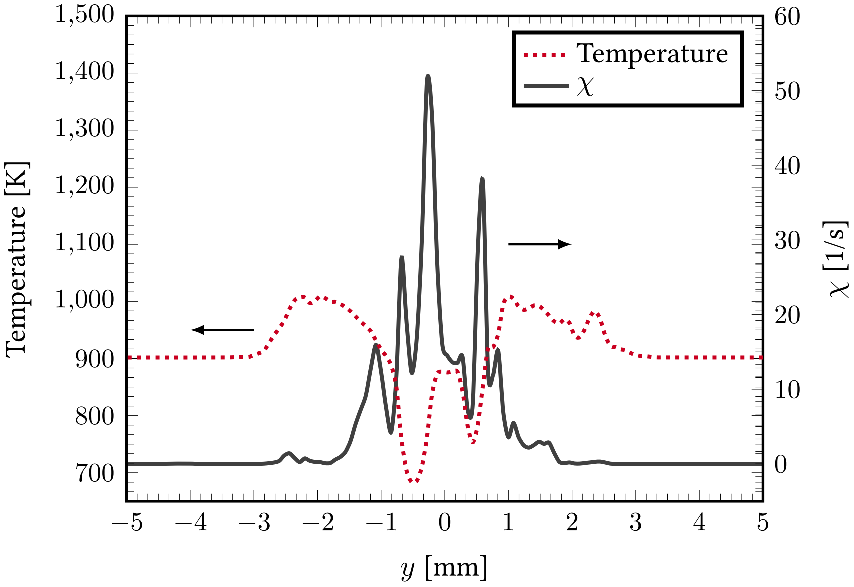

Figure 5.25: Radial scalar field distribution at 0.97 ms ASI at point (B) in Figure 5.22.

5.4 Parametric studies

5.4.1 RANS computational setup

The computational setup is identical to that presented in Section 5.2 with exception of the turbulence model. In the following RANS simulations, the standard $k - \epsilon$ model is used with adjusted model constant $C_{\epsilon 1 = 1.58}$. Combustion was modelled with the CSE-FGM combustion model as described previously, with additional equations solved for the mixture fraction (Equation 5.6), progress variable (Equation 5.5) and mixture fraction variance. In RANS, the mixture fraction variance is computed as:

$$\frac{\partial \bar{\rho} \widetilde{Z''^2}}{\partial t} + \frac{\partial \bar{\rho} \tilde{u}_j \widetilde{Z''^2}}{\partial x_j} = \frac{\partial}{\partial x_j} \left(\bar{\rho} \left(D + D_t \right) \frac{\partial \bar{\rho} \widetilde{Z''^2}}{\partial x_j} \right) + 2 \bar{\rho} \left(D_t \left(\frac{\partial \widetilde{Z}}{\partial x_j} \right)^2 - \widetilde{\chi} \right) \tag{5.14}$$

with $\widetilde{\chi}$ modelled as:

$$\widetilde{\chi} = c_x \frac{\tilde{\epsilon}}{\tilde{k}} \widetilde{Z''^2} \tag{5.15}$$

where c_x is a model constant and usually set as 2.0.

Flamelet libraries generated for each ambient temperature and oxygen concentration with the Luo mechanism. The tabulation parameters are identical to that outlined in Section 5.2.

The computational domain and grid refinement parameters are maintained from the LES setup (Figure 5.4). However, the grid size has been adjusted based on a grid dependence study which will be presented in the next section. In the following RANS simulations, the base grid is set as 2 mm with a minimum AMR and fixed embedding refinement of 0.25 mm. A section of the computational domain showing the RANS computational grid and grid refinement can be seen in Figure 5.26 and Figure 5.27.

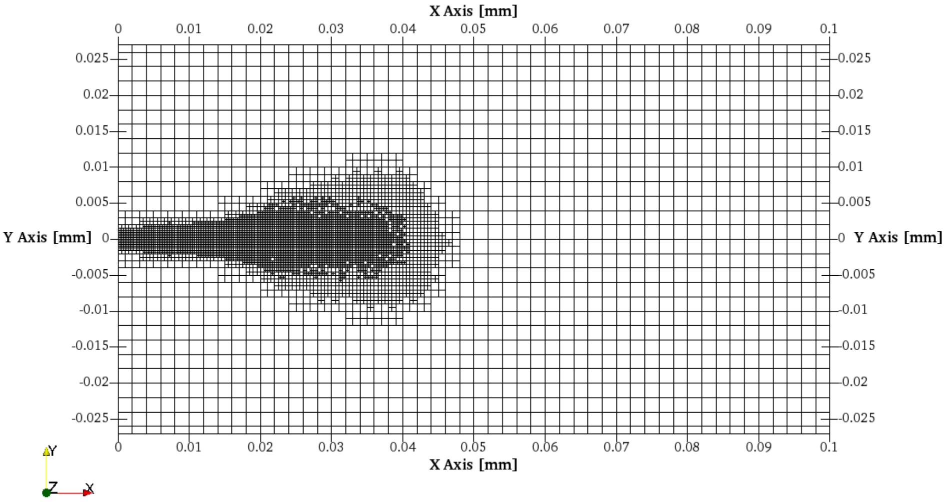

Figure 5.26: Spray computational domain X-Y plane clip showing RANS grid.

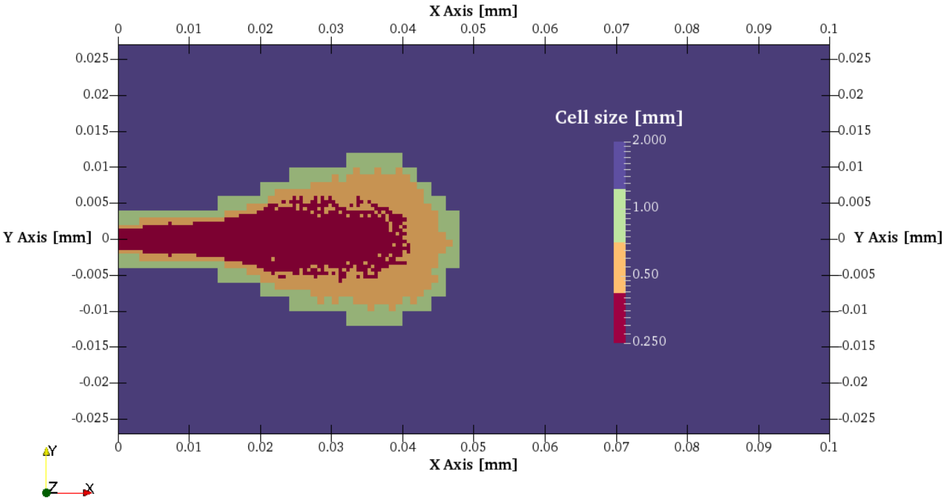

Figure 5.27: Spray computational domain X-Y plane clip showing RANS AMR and fixed embedding grid sizes.

RANS grid dependence

A grid dependence study of the RANS computational setup was conducted for the non-reacting spray condition by varying the minimum grid size from 1 mm down to 0.175 mm. An overview of the grid setup is shown in Table 5.8. Figure 5.28 presents the liquid penetration lengths for all grid sizes, where it is clear that results are relatively insensitive to grid sizes below 0.5 mm. Additionally, with exception of the 0.75 and 1 mm grids, simulation results compare well with experimental measurements over the injection duration. The vapour penetration shown in Figure 5.29 is more sensitive to grid size, where earlier in the injection durations grid sizes of 0.25 mm and below lead to an improved prediction of vapour length when compared to experimental measurements. Later into the injection event, vapour length predictions are insensitive to grid sizes below 0.5 mm with all simulation results falling within experimental measurements. Consequently, the 0.25 mm grid was chosen for all further RANS simulations as it provides a good balance between computational expense and accuracy compared to experimental measurements.

Table 5.8: Grid dependence parameters.

Grid	I	II	III	IV	V
Min cell size [mm]	1.0	0.75	0.5	0.25	0.175
Spray parcels*1000 [-]	50	75	100	200	300
Max cell number*1000 [-]	40	60	85	300	450
Runtime 16-cores [h]	0.1	0.15	0.2	0.35	1.5

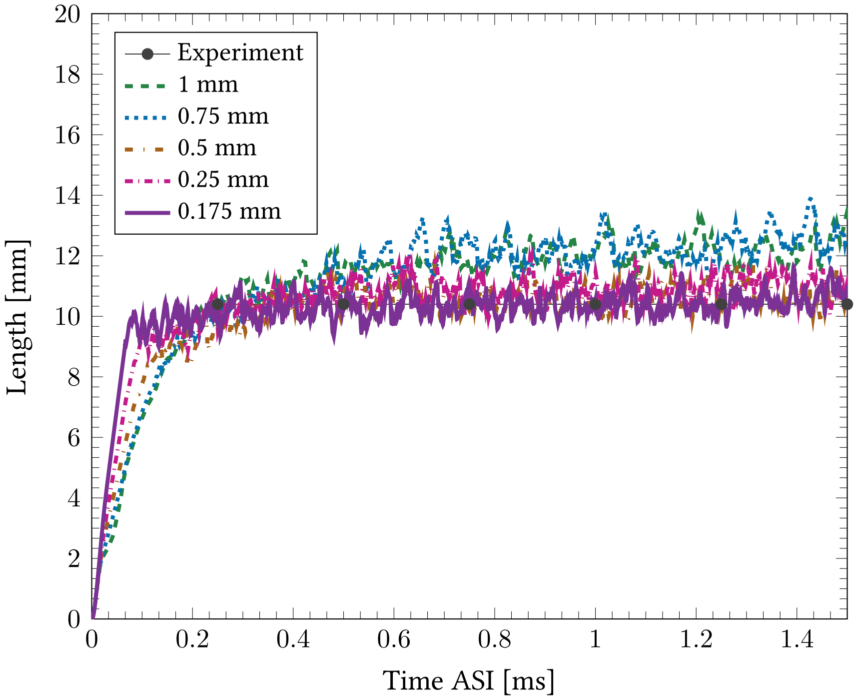

Figure 5.28: Liquid penetration length as a function of grid size. Liquid length is defined as the axial location of 97% liquid mass threshold. Experimental data repeated from [133].

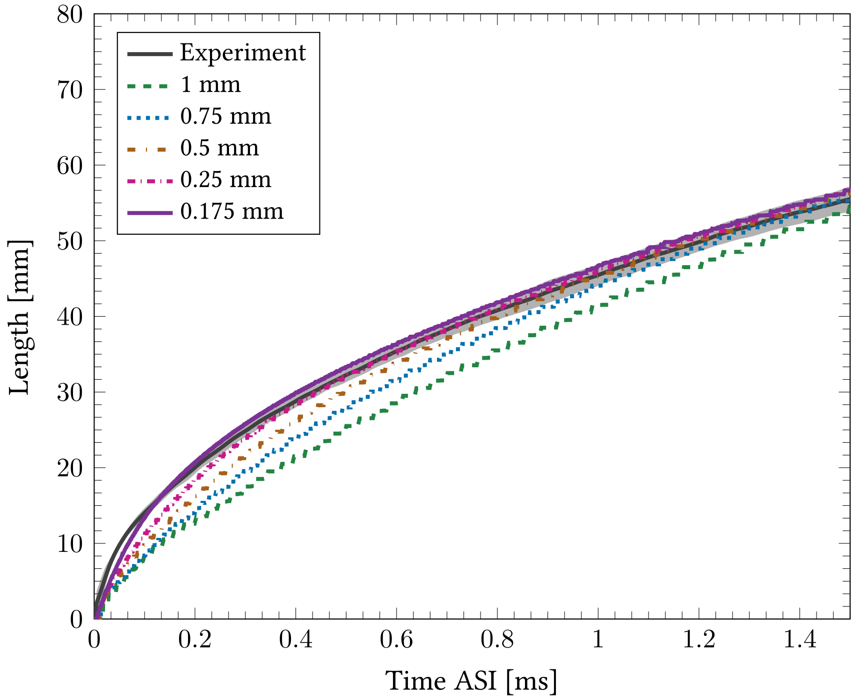

Figure 5.29: Simulation vapour penetration length as a function of grid size. Vapour length is defined as axial location of 1% vapour mass threshold. Shaded area represents experimental uncertainty. Experimental data repeated from [133].

5.4.2 Results and discussion

Non-reacting vaporising spray

Figure 5.30 shows the liquid and vapour lengths between simulation and experiment. The RANS predictions for both criteria are in excellent agreement with experimental measurements with exception of the first 0.2 ms ASI. Furthermore, the mixture fraction distribution as shown in Figure 5.31 is captured well by the RANS model. The LES results are also included and it can be seen that the RANS model is able to capture the mean mixture fraction profiles relatively well across all axial lengths with only a slight over-prediction along the centreline.

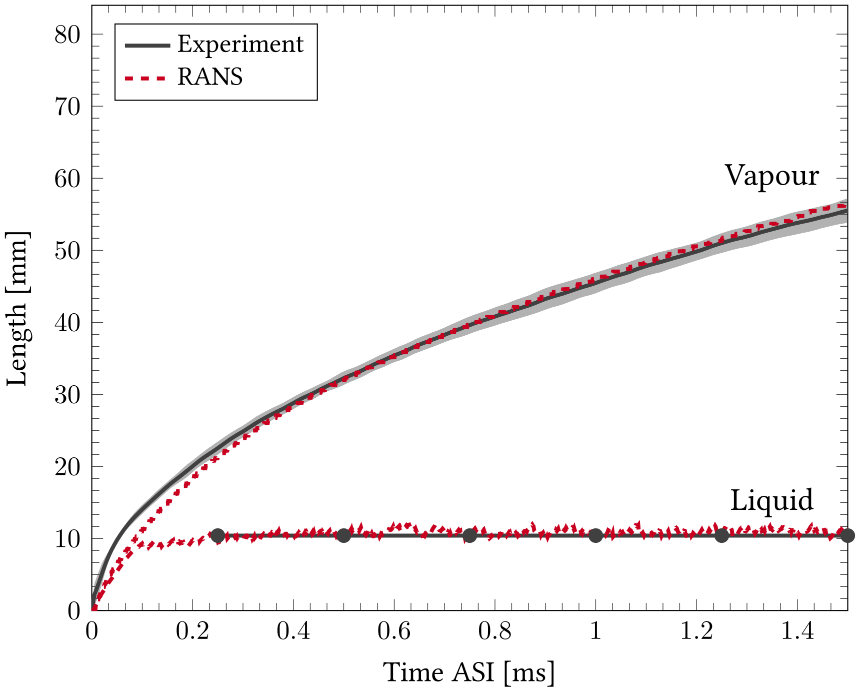

Figure 5.30: Experimental and simulation penetration lengths. Vapour length is defined as axial location of 1% vapour mass threshold. Liquid length is defined as the axial location of 99% liquid mass threshold. Shaded area represents experimental uncertainty.

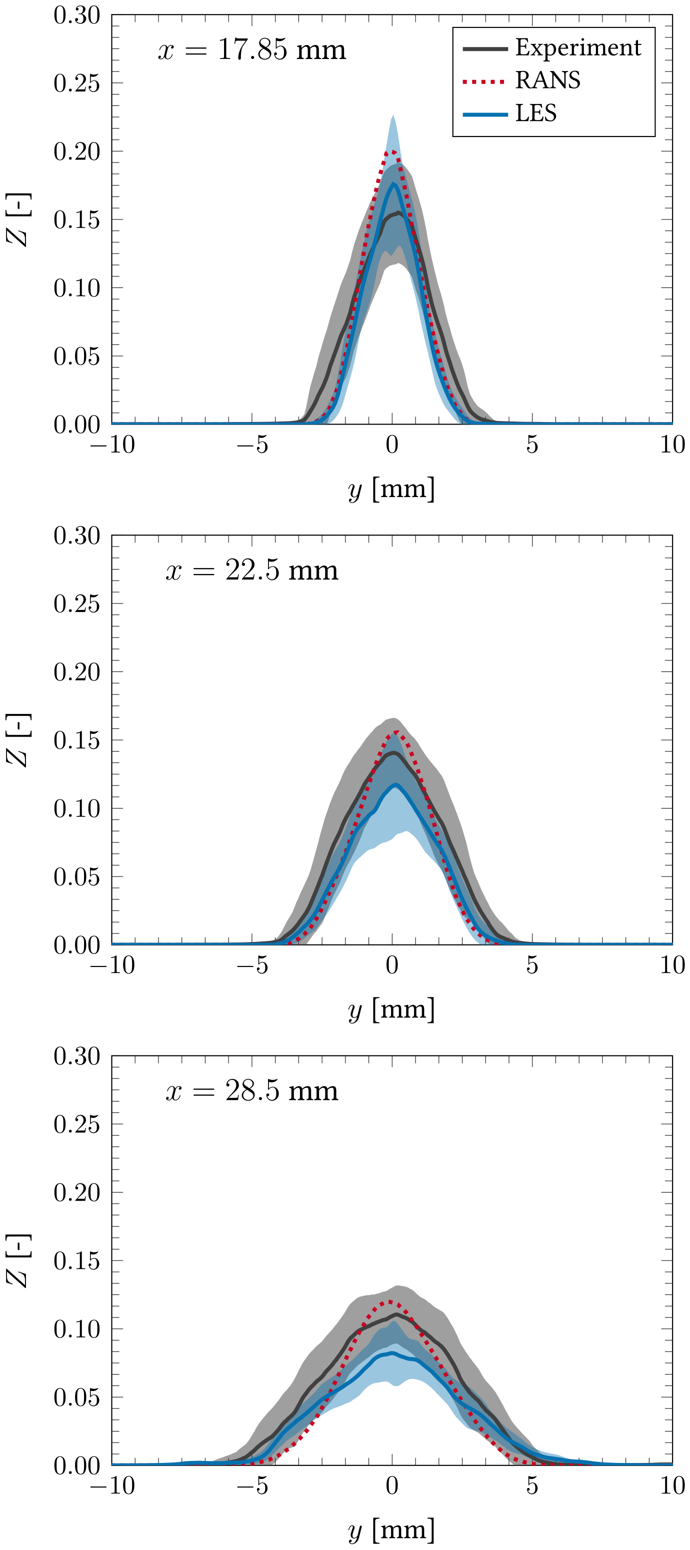

Figure 5.31: Radial profiles of mixture fraction for experiment and simulation at three axial positions. Shaded area represents experimental standard deviation. Experimental data repeated from [133].

Reacting spray

CSE-FGM/RANS simulations of conditions given in Table 5.1 are presented in this section. Figure 5.32 and Figure 5.33 show the comparison of experimental and simulation ignition delay timings and flame lift-off length across a range of ambient temperatures. Both ignition delay and flame lift-off length are predicted well by the CSE-FGM/RANS model at 900K and 1100K. The sensitivity with respect to ambient temperature is also captured accurately. Whilst the trends are captured across the entire temperature range, the model has difficulty in reproducing experimental measurements at 800 K. The effect of ambient oxygen concentration on ignition delay and flame lift-off are presented in Figure 5.34 and Figure 5.35. It can be seen that model over-predicts experimental ignition delay and flame lift-off length for the range of ambient oxygen concentrations. However, the model is able to capture the experimental trends and the sensitivity to changes in ambient oxygen composition are captured very well by the CSE-FGM/RANS combustion model. The discrepancy between predicted results and experimental measurements can be attributed to both the chemical mechanism and turbulent mixing. Pei *et al.*[173] found that the Luo mechanism tended to over-predict ignition delays when compared to shock tube experiments at 6 MPa. Additionally, a study by Meijer *et al.*[174] found that there could be trace concentrations of minor species of OH and NO present in the ECN combustion vessel before start of injection. Pei *et al.*[173] studied the effect of including these minor species into the ambient composition and found they improved the low temperature ignition delay predictions using the Luo mechanism. However, there was still an under-prediction at 800 K. Furthermore, the Luo mechanism has been found to over-predict both ignition delay and flame-lift off length in RANS simulations of ECN Spray A over a wide range of combustion models [151, 160, 175, 176, 177, 178]. As such, the influence of chemical mechanism will be investigated in Section 5.4.3 by applying the mechanism of Yao *et al.*[179] to Test I (800K, 15%O_2).

An additional source of deviation could also originate from the tabulation methodology, whereby a single unsteady flamelet of $a = 500$ s^{-1} is used to capture the ignition region. As explained previously in Section 5.2, ignition delay is insensitive for strain rates of $a =< 1000$ s^{-1} at ECN baseline conditions. However, at 800 K conditions (and high EGR rates), turbulent mixing plays a greater role due to the similar time scales of chemistry and flow, hence, strain rate has a more pronounced effect on ignition delay. It was shown by Ayyapurredi [138] that flame lift-off length was reduced when using manifolds generated with an ICDF at a strain rate of $a = 100$ s^{-1}, with further reductions being achieved by applying a strain rate of $a = 2$ s^{-1}. This suggests that a strain rate of $a = 500$ s^{-1} could be close to the ignition limit at 800 K resulting in the over-predictions of both flame lift-off and ignition delay time. Due to time limit constraints, generating chemistry manifolds with a reduced strain rate has not been studied here but will be recommended for future work.

Using LES has led to improved results with the Luo mechanism as is evidenced by results in Table 5.7 and previous studies [151, 161, 167]. The proposed reason for this improvement is the difference in computed scalar dissipation between LES and RANS. RANS predicts much higher scalar dissipation rates downstream of the nozzle compared to LES as shown in Figure 5.36. Considering ignition take place in low scalar dissipation rate regions and the Luo mechanism has a characteristically low quenching scalar dissipation rate [178] (when compared to other mechanisms) - the conditions leading to ignition, as well as flame stabilisation occur much further downstream of the injector in RANS.

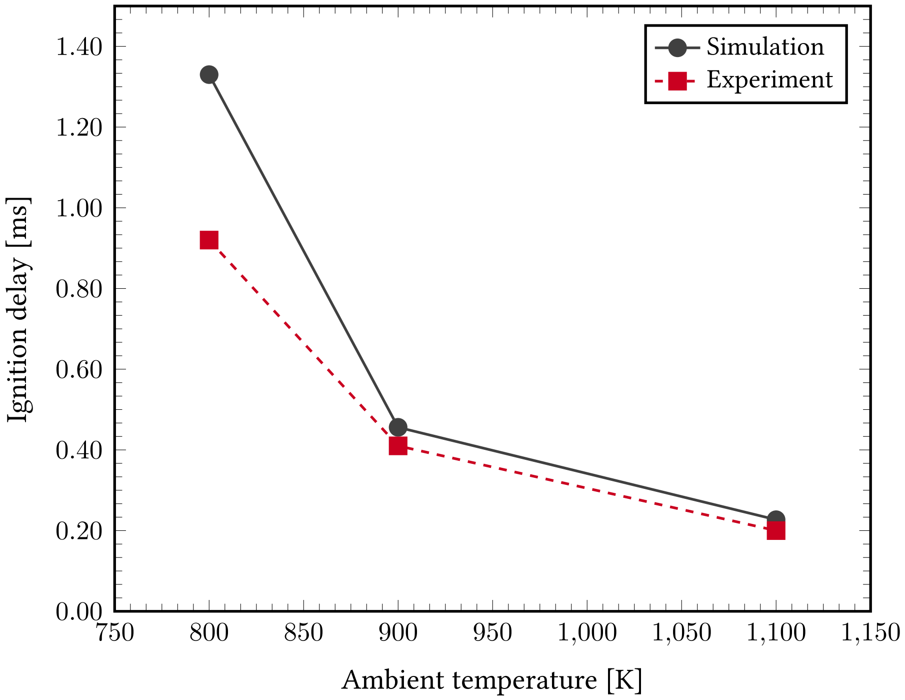

Figure 5.32: Simulation and experimental ignition delay timings for different ambient temperature conditions. Experimental measurements repeated from [133].

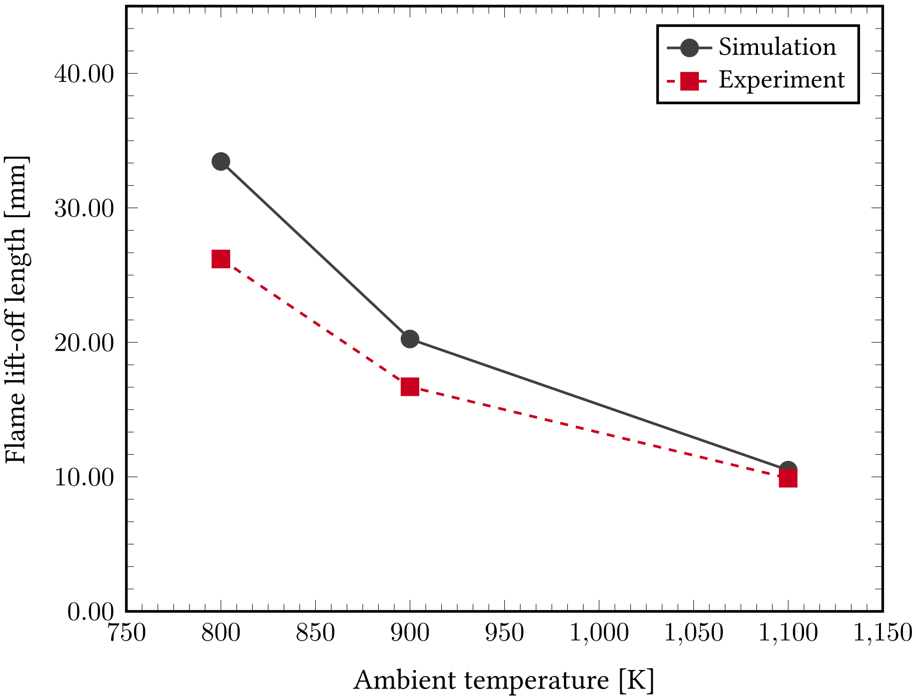

Figure 5.33: Simulation and experimental flame lift-off length for different ambient temperature conditions. Experimental measurements repeated from [133].

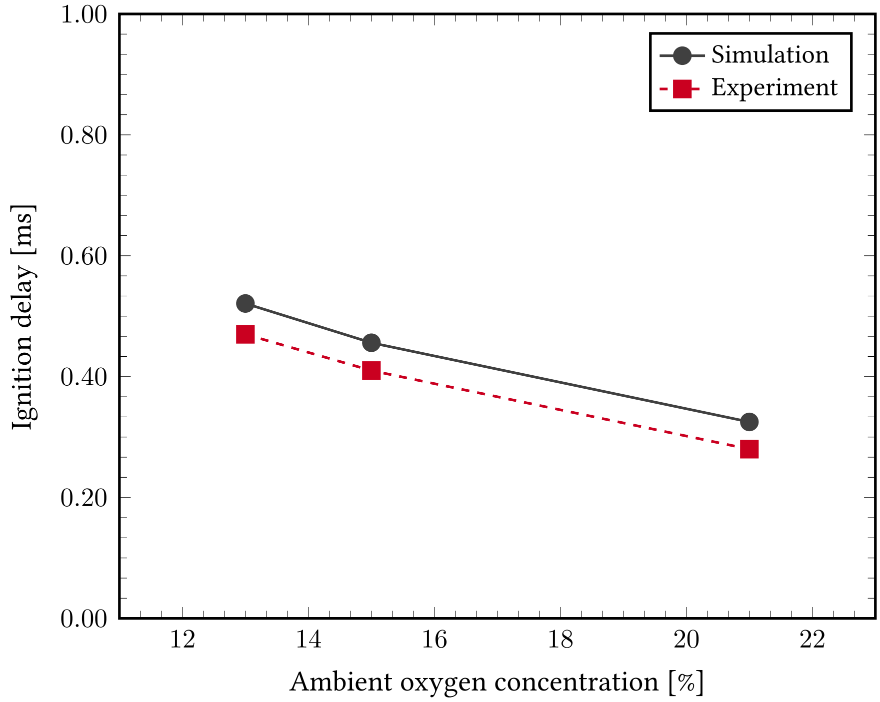

Figure 5.34: Simulation and experimental ignition delay timings for different ambient oxygen concentrations. Experimental measurements repeated from [133].

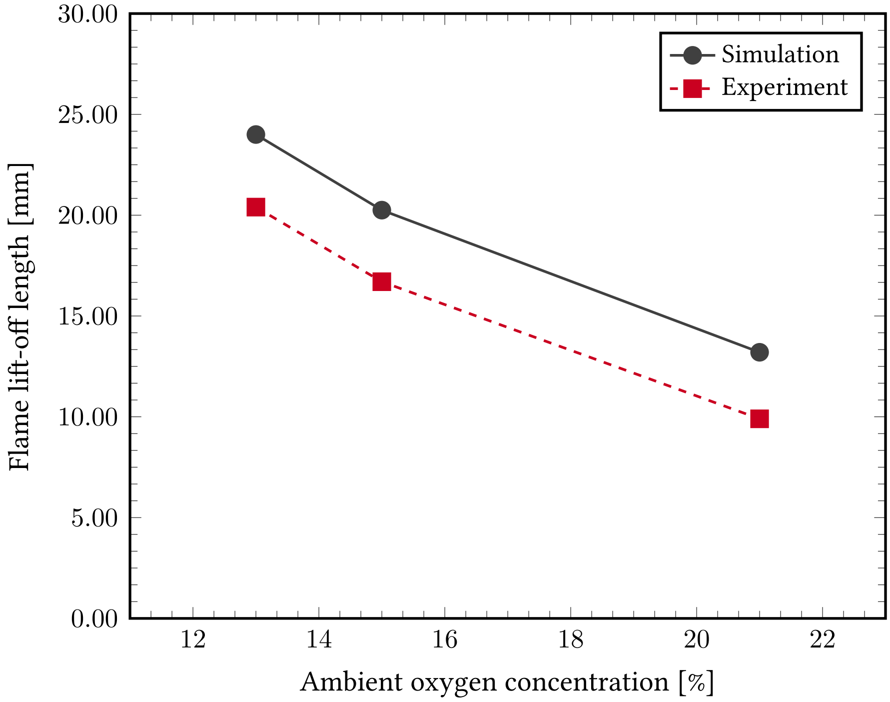

Figure 5.35: Simulation and experimental flame lift-off length for different ambient oxygen concentrations. Experimental measurements repeated from [133].

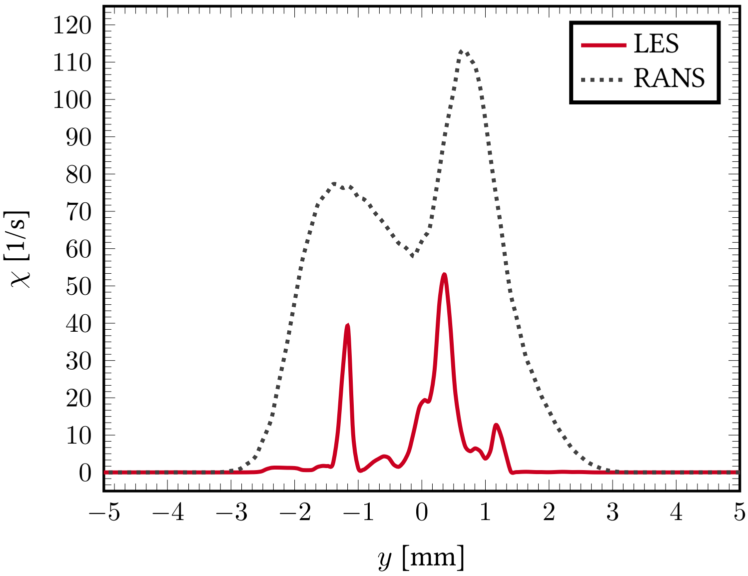

Figure 5.36: Radial scalar dissipation rate distribution near flame lift-off length ($x = 18$ mm) at 1.20 ms ASI for both turbulence models at ECN baseline conditions.

5.4.3 Effect of chemical mechanism

CSE-FGM/RANS simulations were repeated at the 800 K 15% O_2 condition using the skeletal mechanism of Yao *et al.*[179] containing 54 species and 269 reactions. This mechanism is considered a very reactive mechanism in comparison to the one of Luo and will highlight the sensitivity of ignition delay and flame lift-off length to underlying n-Dodecane chemistry. The Yao mechanism was derived from the semi-detailed mechanism of You *et al.*[180] containing 171 species and 1306 reactions. Multiple reduction methods were applied such as reaction flow analysis and isomer lumping with the final skeletal mechanism being validated over a wide range of conditions against shock-tube, perfectly stirred reactor and laminar flame speed experiments. Additionally, this mechanism was tuned against the detailed LLNL N-alkanes mechanism [181] and experimental ECN Spray A measurements for auto-ignition [133]. The RANS predictions are shown in Table 5.9, where improvements are seen for the Yao mechanism for both ignition delay and flame lift-off when compared to the Luo mechanism.

Table 5.9: Ignition delay time and flame lift-off length for both chemical mechanisms at 800 K 15% O_2 . Experimental data repeated from [133].

Test I (800 K, 15% O_2)	Experiment	Luo	Yao
Ignition delay time [ms]	0.92	1.33	1.12
Flame lift-off length [mm]	26.2	33.45	31.4

These improvements result from certain low and high temperature chemistry reactions being significantly enhanced in the Yao mechanism when compared to the Luo mechanism [182]. For low temperature chemistry, it was found that the Yao mechanism accumulates both HO_2 and CH_2O which are species used to track first-stage ignition. It was determined by Desantes *et al.*[183] that chemical activities were increased for reactions containing HCO. As HCO is a primary species in producing HO_2 and CH_2O, the increased activity of these reactions consequently led to increased formation of both first-stage ignition species. Furthermore, the high temperature ignition stage was also found to be promoted by the Yao mechanism as reactions relevant to H_2O_2

production were significantly enhanced with respect to other mechanisms [160, 183]. These enhancements are reflected in the generated chemistry manifolds which are shown in Figure 5.37 and Figure 5.38. The manifold for the Yao mechanism has a much higher source term for lower values of progress variable when compared to the Luo mechanism. Additionally, the Yao manifold is reactive over a wider range of mixture fractions.

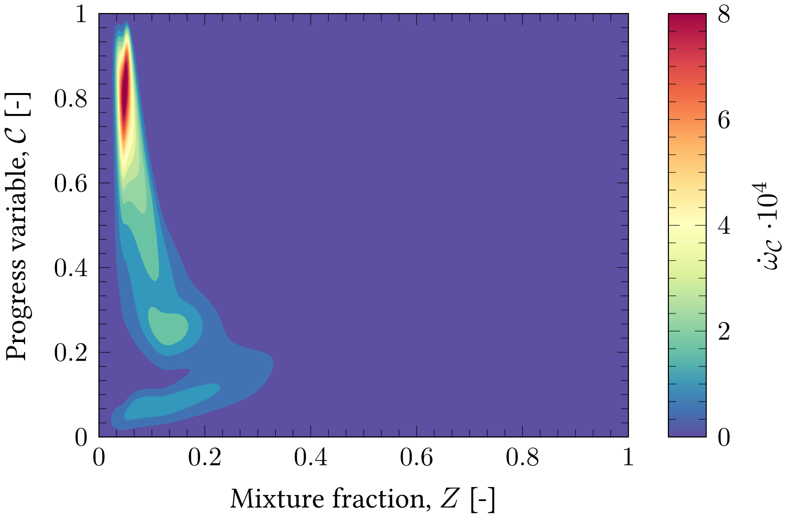

Figure 5.37: Flamelet generated manifold showing reaction rate of $\mathcal{C}$ as a function of mixture fraction and progress variable for the Luo mechanism.

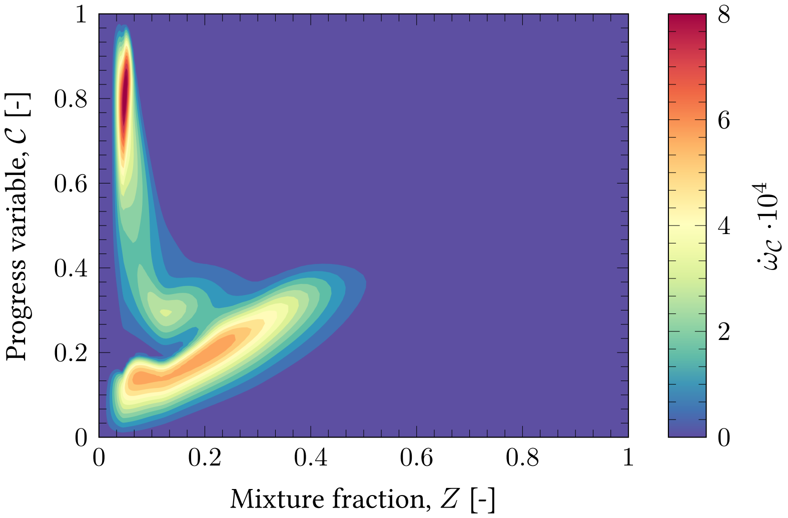

Figure 5.38: Flamelet generated manifold showing reaction rate of $\mathcal{C}$ as a function of mixture fraction and progress variable for the Yao mechanism.

5.5 Computational expense

The CSE-FGM/LES model was run locally on an Intel i7-5820K processor (2014). In order to make a comparison with available data in literature, the CSE-FGM/LES results shown in Table 5.10 have been scaled by 2.0 to account for the longer running time of the results of Blomberg *et al.*[184]. The results from Blomberg are with the Yao mechanism and is a split injection case run for 2.0 ms. As can be seen in Table 5.10, the CSE-FGM/LES model has a very low computational cost compared to the CMC-LES model. This is expected even with the higher cell count and larger chemistry mechanism used in this study, as only an additional three transport equations are being solved with the added expense of the integral inversion. In contrast, the CMC-LES model has to solve transport equations for all species (54). Furthermore, the computational framework used by Blomberg did not include the functionality of AMR which has been shown to greatly optimize run-time.

Table 5.10: CSE-FGM/LES computational cost.

	CSE-FGM/LES	CMC-LES
Min cell size [mm]	0.0875	0.125
Max cell number$\cdot 10^6$ [-]	2.6	1.9
Core-hours for 2 ms [-]	2230	10919

5.6 Summary

The CSE combustion model coupled with FGM chemistry reduction and tabulation was used to simulate the baseline condition of the n-Dodecane ECN Spray A flame. The mean reaction rate was computed based on integral inversion of a product-based progress variable and the presumed β-PDF. The combustion model was applied within an LES turbulence modelling framework and was first validated at non-reacting conditions where good predictions of velocity and mixture fraction field were achieved. The reacting baseline condition was then investigated with the CSE-FGM/LES model showing excellent agreement in predictions of ignition delay and flame lift-off length compared to experimental measurements. The CSE-FGM/LES model was able to predict the underlying physics of the two stage-ignition event of the n-Dodecane spray flame, where both low temperature cool flame propagation and high temperature ignition were observed. Qualitatively, the model was also able to predict the experimental OH distribution with characteristic features captured reasonably well. Furthermore, the auto-ignitive nature of flame stabilisation in high pressure fuel sprays was also predicted by the CSE-FGM/LES model.

Additionally, the model was applied within a RANS context to evaluate parametric variations in ambient temperature and oxygen concentration. The CSE-FGM/RANS model was able to accurately predict experimental trends and sensitivity to ambient conditions with exception of the 800 K test point. The discrepancies between predicted results and measurements were attributed to the chemical mechanism, turbulent mixing and tabulation methodology. RANS was found to predict high values of scalar dissipation rate downstream of the injector when compared to LES. Therefore, favourable conditions for flame stabilisation were pushed farther downstream in RANS when compared to LES which lead to over-predictions of flame lift-off length. As with previous studies, the chemical mechanism of Luo was found to over-predict both ignition delay and flame lift-off length over all test conditions. As such, the more reactive mechanism of Yao was applied to the 800 K test point where improvements were seen for both ignition delay and flame lift-off length. These were a direct result of the enhanced low and high temperature chemistry pathways in the Yao mechanism.

The CSE-FGM model has been successfully applied to simulate high pressure spray flames. The model was able to produce good quantitative and qualitative results over a wide range of conditions at a very modest computational cost. This demonstrates that the model is a good candidate to simulate high pressure spray flames with complex chemistry.

Chapter 6

Conclusions

Two objectives were set out at the beginning of this thesis. The first objective was to develop an understanding of the effects of certain parametric changes on combustion evolution and emissions formation in a single cylinder compression ignition engine. The investigation in Chapter 3 has allowed some insight into these effects, with the main outcomes detailed below:

- Variations in spray targeting, EGR rate and piston bowl geometry were shown to have noticeable impacts on the combustion event with simulation results predicting experimental trends across load points and EGR rates.
- It was shown that the effect of nozzle tip protrusion produced a greater change on combustion behaviour than piston bowl geometry. The effect of increasing the NTP value led to soot reductions at marginal increase in NO_x emissions. This was observed across all load points, EGR rates and both piston geometries. The deeper NTP increased air utilisation and led to improvements in mixing, leading to less fuel-rich regions which promote soot formation.
- The stepped-lip piston was found to reduce soot formation at an increase in NO_x emissions when compared to the standard re-entrant piston bowl. This was attributed to the piston-lip creating a recirculating region at the head of the fire-land which increased the residence time. As there was availability of both nitrogen, oxygen and high combustion temperatures - NO_x formation was promoted in this area.

- A significant finding was the increase in burn duration at all load points for the stepped-lip piston. This result was in contrast with existing literature which found stepped-lip pistons to reduced burn duration when compared to re-entrant piston geometries. This difference was found to be the effect of the shape of the lip, where in this investigation the piston-lip resembled a ‘true’ step, with near right angled change in height, as opposed to the more ramped shaped lip of investigations in literature. This sharp step geometry actively suppressed flame propagation into the fire-land and led to the flame being ’hold-up’ on the lip leading to an increase in burn duration.

- Finally, it was shown that current numerical tools are able to produce good results of global parameters and capture experimental trends. However, predictions of emissions is still a great challenge for combustion models based on simplified chemistry.

The second objective of this thesis was to extend a novel chemical source term closure to simulate diesel sprays with complex chemistry. This was addressed in Chapters 4 and 5, with the main outcomes detailed as follows:

- A state of the art combustion model, Conditional Source-term Estimation was successfully coupled with Flamelet Generated Manifold chemistry reduction and implemented into a commercial CFD code.

- The first application of the CSE-FGM model to simulate the Engine Combustion Network n-Dodecane Spray A was accomplished under a Large Eddy Simulation framework.

- The CSE-FGM/LES model was able to accurately predict ignition delay and flame lift-off length when compared to experimental measurements.

- The characteristic ignition behaviour of the ECN Spray A flame was captured with the model predicting the cool flame phenomenon and high temperature ignition event.

- The CSE-FGM/LES model qualitatively agreed well with experimental observations of the OH distribution and captured the auto-ignitive flame stabilisation mechanism of the ECN Spray A flame.
- The CSE-FGM model was then applied in a RANS framework to validate the model at different ambient temperatures and oxygen concentrations. The CSE-FGM/RANS model successfully predicted experimental trends and sensitivity with respect to ambient conditions.
- The implications of n-Dodecane chemical mechanism were studied, with the CSE-FGM model correctly reflecting the effect of enhanced underlying chemistry on ignition delay and flame lift-off length predictions.
- The CSE-FGM model has been demonstrated to successfully predict constant volume combustion of high pressure spray flames while accounting for turbulence-chemistry-interactions, allowing detailed chemical kinetics and maintaining a low computational cost.

6.1 Future work

Recommendations of future work are mainly based on continued development of the CSE-FGM model:

- The numerical sensitivities of the CSE inversion need to be studied more comprehensively and an understanding of the errors associated with regularisation need to be quantified.
- The current FGM is parametrised by progress variable and mixture fraction. Considering flow and chemistry are more strongly coupled at lower ambient temperatures and high EGR rates. A manifold should be constructed to include scalar dissipation rate as third dimension which should improve predictions at these conditions.
- Coupling of chemistry and flow is done through a product based progress variable. Whilst this approach has been used successfully, the selection of species used in the definition of progress variable will have impact on combustion predictions. A sensitivity study of the progress variable definition should be carried out to determine the most accurate with respect to combustion predictions.
- The current implementation of CSE-FGM can be coupled with more complex emissions models. As comprehensive experimental soot data is available from the Engine Combustion Network, the current model should be applied to these test cases to determine the CSE-FGM models ability in predicting these emissions.
- Finally, the CSE-FGM model should be applied to an engine case. This is possible but requires a manifold that contains additional dimensions of pressure and enthalpy which change considerably over an engine cycle.

References

[1] Detlev Mohr, N Müller, et al. "The road to 2020 and beyond: What's driving the global automotive industry". In: *McKinsey & Company* (2013).

[2] IEA. "CO2 Emissions from Fuel Combustion". In: *International Energy Agency, Paris* (2016).

[3] D Becker. "KPMG's Global Automotive Executive Survey 2015". In: *KPMG International, Stuttgart* (2015).

[4] Felix Leach, Riyaz Ismail, et al. "Comparing the Effect of Fuel/Air Interactions in a Modern High-Speed Light-Duty Diesel Engine". In: *SAE Technical Paper 2017-24-0075*. SAE International, Sept. 2017.

[5] Riyaz Ismail, Felix Leach, et al. "Computational investigation of the effects of piston geometry on the combustion evolution in a light duty HSDI engine". In: *ASME 2017 Internal Combustion Engine Division Fall Technical Conference ICEF2017-3588*. American Society of Mechanical Engineers. 2017.

[6] Felix Leach, Riyaz Ismail, et al. "Engine-out emissions from a modern high speed diesel engine – The importance of Nozzle Tip Protrusion". In: *Applied Energy* 226 (2018), pp. 340–352.

[7] Felix Leach, Riyaz Ismail, et al. "The effect of a stepped lip piston design on performance and emissions from a high-speed diesel engine". In: *Applied Energy* 215 (2018), pp. 679–689.

[8] XiaoHang Fang, Riyaz Ismail, et al. "Numerical Investigation of Combustion Recession on ECN Diesel Spray A". In: *ASME 2017 Internal Combustion Engine Division Fall Technical Conference ICEF2018-9597*. American Society of Mechanical Engineers. 2018.

[9] XiaoHang Fang, Riyaz Ismail, et al. "A Study on Kinetic Mechanisms of Diesel Fuel Surrogate n-Dodecane for the Simulation of Combustion Recession". In: *SAE Technical Paper 2019-01-0202*. SAE International, Jan. 2019.

[10] Denis Veynante and Luc Vervisch. "Turbulent combustion modeling". In: *Progress in Energy and Combustion Science* 28.3 (2002), pp. 193–266.

[11] Thierry Poinsot and Denis Veynante. *Theoretical and numerical combustion*. RT Edwards, Inc., 2005.

[12] Lars Davidson. *Fluid mechanics, Turbulent Flow and Turbulence Modeling*. Chalmers University of Technology, 2015.

[13] B.E. Launder and D.B. Spalding. “The numerical computation of turbulent flows”. In: *Computer Methods in Applied Mechanics and Engineering* 3.2 (1974), pp. 269–289.

[14] Zhiyu Han and Rolf D Reitz. “Turbulence modeling of internal combustion engines using RNG $k - \epsilon$ models”. In: *Combustion Science and Technology* 106.4-6 (1995), pp. 267–295.

[15] Victor Yakhot and Steven A Orszag. “Renormalization group analysis of turbulence. I. Basic theory”. In: *Journal of Scientific Computing* 1.1 (1986), pp. 3–51.

[16] Stephen B Pope. *Turbulent flows*. Cambridge University Press, 2000.

[17] S Leonard, M Terracol, et al. “Commutation error in LES with time-dependent filter width”. In: *Computers & Fluids* 36.3 (2007), pp. 513–519.

[18] DB Spalding. “Mixing and chemical reaction in steady confined turbulent flames”. In: *International Symposium on Combustion*. Vol. 13. 1. Elsevier. 1971, pp. 649–657.

[19] Bjørn F Magnussen and BW Hjertager. “On the structure of turbulence and a generalized eddy dissipation concept for chemical reaction in turbulent flow”. In: *19th AIAA Aerospace Meeting, St. Louis, USA*. 1981.

[20] S.B. Pope. “Computations of turbulent combustion: Progress and challenges”. In: *Symposium (International) on Combustion* 23.1 (1991). Twenty-Third Symposium (International) on Combustion, pp. 591–612.

[21] FA Williams. “Recent advances in theoretical descriptions of turbulent diffusion flames”. In: *Turbulent mixing in nonreactive and reactive flows*. Springer, 1975, pp. 189–208.

[22] N Peters and FA Williams. “Coherent structures in turbulent combustion”. In: *The Role of Coherent Structures in Modelling Turbulence and Mixing*. Springer, 1981, pp. 364–393.

[23] Norbert Peters. “Laminar diffusion flamelet models in non-premixed turbulent combustion”. In: *Progress in Energy and Combustion Science* 10.3 (1984), pp. 319–339.

[24] Sung King Liew, KNC Bray, et al. “A flamelet model of turbulent non-premixed combustion”. In: *Combustion Science and Technology* 27.1-2 (1981), pp. 69–73.

[25] Stephen B Pope. “Small scales, many species and the manifold challenges of turbulent combustion”. In: *Proceedings of the Combustion Institute* 34.1 (2013), pp. 1–31.

[26] B Cuenot and T Poinsot. “Effects of curvature and unsteadiness in diffusion flames. Implications for turbulent diffusion combustion”. In: *Symposium (International) on Combustion*. Vol. 25. 1. Elsevier. 1994, pp. 1383–1390.

[27] Bénédicte Cuenot. “The Flamelet Model for Non-Premixed Combustion”. In: *Turbulent Combustion Modeling*. Springer, 2011, pp. 43–61.

[28] H. Barths, C. Antoni, et al. "Three-Dimensional Simulation of Pollutant Formation in a DI Diesel Engine Using Multiple Interactive Flamelets". In: *SAE Technical Paper 982459*. SAE International, Oct. 1998.

[29] C Felsch, M Gauding, et al. "An extended flamelet model for multiple injections in DI Diesel engines". In: *Proceedings of the Combustion Institute* 32.2 (2009), pp. 2775–2783.

[30] J.A. Van Oijen and L.P.H. De Goey. "Modelling of Premixed Laminar Flames using Flamelet-Generated Manifolds". In: *Combustion Science and Technology* 161.1 (2000), pp. 113–137.

[31] Jeroen Adrianus van Oijen. *Flamelet-generated manifolds: development and application to premixed laminar flames*. Eindhoven University of Technology, 2002.

[32] Frank E Marble and James E Broadwell. *The coherent flame model for turbulent chemical reactions*. Tech. rep. Defense Technical Information Center, 1977.

[33] O Colin, A Benkenida, et al. "3D modeling of mixing, ignition and combustion phenomena in highly stratified gasoline engines". In: *Oil & Gas Science and Technology* 58.1 (2003), pp. 47–62.

[34] O Colin and A Benkenida. "The 3-zones extended coherent flame model (ECFM3Z) for computing premixed/diffusion combustion". In: *Oil & Gas Science and Technology* 59.6 (2004), pp. 593–609.

[35] Olivier Colin, António Pires da Cruz, et al. "Detailed chemistry-based auto-ignition model including low temperature phenomena applied to 3-D engine calculations". In: *Proceedings of the Combustion Institute* 30.2 (2005), pp. 2649–2656.

[36] G. Subramanian, L. Vervisch, et al. "New Developments in Turbulent Combustion Modeling for Engine Design: ECFM-CLEH Combustion Submodel". In: *SAE Technical Paper 2007-01-0154*. SAE International, Apr. 2007.

[37] Roland Borghi. "Turbulent combustion modelling". In: *Progress in Energy and Combustion Science* 14.4 (1988), pp. 245–292.

[38] Fengshan Liu, Hongsheng Guo, et al. "A robust and accurate algorithm of the β-pdf integration and its application to turbulent methane–air diffusion combustion in a gas turbine combustor simulator". In: *International journal of Thermal Sciences* 41.8 (2002), pp. 763–772.

[39] SS Girimaji. "Assumed β-pdf model for turbulent mixing: Validation and extension to multiple scalar mixing". In: *Combustion Science and Technology* 78.4-6 (1991), pp. 177–196.

[40] R.W. Bilger, S.H. Starner, et al. "On reduced mechanisms for methanee5f8air combustion in nonpremixed flames". In: *Combustion and Flame* 80.2 (1990), pp. 135–149.

[41] S.B. Pope. "The probability approach to the modelling of turbulent reacting flows". In: *Combustion and Flame* 27 (1976), pp. 299–312.

[42] S.B. Pope. “PDF methods for turbulent reactive flows”. In: *Progress in Energy and Combustion Science* 11.2 (1985), pp. 119–192.

[43] Zhuyin Ren and Stephen B. Pope. “An investigation of the performance of turbulent mixing models”. In: *Combustion and Flame* 136.1 (2004), pp. 208–216.

[44] Stephen B Pope. “A Monte Carlo Method for the PDF Equations of Turbulent Reactive Flow”. In: *Combustion Science and Technology* 25.5-6 (1981), pp. 159–174.

[45] D.C. Haworth. “Progress in probability density function methods for turbulent reacting flows”. In: *Progress in Energy and Combustion Science* 36.2 (2010), pp. 168–259.

[46] A Yu Klimenko. “Multicomponent diffusion of various admixtures in turbulent flow”. In: *Fluid dynamics* 25.3 (1990), pp. 327–334.

[47] R. W. Bilger. “Conditional moment closure for turbulent reacting flow”. In: *Physics of Fluids A: Fluid Dynamics* 5.2 (1993), pp. 436–444.

[48] AR Masri, RW Dibble, et al. “The structure of turbulent nonpremixed flames of methanol over a range of mixing rates”. In: *Combustion and Flame* 89.2 (1992), pp. 167–185.

[49] Jonathan H Frank, Sebastian A Kaiser, et al. “Reaction-rate, mixture-fraction, and temperature imaging in turbulent methane/air jet flames”. In: *Proceedings of the Combustion Institute* 29.2 (2002), pp. 2687–2694.

[50] A Yu Klimenko and Robert William Bilger. “Conditional moment closure for turbulent combustion”. In: *Progress in Energy and Combustion science* 25.6 (1999), pp. 595–687.

[51] W. Kendal Bushe and Helfried Steiner. “Conditional moment closure for large eddy simulation of nonpremixed turbulent reacting flows”. In: *Physics of Fluids* 11.7 (1999), pp. 1896–1906.

[52] Chong M. Cha, George Kosály, et al. “Modeling extinction and reignition in turbulent nonpremixed combustion using a doubly-conditional moment closure approach”. In: *Physics of Fluids* 13.12 (2001), pp. 3824–3834.

[53] Seung Hyun Kim and Kang Y. Huh. “Second-order conditional moment closure modeling of turbulent piloted Jet diffusion flames”. In: *Combustion and Flame* 138.4 (2004), pp. 336–352.

[54] G De Paola, IS Kim, et al. “Second-order conditional moment closure simulations of autoignition of an n-heptane plume in a turbulent coflow of heated air”. In: *Flow, Turbulence and Combustion* 82.4 (2009), pp. 455–475.

[55] E. Mastorakos and R. W. Bilger. “Second-order conditional moment closure for the autoignition of turbulent flows”. In: *Physics of Fluids* 10.6 (1998), pp. 1246–1248.

[56] G De Paola, E Mastorakos, et al. “Diesel engine simulations with multi-dimensional conditional moment closure”. In: *Combustion Science and Technology* 180.5 (2008), pp. 883–899.

[57] Giulio Borghesi, Epaminondas Mastorakos, et al. “Modeling evaporation effects in conditional moment closure for spray autoignition”. In: *Combustion Theory and Modelling* 15.5 (2011), pp. 725–752.

[58] Michele Bolla, Daniele Farrace, et al. “Influence of turbulence–chemistry interaction for n-heptane spray combustion under diesel engine conditions with emphasis on soot formation and oxidation”. In: *Combustion Theory and Modelling* 18.2 (2014), pp. 330–360.

[59] Michele Bolla, Daniele Farrace, et al. “Modelling of soot formation in a heavy-duty diesel engine with conditional moment closure”. In: *Fuel* 117 (2014), pp. 309–325.

[60] ES Richardson and E Mastorakos. “Conditional moment closure modelling for spark ignition in a turbulent n-heptane spray”. In: *Proceedings of the Mediterranean Combustion Symposium*. Vol. 5. 2007.

[61] YM Wright, K Boulouchos, et al. *Multi-dimensional conditional moment closure modelling applied to a heavy-duty common-rail diesel engine*. Tech. rep. SAE Technical Paper, 2009.

[62] IS Kim and E Mastorakos. “Simulations of turbulent lifted jet flames with two-dimensional conditional moment closure”. In: *Proceedings of the Combustion Institute* 30.1 (2005), pp. 911–918.

[63] G Kim, S Kang, et al. “Conditional moment closure and transient flamelet modelling for detailed structure and NO x formation characteristics of turbulent nonpremixed jet and recirculating flames”. In: *Combustion Theory and Modelling* 11.4 (2007), pp. 527–552.

[64] W Kendal Bushe and Helfried Steiner. “Conditional moment closure for large eddy simulation of nonpremixed turbulent reacting flows”. In: *Physics of Fluids* 11.7 (1999), pp. 1896–1906.

[65] Anthony A Amsden, PJ O’rourke, et al. *KIVA-II: A computer program for chemically reactive flows with sprays*. Tech. rep. Los Alamos National Lab., NM (USA), 1989.

[66] G.M. Faeth. “Current status of droplet and liquid combustion”. In: *Energy and Combustion Science*. Ed. by N.A. Chigier. Pergamon, 1979, pp. 149–182.

[67] Paul C Miles and Öivind Andersson. “A review of design considerations for light-duty diesel combustion systems”. In: *International Journal of Engine Research* 17.1 (2016), pp. 6–15.

[68] Su Han Park, Hyung Jun Kim, et al. “Effect of multiple injection strategies on combustion and emission characteristics in a diesel engine”. In: *Energy & Fuels* 30.2 (2016), pp. 810–818.

[69] Jacqueline O’Connor and Mark Musculus. “Post Injections for Soot Reduction in Diesel Engines: A Review of Current Understanding”. In: *SAE Int. J. Engines* 6 (Apr. 2013), pp. 400–421.

[70] M. Badami, F. Mallamo, et al. “Influence of Multiple Injection Strategies on Emissions, Combustion Noise and BSFC of a DI Common Rail Diesel Engine”. In: *SAE Technical Paper 2002-01-0503*. SAE International, Mar. 2002.

[71] Eric M. Kurtz and Joshua Styron. “An Assessment of Two Piston Bowl Concepts in a Medium-Duty Diesel Engine”. In: *SAE Int. J. Engines* 5 (Apr. 2012), pp. 344–352.

[72] Joshua Styron, Brian Baldwin, et al. “Ford 2011 6.7L Power Stroke® Diesel Engine Combustion System Development”. In: *SAE Technical Paper 2011-01-0415*. SAE International, Apr. 2011.

[73] S Busch, F Perini, et al. “Light-Duty Diesel Combustion”. In: (2016).

[74] Jessica Dahlstrom, Oivind Andersson, et al. “Experimental Comparison of Heat Losses in Stepped-Bowl and Re-Entrant Combustion Chambers in a Light Duty Diesel Engine”. In: *SAE Technical Paper 2016-01-0732*. SAE International, Apr. 2016.

[75] Jonathan George Dolak, Yu Shi, et al. “A Computational Investigation of Stepped-Bowl Piston Geometry for a Light Duty Engine Operating at Low Load”. In: *SAE Technical Paper 2010-01-1263*. SAE International, Apr. 2010.

[76] Stephen Chittick, Mark Swindell, et al. “Analytical and Developmental Techniques Utilized in the Structural Optimization of a New Lightweight Diesel Engine”. In: *SAE International Journal of Engines* 8.4 (2015), pp. 1960–1966.

[77] N Papaioannou. “Thermal Investigations on a High-Speed Direct Injection Diesel Engine”. PhD thesis. University of Oxford, 2018.

[78] K Richards, P Senecal, et al. “CONVERGE (2.4)”. In: *Convergent Science, Inc., Middleton, WI* (2013).

[79] R.I Issa. “Solution of the implicitly discretised fluid flow equations by operator-splitting”. In: *Journal of Computational Physics* 62.1 (1986), pp. 40–65.

[80] CM Rhie and W Li Chow. “Numerical study of the turbulent flow past an airfoil with trailing edge separation”. In: *AIAA journal* 21.11 (1983), pp. 1525–1532.

[81] V Golovichev. “Mechanisms: Combustion Chemistry”. In: *Chalmers University of Technology, http://www. tfd. chalmers. se/~ valeri/MECH. html* (2000).

[82] Julien Bohbot, Olivier Colin, et al. “An Innovative Approach Combining Adaptive Mesh Refinement, the ECFM3Z Turbulent Combustion Model, and the TKI Tabulated Auto-Ignition Model for Diesel Engine CFD Simulations”. In: *SAE Technical Paper 2016-01-0604*. SAE International, Apr. 2016.

[83] P. K. Senecal, E. Pomraning, et al. “Multi-Dimensional Modeling of Direct-Injection Diesel Spray Liquid Length and Flame Lift-off Length using CFD and Parallel Detailed Chemistry”. In: *SAE Technical Paper 2003-01-1043*. SAE International, Mar. 2003.

[84] Zhiyu Han and Rolf D Reitz. “A temperature wall function formulation for variable-density turbulent flows with application to engine convective heat

transfer modeling”. In: *International Journal of Heat and Mass Transfer* 40.3 (1997), pp. 613–625.

[85] Rolf D. Reitz and R. Diwakar. “Structure of High-Pressure Fuel Sprays”. In: *SAE Technical Paper 870598*. SAE International, Feb. 1987.

[86] Jennifer C Beale and Rolf D Reitz. “Modeling spray atomization with the Kelvin-Helmholtz/Rayleigh-Taylor hybrid model”. In: *Atomization and Sprays* 9.6 (1999).

[87] Rolf D Reitz and FV Bracco. “Mechanisms of breakup of round liquid jets”. In: *Encyclopedia of Fluid Mechanics* 3 (1986), pp. 233–249.

[88] Peter J O’Rourke and Anthony A Amsden. *The TAB method for numerical calculation of spray droplet breakup*. Tech. rep. Los Alamos National Lab., NM (USA), 1987.

[89] Alex B Liu, Daniel Mather, et al. *Modeling the effects of drop drag and breakup on fuel sprays*. Tech. rep. Defense Technical Information Center, 1993.

[90] David P Schmidt and CJ Rutland. “A new droplet collision algorithm”. In: *Journal of Computational Physics* 164.1 (2000), pp. 62–80.

[91] Dominik Kuhnke. *Spray/wall interaction modelling by dimensionless data analysis*. Shaker, 2004.

[92] John Heywood. *Internal combustion engine fundamentals*. McGraw-Hill Education, 1988.

[93] K Richards, P Senecal, et al. “CONVERGE 2.4 Manual”. In: *Convergent Science, Inc., Madison, WI* (2017).

[94] H. Hiroyasu and T. Kadota. “Models for Combustion and Formation of Nitric Oxide and Soot in Direct Injection Diesel Engines”. In: *SAE Technical Paper 760129*. SAE International, Feb. 1976.

[95] J Nagle and RF Strickland-Constable. “Oxidation of Carbon between 1000-2000 C”. In: *Proceedings of The Fifth Carbon Conference*. Vol. 1. 1. Pergamon Press London. 1962, p. 154.

[96] Mike Bergin, Ettore Musu, et al. “Examination of initialization and geometric details on the results of CFD simulations of diesel engines”. In: *ASME 2009 Internal Combustion Engine Division Spring Technical Conference*. American Society of Mechanical Engineers. 2009, pp. 541–553.

[97] KW Bedford and WK Yeo. “Conjunctive filtering procedures in surface water flow and transport”. In: *Large eddy simulation of complex engineering and geophysical flows* (2010), pp. 513–537.

[98] Eric Pomraning. “Development of large eddy simulation turbulence models”. PhD thesis. University of Wisconsin–Madison, 2000.

[99] William M. Silvis. “An Algorithm for Calculating the Air/Fuel Ratio from Exhaust Emissions”. In: *International Congress Exposition*. SAE International 970514, 1997.

[100] XLJ Seykens, LMT Somers, et al. “Modelling of common rail fuel injection system and influence of fluid properties on injection process”. In: *Proceedings of VAFSEP* (2004), pp. 6–9.

[101] PK Senecal, E Pomraning, et al. “Grid-convergent spray models for internal combustion engine computational fluid dynamics simulations”. In: *Journal of Energy Resources Technology* 136.1 (2014), p. 012204.

[102] Janardhan Kodavasal, Christopher P Kolodziej, et al. “Computational fluid dynamics simulation of gasoline compression ignition”. In: *Journal of Energy Resources Technology* 137.3 (2015), p. 032212.

[103] Keita Arato and Teruyuki Takashima. “A Study on Reduction of Heat Loss by Optimizing Combustion Chamber Shape”. In: *SAE International Journal of Engines 2015-01-0786* 8.2 (2015), pp. 596–608.

[104] C. Angelberger, T. Poinsot, et al. “Improving Near-Wall Combustion and Wall Heat Transfer Modeling in SI Engine Computations”. In: *International Fuels Lubricants Meeting Exposition.* SAE International 972881, 1997.

[105] Ahmed Abdul Moiz. “Low temperature split injection spray combustion: ignition, flame stabilization and soot formation characteristics in diesel engine conditions”. PhD thesis. Michigan Technological University, 2016.

[106] Jacques Hadamard. *Lectures on Cauchy’s problem in linear partial differential equations.* Yale University Press, 1923.

[107] Per Christian Hansen. “Truncated singular value decomposition solutions to discrete ill-posed problems with ill-determined numerical rank”. In: *SIAM Journal on Scientific and Statistical Computing* 11.3 (1990), pp. 503–518.

[108] AN TIKHONOV. “Solution of incorrectly formulated problems and the regularization methods”. In: *Soviet Mathematics Doklady.* Vol. 4. 1963, pp. 1035–1038.

[109] J.W. Labahn and C.B. Devaud. “Investigation of conditional source-term estimation applied to a non-premixed turbulent flame”. In: *Combustion Theory and Modelling* 17.5 (2013), pp. 960–982.

[110] Daniele Dovizio, Jeffrey W. Labahn, et al. “Doubly Conditional Source-term Estimation (DCSE) applied to a series of lifted turbulent jet flames in cold air”. In: *Combustion and Flame* 162.5 (2015), pp. 1976–1986.

[111] M. Wang, J. Huang, et al. “Simulation of a turbulent non-premixed flame using conditional source-term estimation with trajectory generated low-dimensional manifold”. In: *Proceedings of the Combustion Institute* 31.2 (2007), pp. 1701–1709.

[112] M. M. Salehi, W. K. Bushe, et al. “Application of the conditional source-term estimation model for turbulence–chemistry interactions in a premixed flame”. In: *Combustion Theory and Modelling* 16.2 (2012), pp. 301–320.

[113] Lee, Seung Hi. “Numerical Investigation on Turbulent Non-premixed Methanol Flames Using Conditional Source-term Estimation”. MA thesis. 2015.

[114] RW Grout, W Kendal Bushe, et al. “Predicting the ignition delay of turbulent methane jets using conditional source-term estimation”. In: *Combustion Theory and Modelling* 11.6 (2007), pp. 1009–1028.

[115] Per Christian Hansen. “The L-curve and its use in the numerical treatment of inverse problems”. In: (1999).

[116] Mohammad Mahdi Salehi. “Numerical simulation of turbulent premixed flames with conditional source-term estimation”. PhD thesis. University of British Columbia, 2012.

[117] Max Bodenstein. “Eine theorie der photochemischen reaktionsgeschwindigkeiten”. In: *Zeitschrift für physikalische Chemie* 85.1 (1913), pp. 329–397.

[118] MD Smooke. “Reduced Kinetic Mechanisms and Asymptotic Approximations for Methane-Air Flames”. In: *Lecture Note in Physics* 384 (1991).

[119] Jürgen Warnatz, Ulrich Maas, et al. *Combustion*. Vol. 3. Springer, 1996.

[120] Norbert Peters and Bernd Rogg. *Reduced kinetic mechanisms for applications in combustion systems*. Vol. 15. Springer Science & Business Media, 2008.

[121] U. Maas and S.B. Pope. “Simplifying chemical kinetics: Intrinsic low-dimensional manifolds in composition space”. In: *Combustion and Flame* 88.3 (1992), pp. 239–264.

[122] Terese Løvås. “Model reduction techniques for chemical mechanisms”. In: *Chemical Kinetics*. InTech, 2012.

[123] SB Pope and U Maas. “Simplifying chemical kinetics: Trajectory-generated low-dimensional manifolds”. In: *Mechanical and Aerospace Engineering Report: FDA* 11 (1993).

[124] J. Huang and W. K. Bushe. “Simulation of transient turbulent methane jet ignition and combustion under engine-relevant conditions using conditional source-term estimation with detailed chemistry”. In: *Combustion Theory and Modelling* 11.6 (2007), pp. 977–1008.

[125] Seunghi Lee and Cecile Devaud. “Application of Conditional Source-term Estimation to two turbulent non-premixed methanol flames”. In: *Combustion Theory and Modelling* 20.5 (2016), pp. 765–797.

[126] Nasim Shahbazian, M. Mahdi Salehi, et al. “Performance of conditional source-term estimation model for LES of turbulent premixed flames in thin reaction zones regime”. In: *Proceedings of the Combustion Institute* 35.2 (2015), pp. 1367–1375.

[127] Stefanie Asenbauer. “Examining Spray Models for Conditional Source-term Estimation Combustion Simulation”. PhD thesis. University of Stuttgart, 2015.

[128] Olivier Gicquel, Nasser Darabiha, et al. “Liminar premixed hydrogen/air counterflow flame simulations using flame prolongation of ILDM with differential diffusion”. In: *Proceedings of the Combustion Institute* 28.2 (2000), pp. 1901–1908.

[129] G. Stahl and J. Warnatz. "Numerical investigation of time-dependent properties and extinction of strained methanee5f8 and propane-air flamelets". In: *Combustion and Flame* 85.3 (1991), pp. 285–299.

[130] Chem1D. "A one-dimensional laminar flame code, Eindhoven University of Technology". In: *URL http://www. combustion. tue. nl/chem1d* (2018).

[131] Cemil Bekdemir, Bart Somers, et al. "DNS with detailed and tabulated chemistry of engine relevant igniting systems". In: *Combustion and Flame* 161.1 (2014), pp. 210–221.

[132] Armin Wehrfritz, Ossi Kaario, et al. "Large Eddy Simulation of n-dodecane spray flames using Flamelet Generated Manifolds". In: *Combustion and Flame* 167 (2016), pp. 113–131.

[133] L Pickett and G Bruneaux. "Engine combustion network. Combustion Research Facility, Sandia National Laboratories, Livermore, CA". In: *See http://www. sandia. gov/ECN* (2018).

[134] Akira Yoshizawa and Kiyosi Horiuti. "A Statistically-Derived Subgrid-Scale Kinetic Energy Model for the Large-Eddy Simulation of Turbulent Flows". In: *Journal of the Physical Society of Japan* 54.8 (1985), pp. 2834–2839.

[135] S. Menon, P.-K. Yeung, et al. "Effect of subgrid models on the computed interscale energy transfer in isotropic turbulence". In: *Computers & Fluids* 25.2 (1996), pp. 165–180.

[136] Charles D. Pierce and Parviz Moin. "A dynamic model for subgrid-scale variance and dissipation rate of a conserved scalar". In: *Physics of Fluids* 10.12 (1998), pp. 3041–3044.

[137] C Bekdemir. "Tabulated chemical kinetics for efficient and detailed simulations of diesel engine combustion". PhD thesis. 2012.

[138] S Ayyapureddi. "Advances in the application of flamelet generated manifold for diesel engine combustion modeling". PhD thesis. Eindhoven University of Technology, 2014.

[139] Zhaoyu Luo, Sibendu Som, et al. "Development and validation of an n-dodecane skeletal mechanism for00a0spray combustion applications". In: *Combustion Theory and Modelling* 18.2 (2014), pp. 187–203.

[140] Charles K. Westbrook, William J. Pitz, et al. "A comprehensive detailed chemical kinetic reaction mechanism for combustion of n-alkane hydrocarbons from n-octane to n-hexadecane". In: *Combustion and Flame* 156.1 (2009), pp. 181–199.

[141] CMT-Motores Térmicos. "Engine combustion network, Rate of injection". In: *See https://www.cmt.upv.es/ECN03.aspx#* (2018).

[142] Dennis L. Siebers. "Scaling Liquid-Phase Fuel Penetration in Diesel Sprays Based on Mixing-Limited Vaporization". In: *SAE Technical Paper 1999-01-0528*. SAE International, Mar. 1999.

[143] R. Payri, F.J. Salvador, et al. “A new methodology for correcting the signal cumulative phenomenon on injection rate measurements”. In: *Experimental Techniques* 32.1 (), pp. 46–49.

[144] Lyle M. Pickett, Julien Manin, et al. “Transient Rate of Injection Effects on Spray Development”. In: *11th International Conference on Engines Vehicles*. SAE International 2013-24-0001, 2013.

[145] Q Xue, W Som, et al. “A Study of Grid Resolution and SGS Models for LES Under Non-Reacting Spray Conditions”. In: *25th Annual Conference on Liquid Atomization and Spray Systems, Pittsburgh, PA*. 2013.

[146] Stephen B Pope. “Ten questions concerning the large-eddy simulation of turbulent flows”. In: *New Journal of Physics* 6.1 (2004), p. 35.

[147] C J Rutland. “Large-eddy simulations for internal combustion engines – a review”. In: *International Journal of Engine Research* 12.5 (2011), pp. 421–451.

[148] J. Tillou, J.-B. Michel, et al. “Assessing LES models based on tabulated chemistry for the simulation of Diesel spray combustion”. In: *Combustion and Flame* 161.2 (2014), pp. 525–540.

[149] Michele Battistoni, Qingluan Xue, et al. “Large-Eddy Simulation (LES) of spray transients: start and end of injection phenomena”. In: *Oil & Gas Science and Technology* 71.1 (2016), p. 4.

[150] PK Senecal, E Pomraning, et al. “Large Eddy simulation of vaporizing sprays considering multi-injection averaging and grid-convergent mesh resolution”. In: *Journal of Engineering for Gas Turbines and Power* 136.11 (2014), p. 111504.

[151] Yuanjiang Pei, Sibendu Som, et al. “Large eddy simulation of a reacting spray flame with multiple realizations under compression ignition engine conditions”. In: *Combustion and Flame* 162.12 (2015), pp. 4442–4455.

[152] Muhsin M. Ameen, Yuanjiang Pei, et al. “Computing Statistical Averages from Large Eddy Simulation of Spray Flames”. In: *SAE 2016 World Congress and Exhibition*. SAE International 2016-01-0585, 2016.

[153] Daniele Farrace, Ronny Panier, et al. “Analysis of Averaging Methods for Large Eddy Simulations of Diesel Sprays”. In: *SAE International Journal of Fuels and Lubricants 2015-24-2464* 8.3 (2015), pp. 568–580.

[154] Marco Davidovic, Tobias Falkenstein, et al. “LES of n-Dodecane Spray Combustion Using a Multiple Representative Interactive Flamelets Model”. In: *Oil & Gas Science and Technology–Revue d’IFP Energies nouvelles* 72.5 (2017), p. 29.

[155] Heikki Kahila, Armin Wehrfritz, et al. “Large-eddy simulation on the influence of injection pressure in reacting Spray A”. In: *Combustion and Flame* 191 (2018), pp. 142–159.

[156] Lyle M. Pickett, Julien Manin, et al. “Relationship Between Diesel Fuel Spray Vapor Penetration/Dispersion and Local Fuel Mixture Fraction”. In: *SAE Int. J. Engines* 4 (Apr. 2011), pp. 764–799.

[157] M Meijer and LMT Somers. “Engine Combustion Network:” Spray A” basic measurements and advanced diagnostics”. In: *Proceedings of the 12th International Conference on Liquid Atomization and Spray Systems, ICLASS 2012, 2-6 September 2012, Heidelberg, Germany.* 2012.

[158] P. K. Senecal, E. Pomraning, et al. “An Investigation of Grid Convergence for Spray Simulations using an LES Turbulence Model”. In: *SAE Technical Paper 2013-01-1083.* SAE International, Apr. 2013.

[159] Armin Wehrfritz, Ville Vuorinen, et al. “Large eddy simulation of high-velocity fuel sprays: studying mesh resolution and breakup model effects for spray a”. In: *Atomization and Sprays* 23.5 (2013), pp. 419–442.

[160] *Engine Combustion Network: ECN5 Proceedings, Topic 4 Chemistry.* Tech. rep. Sandia National Laboratories, 2016.

[161] Muhsin M. Ameen, Prithwish Kundu, et al. “Novel Tabulated Combustion Model Approach for Lifted Spray Flames with Large Eddy Simulations”. In: *SAE Int. J. Engines* 9 (Oct. 2016), pp. 2056–2065.

[162] Scott A. Skeen, Julien Manin, et al. “Simultaneous formaldehyde PLIF and high-speed schlieren imaging for ignition visualization in high-pressure spray flames”. In: *Proceedings of the Combustion Institute* 35.3 (2015), pp. 3167–3174.

[163] Scott Skeen, Julien Manin, et al. “Visualization of Ignition Processes in High-Pressure Sprays with Multiple Injections of n-Dodecane”. In: *SAE Int. J. Engines* (2015).

[164] Peter M. Lillo, Lyle M. Pickett, et al. *Diesel Spray Ignition Detection and Spatial/Temporal Correction.* 2012.

[165] Rainer N. Dahms, Günter A. Paczko, et al. “Understanding the ignition mechanism of high-pressure spray flames”. In: *Proceedings of the Combustion Institute* 36.2 (2017), pp. 2615–2623.

[166] Cheng Gong, Mehdi Jangi, et al. “Large eddy simulation of n-Dodecane spray combustion in a high pressure combustion vessel”. In: *Applied Energy* 136 (2014), pp. 373–381.

[167] Prithwish Kundu, Muhsin M Ameen, et al. “Importance of turbulence-chemistry interactions at low temperature engine conditions”. In: *Combustion and Flame* 183 (2017), pp. 283–298.

[168] Muhsin M. Ameen and John Abraham. “RANS and LES Study of Lift-Off Physics in Reacting Diesel Jets”. In: *SAE 2014 World Congress & Exhibition.* SAE International 2014-01-1118, 2014.

[169] JM Desantes, JM García-Oliver, et al. “Application of a flamelet-based CFD combustion model to the LES simulation of a diesel-like reacting spray”. In: *Tenth International Conference on CFD, ICCFD 2018, 9-13 July 2018, Barcelona, Spain.* 2018.

[170] Noud Maes, Maarten Meijer, et al. “Characterization of Spray A flame structure for parametric variations in ECN constant-volume vessels using

chemiluminescence and laser-induced fluorescence". In: *Combustion and Flame* 174 (2016), pp. 138–151.

[171] G Bruneaux. "Combustion structure of free and wall-impinging diesel jets by simultaneous laser-induced fluorescence of formaldehyde, poly-aromatic hydrocarbons, and hydroxides". In: *International Journal of Engine Research* 9.3 (2008), pp. 249–265.

[172] C.A.J. Leermakers and M.P.B. Musculus. "In-cylinder soot precursor growth in a low-temperature combustion diesel engine: Laser-induced fluorescence of polycyclic aromatic hydrocarbons". In: *Proceedings of the Combustion Institute* 35.3 (2015), pp. 3079–3086.

[173] Yuanjiang Pei, Evatt R. Hawkes, et al. "Modelling n-dodecane spray and combustion with the transported probability density function method". In: *Combustion and Flame* 162.5 (2015), pp. 2006–2019.

[174] Maarten Meijer, Bart Somers, et al. "Engine Combustion Network (ECN): characterization and comparison of boundary conditions for different combustion vessels". In: *Atomization and Sprays* 22.9 (2012), pp. 777–806.

[175] Prithwish Kundu, Tarek Echekki, et al. "An equivalent dissipation rate model for capturing history effects in non-premixed flames". In: *Combustion and Flame* 176 (2017), pp. 202–212.

[176] Prithwish Kundu, Muhsin Ameen, et al. "Implementation of a Tabulated Flamelet Model for Compression Ignition Engine Applications". In: *WCX2122 17: SAE World Congress Experience*. SAE International 2017-01-0564, 2017.

[177] Muhammad A. Chishty, Michele Bolla, et al. "Soot formation modelling for n-dodecane sprays using the transported PDF model". In: *Combustion and Flame* 192 (2018), pp. 101–119.

[178] *Engine Combustion Network: ECN4 Proceedings, Ignition*. Tech. rep. Sandia National Laboratories, 2015.

[179] Tong Yao, Yuanjiang Pei, et al. "A compact skeletal mechanism for n-dodecane with optimized semi-global low-temperature chemistry for diesel engine simulations". In: *Fuel* 191 (2017), pp. 339–349.

[180] Xiaoqing You, Fokion N. Egolfopoulos, et al. "Detailed and simplified kinetic models of n-dodecane oxidation: The role of fuel cracking in aliphatic hydrocarbon combustion". In: *Proceedings of the Combustion Institute* 32.1 (2009), pp. 403–410.

[181] S.M. Sarathy, C.K. Westbrook, et al. "Comprehensive chemical kinetic modeling of the oxidation of 2-methylalkanes from C7 to C20". In: *Combustion and Flame* 158.12 (2011), pp. 2338–2357.

[182] José M. Desantes, Vicente Bermúdez, et al. "A new method to predict high and low-temperature ignition delays under transient thermodynamic conditions and its experimental validation using a Rapid Compression-Expansion Machine". In: *Energy Conversion and Management* 123 (2016), pp. 512–522.

[183] José M. Desantes, J. Javier López, et al. “Experimental validation and analysis of seven different chemical kinetic mechanisms for n-dodecane using a Rapid Compression-Expansion Machine”. In: *Combustion and Flame* 182 (2017), pp. 76–89.

[184] Christopher Kim Blomberg, Lucas Zeugin, et al. *Modeling Split Injections of ECN “Spray A” Using a Conditional Moment Closure Combustion Model with RANS and LES.* 2016.